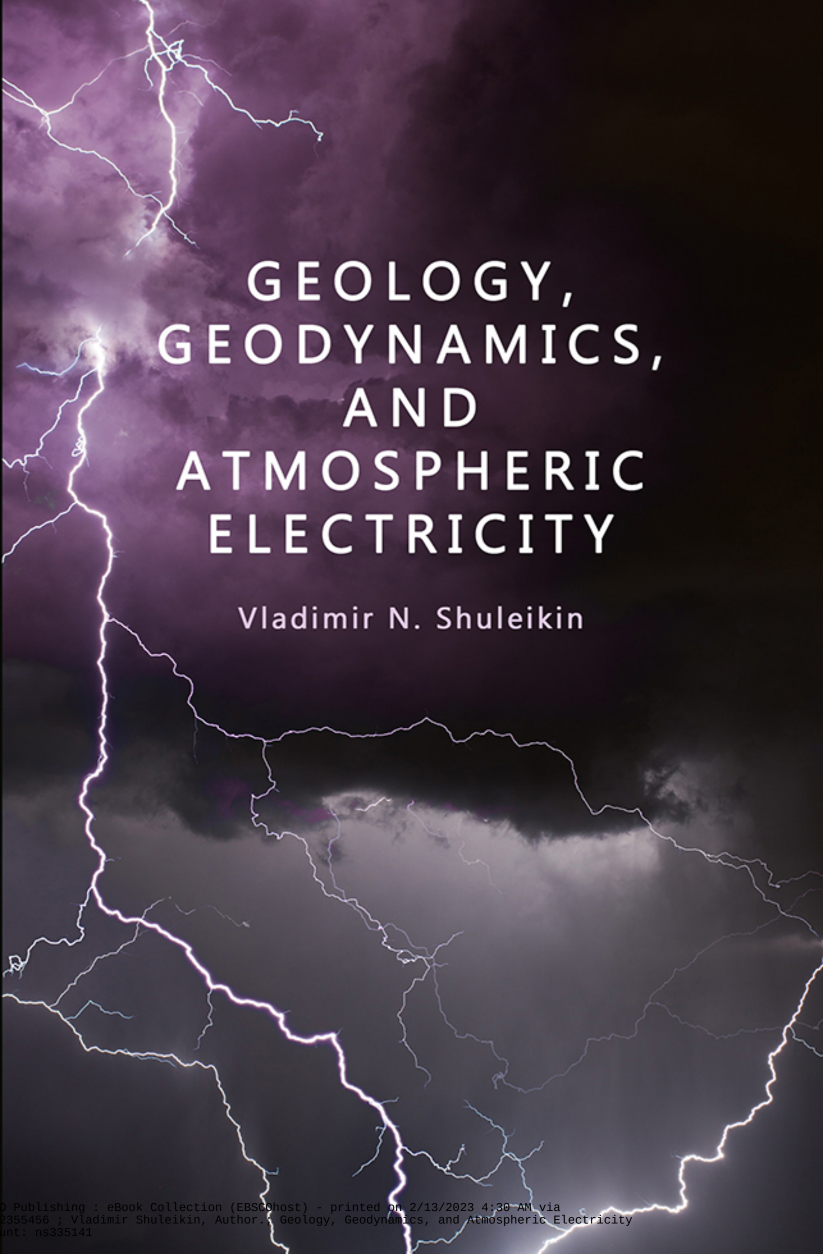

GEOLOGY, GEODYNAMICS, AND ATMOSPHERIC ELECTRICITY

Vladimir N. Shuleikin

Geology, Geodynamics, and Atmospheric Electricity

Geology, Geodynamics, and Atmospheric Electricity

By

Vladimir N. Shuleikin

Cambridge
Scholars
Publishing

Geology, Geodynamics, and Atmospheric Electricity

By Vladimir N. Shuleikin

Reviewers:
Dmitrievsky A. N., Academician of the Russian Academy of Sciences;
Nikolaev A. V., Full Member of the Russian Academy of Sciences

This book first published 2020

Cambridge Scholars Publishing

Lady Stephenson Library, Newcastle upon Tyne, NE6 2PA, UK

British Library Cataloguing in Publication Data
A catalogue record for this book is available from the British Library

ISBN (10): 1-5275-4442-7
ISBN (13): 978-1-5275-4442-0

This research was performed under the auspices of the Oil and Gas Research Institute, Russian Academy of Sciences (3 Gubkina Street, 119333, Moscow, Russia) and was approved for publication by the Academic Council of the Institute.

In memory of my first teachers:
My grandfather, Alexander Kondratievich Kondratiev,
and my father, Nikolai Mikhailovich Shuleikin

TABLE OF CONTENTS

PREFACE

Atmospheric electricity is a research problem in geophysics that consistently attracts the attention of researchers to a variety of phenomena and processes. These involve, directly or indirectly, natural and man-made sources and complex systems taking place in the various shells of the Earth: the lithosphere, the hydrosphere, and the atmosphere. With high energy saturation (from thunderstorm activity) and the complexity of the distribution of electrical, magnetic, and mechanical properties, the Earth's crust, the surface layer of the troposphere adjoining it, the stratosphere, and the ionosphere constantly exhibit unpredictable behavior that has not yet been explained by modern science. On the one hand, the role of electrical phenomena in lithospheric processes associated with the generation of earthquake foci and seismicity is not entirely clear. On the other hand, there is no absolutely clear explanation as to the influence of earthquake generation processes in the formation of anomalous electrical phenomena in the atmosphere. The same can be said about other catastrophic phenomena, such as typhoons, tornadoes, and linear cloud formations over fault zones, which are especially noticeable shortly before seismic events. Similar anomalous phenomena accompanying robust man-made processes include underground nuclear explosions, to which lightning discharges in the atmosphere at the surface level should be added.

At first sight, it is logical to consider the electrical phenomena observed in the atmosphere to be a continuation of telluric processes that take irregular forms and expand their role in the surface atmosphere during the period preceding cataclysmic Earth events. However, this approach cannot be explained from the position of physics. It cannot be assumed that, even in the case of small-focus earthquakes, electric fields generated in the Earth will be discharged through the atmosphere. Even assuming the formation of local anomalous charges, with a linear or circular current source in the area of the hypocenter, their electric fields will be shielded by kilometer-thick layers of sedimentary rock cover, the conductivity of which is many orders of magnitude higher than that of atmospheric air.

For more than 35 years, the author of this monograph has been engaged in experimental study into the connections between geological heterogeneities and processes in the Earth's crust and the elements of surface atmospheric electricity. This work, as well as the work of most geophysicists-researchers in the field of atmospheric electricity, are associated with the forecasting of earthquakes. Preliminary surveys were undertaken on a vibrational testing ground to identify the interrelations of elements of surface atmospheric electricity, which have a powerful effect on the geological environment, and changes in hydrogeological and geochemical fields in the zone of artificial microvibrations.

The classical theory of atmospheric electricity and the radon mechanism for generating the space charge of the surface layer of air was taken as the theoretical grounds of the interactions being studied. Based on numerous field observations, a representational model of the relationships between hydrogen, methane, radon, and surface atmospheric electricity elements was developed. Bubbles of two volatile gases carry radon into the surface atmosphere where, as a result of ionization, light ions are formed that provide polar conductivity in the air. The combination of light ions with neutral condensation nuclei creates heavy ions, which are primarily responsible for the atmospheric electric field. To put it differently, the local space charge of the surface atmosphere is determined by content of the parent substance—radium—at depths of the first few meters below the Earth's surface and sub-vertical volatile gas flux density. This means that any geological anomalies and geodynamic processes that can change hydrogen and methane flux density will inevitably cause changes in the elements relevant to surface atmospheric electricity.

In 1988, the Interdepartmental Geophysical Committee of the Presidium of the Russian Academy of Sciences established a commission—the Global Electrical Circuit Project—for the purpose of developing and adapting research into interactions in the complex lithosphere-atmosphere-ionosphere system. The field observation materials provided in this monograph, and their interpretation, will be of interest in understanding the first stage of these interactions and the relationships between geology, geodynamics, and surface atmospheric electricity.

This book is unconventional in its content and methodological approaches to the study of electrical processes in identifying their relationships with the processes of different physical origins. The results of the complex atmospheric-electrical, seismic, hydrogeological, and geochemical observations presented in this monograph unequivocally indicate the interrelations of the above-listed fields. Groundwater-level dynamics regulate ionizer injection into the atmosphere, while seismic effects aggravate this regulation. Any municipal water intake can increase the atmospheric electric field by an order of magnitude in the depression funnel zone. The efficiency of seismic acceleration in the process increases with a period of microvibrations.

The results of atmospheric-electrical and hydrogen-radon monitoring are all of applied interest in research into: fault zones; ore bodies; basement rock areas; oil fields and the dynamics of their development; the process of combustible gas dispersion in an underground gas storage reservoir bed; and the stress-state of a landslide, the movement of which can be provoked by the laying of a pipeline.

In academic courses on atmospheric electricity, changes in the electrical characteristics of the surface air layer are associated exclusively with the dynamics of the meteorological situation. The data in this book enhances our understanding of the physical origin of this phenomenon. In stable meteorological conditions, changes in the electrical characteristics of the surface air layer are determined exclusively by the geological and geodynamic features of the environment.

The author of this monograph solves here a number of unconventional problems and, at the same time, discovers new effects and antimonies, the explanation of which will be marked by advances in geophysical science in years to come.

Academician A. N. Dmitrievsky

INTRODUCTION

In the mid-eighteenth century, Benjamin Franklin suggested an experiment using a kite flown into a thunderstorm cloud. The investigation was conducted independently by T. Delibard and B. Franklin and completed with the creation of the lightning conductor. At the same time, after experiments on a “thunder machine,” Mikhail Lomonosov formulated the first hypothesis on the charging of thunderstorm clouds. Today’s research suggests the existence of a multistage global electrical circuit connecting the Earth’s shells and the atmosphere in an integrated system. The establishment of relationships between parallel processes in different Earth shells highlights the problem of the global electrical chain. The phenomena of interest in studying the global electrical chain are at the planetary-spatial scale and require the use of rockets, ionospheric balloons, and aircraft; and the taking of measurements in space, at ground level, and in the lithosphere.

In 1890, the primary experimental results on disturbances of the electric potential in the atmosphere—the atmospheric electric field—before, during, and after seismic events were obtained at the Imperial Meteorological Observatory in Tokyo. Perturbations of the field recorded with clear weather conditions before the 1926 earthquake in Kyrgyzstan were named the “Electric Storm.” In the mid-twentieth century, extensive field material on abnormal variations of the atmospheric electric field before seismic events was obtained at the Gharm Forecasting Test Site of the Institute of Earth Physics, RAS. Up to the present day, in the scientific literature, one can find only a few works that describe such field anomalies during drastic changes in the seismic mode. As per accepted classification, these perturbations relate to short-term precursors, are bipolar, and are several times larger in magnitude than the general background signal level. Their development can take from tens of minutes to hours before an earthquake.

P. Tverskoi and J. Chalmers, the founders of the surface atmospheric electricity theory, have pointed to radon as the origin of the surface charge of atmospheric surface air. The ionization process forms a pair of light ions that determine the polar conductivities of the air. The combination of light ions with neutral condensation nuclei creates heavy ions, which are primarily responsible for the formation of the atmospheric electric field.

The negative charge of the Earth and the presence of positive and negative ions in the surface atmosphere inevitably led researchers to discover the electrode effect. At first, the problem was addressed by approximating the presence of light ions in air at the Earth's surface. Such estimates did not correspond to the actual atmospheric situation, where heavy ion density is almost an order of magnitude higher than light ion density. However, this does not contradict the physics of the atmospheric situation, which sees the presence of positive and negative ions of comparable concentrations in surface air.

In studying the relationship of the atmospheric electric field to altitude, it was immediately possible to distinguish two cases: the classical electrode effect and the reverse electrode effect. In the first case, with a low ionization rate—a low concentration of emitted soil radon—the electrical field smoothly decreases with the height of the relatively negatively charged electrode and reaches a background level determined solely by the space charge. At a high ionization rate—a high radon concentration—a negative space charge layer forms above the ground; after a particular height the field then decreases below the background level, the yield of which follows a curve that describes the measurements of field values if they were to be plotted on a graph.

The calculation of the classical and reverse electrode effects led to an understanding of the bipolar nature of changes in the atmospheric electric field before earthquakes. If the measurements were carried out in the compression zone where ionizer emission was minimized, the measuring device recorded abnormally high fields. In the extension zone, the release of soil radon into the atmosphere reached its maximum. Here, at the Earth's surface, a thick layer of negative space charge was formed and measurements of the atmospheric electric field showed the formation of abnormally low negative fields.

The mechanism of soil radon transport into the near-surface atmosphere remained an open question. The high molecular weight of the ionizer, Rn^{222}, precluded the possibility of its isolated sub-vertical migration. For a long time, we believed that bubbles of all the volatile gases in soil air acted as ionizer carriers, bringing radon to the surface. However, radon detection at altitudes of several kilometers during the taking of measurements from an aircraft has suggested a limited density of the carrier gases. Radon efflux to altitudes of several kilometer could only be performed by gases whose density is less than the density of atmospheric air. These gases potentially also include four ingredients of soil air: hydrogen, helium, methane, and water vapor. Helium, like radon, belongs to the category of inert gases and the capture of one inert gas by a bubble of another inert gas is impossible. The evaporation process takes place in a thin surface layer of the ground, where the radon soil concentration is almost equal to its atmospheric level. Even if water vapor participated in radon transport, the contribution of the ionizer transported by water vapor to the total radon content in the atmosphere would be minimal. Additional experimentation has confirmed this conclusion.

Following this logic, one can state that the soil-to-atmosphere air exchange determines the space charge dynamics of the surface air at the point of observation. The half-life of radon is 3.8 days, which suggests that the emanated gas must enter the atmosphere from shallow depths. This is because as over a period of three half-lives, its concentration decreases by almost an order of magnitude. All this means that the emitted soil radon is only a mediator, which opens up the possibility of tracking the density of sub-vertical hydrogen and methane fluxes through measuring local values of polar conductivities and the atmospheric electric field.

In fracture zones, intensification of the soil-to-atmosphere air exchange is observed. Excessive methane concentrations are present in oil field plumes and electrochemical processes in the caps of ore bodies increase the hydrogen concentration in soil air.

Recording of the abnormal electrical characteristics of surface air before seismic events is somewhat random, as the researcher must be in the right place at the right time. Measurements of the atmospheric electric field and polar air conductivities above geological anomalies and in geodynamic process zones can be performed in a targeted manner. The results of these studies and their analysis form the basis of this monograph.

The author considers it a pleasant duty to express his deep gratitude to Alexei Vsevolodovich Nikolaev, the Corresponding Member of the Russian Academy of Sciences, whose support allowed me to carry out research in Belarus and Central Asia and the Academician, Anatoly Nikolayevich Dmitrievsky, who is the moderator of research into hydrocarbon accumulations. I also wish to thank my colleagues and friends: Reznichenko Alexander

Pavlovich, Barabanov Vyacheslav Leonidovich, and Gufeld Iosif Lippovich for their help in carrying out fieldwork; Professor Georgy Georgievich Shchukin, the co-author of many of my articles. I make a deep bow to: Ilya Moiseevich Imyanitov, Dr. Sci. in Physics and Mathematics; Yakov Mikhailovich Schwartz, Ph.D. in Physics and Mathematics; Georgy Ivanovich Voitov, Dr. Sci. in Geology and Mineralogy; Professor Dmitry Nikolayevich Chetaev; Alexey Mikhailovich Polykarpov, Ph.D. in Physics and Mathematics who has passed on and whose help in performing tests and fieldwork and interpreting the results has been invaluable.

CHAPTER 1

ATMOSPHERIC ELECTRICITY AND THE PHYSICS OF THE EARTH

In the mid-eighteenth century, the practical study of lightning electricity started in both Russia and the USA almost simultaneously. In 1745, Mikhail Lomonosov and Georg Richmann designed the first electrical-type instrument—the 'electric indicator.' This electric indicator differed from the famous electroscope in its use of a wooden quadrant with a scale, which allowed the quantitative assessment of the deflection of a linen thread from the vertical plane. This innovation allowed the measurement of a "higher or lower electricity level."

A wire connected the electric indicator to a metal rod on the laboratory roof. The "thunder machine" showed that electricity existed in the atmosphere, even in fair weather.

In 1750, B. Franklin suggested an experiment that used a kite flown into a thunderstorm cloud. On May 10, 1752, the French physicist Thomas-François Dalibard carried out the same investigation. The work by Benjamin Franklin logically resulted in the design of a lightning conductor. According to B. Franklin, the lightning conductor "...either prevents lightning discharge from a cloud or, already at the discharge, deflects the lightning to the ground without any detrimental effect to a building...." In 1760, B. Franklin installed the first lightning conductor on the house of the tradesman Benjamin West in Philadelphia.

Since the early nineteenth century, the interest of researchers in studying thunderstorm electricity has subsided a bit and the focus has been on the study of "fair weather" electricity. At the end of the 1800s, Japanese researchers showed the presence of abnormal changes in the potential of the atmosphere before, during, and after earthquakes. Up to the present day, one can find several (20–30) publications on changes in the atmospheric electric field before seismic events in the scientific literature.

The discovery of the radon mechanism of surface space charge generation provided the foundation for the modelling of the relationships between gas and electric fields in the ground and the atmosphere. Bubbles of hydrogen and methane transport soil radon to the surface atmosphere where, in the ionization cycle, light ions form. These are responsible for the polar conductivity of the air. The aggregation of light ions with neutral condensation nuclei causes the formation of heavy ions, which are primarily responsible for the atmospheric electric field (AEF).

1.1. The History of Observation and Equipment

Published results of instrumental observations indicating the appearance of unusual perturbations of the atmospheric electric field (AEF) before an earthquake are very few. In the late nineteenth century, the Imperial Meteorological Observatory in Tokyo implemented annual monitoring of the atmospheric potential. Nine times out of ten, strong earthquakes with foci as far as 100 km from Tokyo were seen to induce anomalous perturbations in the field [1].

Before an earthquake of magnitude M = 4.5 occurred on August 1, 1924, in Kyrgyzstan, disturbances of the AEF of a very complex shape were recorded at a distance of about 150 km from the epicenter in clear weather:

- 5 hours before the seismic event, a decrease in the signal level began;
- 4 hours before, intense discharges and charges of the electrometer at a frequency of 1.0–1.5 Hz began;
- at the same time, the maximum field values reached 1,000 V/m [2].

In 1946, before the Chatkal Earthquake, and in 1949, before earthquakes in Dushanbe and Obi-Gharm, similar effects were observed [3]. In the cases considered, the sign of the recorded parameter also changed.

Five hours before the Tashkent Earthquake, with a magnitude M = 5.3, took place on April 26, 1960, a change in the vector of the atmospheric electric field was recorded in the epicentral zone [4]. The meteorological situation in the observation area on the eve of the earthquake was turbulent; it stabilized only a few hours before the seismic event. Anomalous AEF perturbations were also recorded before several of the most powerful aftershocks. However, in most cases, no noticeable changes in the field before most of the aftershocks were observed.

Immediately after the catastrophic Khait Earthquake occurred on June 10, 1949, monitoring and AEF measurements 50 km from the epicenter were initiated by the Gharm Expedition of the Schmidt Institute of Earth Physics. In 22 out of 23 cases, 1.5–2.0 hours before the strongest aftershocks, with M = 5–6 at the observation point, an increase in the signal of ~100 V/m was observed. Over the summer season of 1950–51, in the same area, the atmospheric electric field was continuously recorded at five points. Perturbations of the AEF, similar in form to those before local seismic events of M = 5–6 were successfully recorded [5].

Up to today, the field observations obtained at the Gharm Test Range of the Schmidt Institute of Earth Physics represent the most significant source of information on abnormal AEF precursors before seismic events [6]. Modern retrograde analysis of the results has allowed the rejection of some of the recorded anomalous field changes, as they were associated exclusively with current changes in the meteorological situation [7]. However, even taking into account the current level of scientific knowledge and instrument capability, it is necessary to pay tribute to the high professionalism of those experts who developed unique experimental material in the middle of the past century.

In 1977, AEF disturbances were recorded at the Gharm Test Range at three observation points 1 to 2.5 days before a K = 13 earthquake and at epicentral distances of 20–35 km. The perturbations took the form of distinct oscillations with a period of 6–10 minutes [8].

At an observation station in China [9], before earthquakes of M = 4.6–6.1, anomalous decays of AEF were observed at epicentral distances of 100–250 km. Perturbations occurred at time intervals ranging from several days to one month before a seismic event and reached 500–950 V/m. During periods of seismic calm, such disturbances were not observed.

Further observations over the past 12 years have confirmed the reliability and stability of such manifestations of AEF anomalies [10, 11]. Following analysis of the results of observation, certain regularities of earthquake precursors were established based on AEF monitoring data. Their geographical features were highlighted and theoretical ideas were developed that satisfactorily explained the nature of the anomalies observed [12, 13]. Similar decreases in AEF before an earthquake are discussed in [14].

The field changed its sign at an epicentral distance of 18 km, six hours before an earthquake of magnitude M = 3.5 in California. About a day before another seismic event of the same energy, with calm weather conditions, oscillations with a total duration of about four hours were recorded at two points with epicentral distances of 8 km and 20 km. At a position 50 km from the epicenter, no anomalous perturbations of the AEF were detected [15]. Fluctuations in AEF intensity before an earthquake, class $K = 11$, are described in [16].

Convincing results on variation in AEF before earthquakes are presented in [17, 18]. Unfortunately, these studies only provide a concise (less than a day) series of observations, which do not allow us to assess the origin of background field variations before and after seismic events. Description of the meteorological situation is limited to mentioning the calmness of the weather at the observation point and we cannot speak confidently about the tectonic origin of the recorded anomalies.

The space charge of air at the Earth's surface owes its origin to ionization from emitted soil radon [19–22]. In the summer of 1914, this effect was used when prospecting for radioactive ores by the Moscow Radium Expedition in Fergana, Uzbekistan [23]. In 1919, S. Kurbatov performed laboratory studies on the ionizing radiation of rocks sampled from the Yulin Mine near Minusinsk, Krasnoyarsk Krai, Russia. In 1920, using these lab results, he succeeded in detecting a deposit of radioactive ores located 12–13 km southeast of the Yulin Mine.

In performing field observations, classical measuring devices are used to record polar conductivities (PCs) and AEF—an aspiration capacitor unit combined with a field mill have been used around the world to take atmospheric-electrical measurements for decades. Let us turn to the refinement of the technique of using these devices in the field.

To reduce the sensitivity of the PC sensor to an external wind load, in some cases, a block of aspiration condensers was mounted vertically above a ~20-liter pit and the "soil air" was purged directly through the condensers [24]. When specialized observations are performed from a vehicle, a set of aspiration condensers is placed on the back seat; the air is purged through an open window; and the machine is oriented perpendicular to the wind direction.

Until the mid-1990s, the signal was recorded using a two-channel analog data recorder, and later on by a personal computer. In the latter case, in the presence of noticeable variations of signals relative to the average level, the correlation coefficient between them was calculated at once. When the correlation coefficient was below 0.8, the measurement was repeated.

In the initial experiments measuring the AEF profile, the field mill was placed on the ground at each observation picket [25]. Sometimes, towing it on a sled-trailer behind a motor vehicle led to noise contamination of the signal due to the accumulation of dust. The best way to install the measuring device is in the roof hatch of a car. Measurements were always carried out in fair weather conditions [26–28]. Each controlled profile was passed at least twice, Figure 1.1.1.

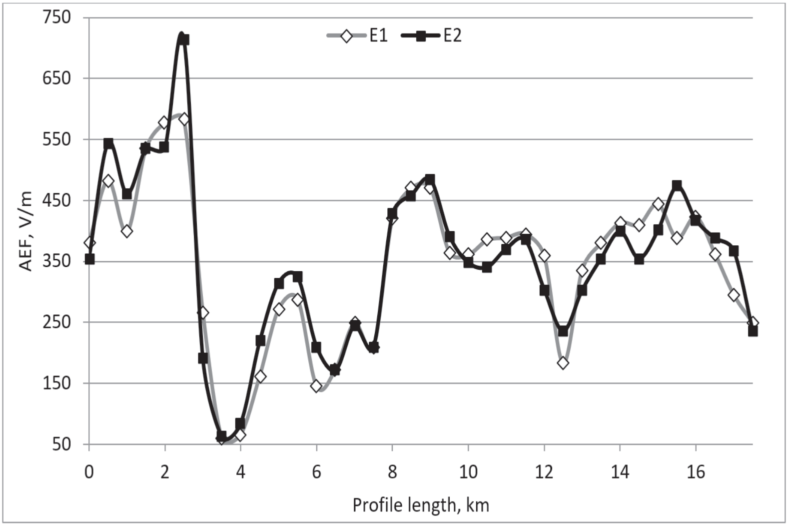

Figure 1.1.1: An example of recording AEF for a double-pass, E1 & E2, profile length of 17.5 km.

Due to the limited demand for AEF sensors, this device has never been serially manufactured. The most extensive series of the Pole-2 device was designed and manufactured at the Experimental and Production Workshops of A. I. Voeykov Main Geophysical Observatory. For many years, AEF sensors have been in operation at the Voeykovo settlement and at several meteorological stations, including: Verkhnee Dubrovo; Dusheti; Irkutsk, Yuzhno-Sakhalinsk; Karadag, Kyiv; Murmansk; and Odesa [29]. For mobile AEF observations, a gradient measuring device from the same manufacturer, designed to be powered by an autonomous 12 V power supply, was used.

Before developing a measuring device for a regime of forecast observations at five pickets at a landfill site in Tajikistan, based on observations in the Tiksi Bay [30], AEF and the air-earth current were studied. The measurements were carried out using a sensor grid [31] at a height of 1 m above the ground on four insulated pillars. A grid of 100 m² area and a cell size of 0.1 m × 0.1 m was installed. Figure 1.1.2 shows the air-earth current variations recorded in fair weather conditions, including still air and zero cloud cover. The AEF was simultaneously recorded.

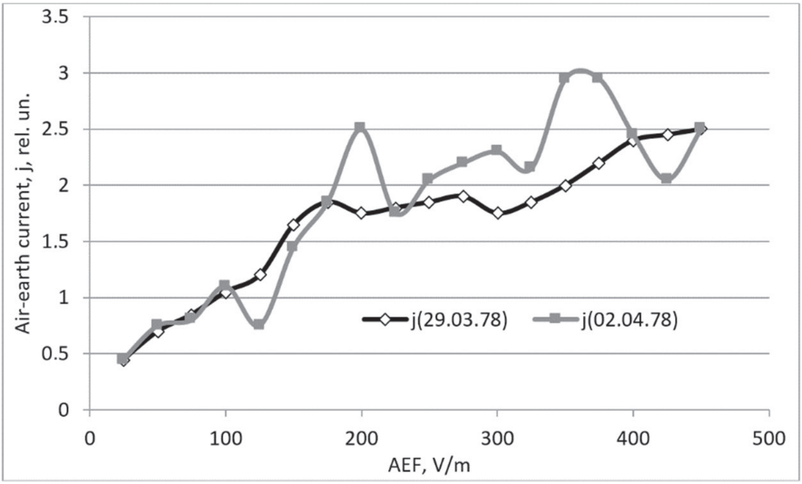

Figure 1.1.2: Non-linear origin of Ohm’s law in the atmosphere with measurements at Tiksi Bay.

Formal mathematical evaluation allows us to say that in fields of up to 100 V/m, the accuracy of the linear field and current approximation is *D* ~0.95–0.98 and the scatter of the reduction coefficient, *k*, is below 2 %; up to 200 V/m—*D* ~ 0.85–0.95, *k* ~(2–9) %; up to 300 V/m—*D* ~0.85, *k* ~(35–66) %; and up to 400 V/m—*D* ~0.85, *k* ~(54–104) %. In fields of over 200 V/m, however, the linearity of Ohm’s law in the atmosphere is violated.

Taking into account the abnormal changes in the AEF recorded before seismic events (see above) and deviations from Ohm's law in fields above 200 V/m, the air-earth current was chosen as a control parameter at observation pickets in Tajikistan. Disadvantages of the grid sensor included: low noise immunity where convection currents were concerned; vortex movements of dust charge formations; low technological capability at the test installation; and long-term operation of the collecting element. Continuous operation of the current sensor in Central Asia required us to solve the problem of ensuring noise immunity of the measuring device to interference from the surface layers of dust that formed up to a thickness of several decimeters.

A single-wire antenna was used as the basis of the measuring device [19, 32, 33]. To minimize near-surface interference, the antenna height was increased to 5–6 m. At the same time, this increase improved the technical capability of the sensor, as it eliminated the possibility of the collecting element being disconnected, for example, by vehicles passing over it. Furthermore, a second, additional collecting element was added to the measuring circuit. This element was located on the same plane as the main element, in parallel with it and the Earth's surface. The main and additional antennas were separated by a distance of an order of magnitude smaller than their installation heights: $\Delta H = H(\mathrm{A1}) - H(\mathrm{A2})$. At the same time, the signal difference at the output of the main and additional antennas minimized common mode interferences from convection currents and near-surface dust formations.

Differential antenna operation was repeatedly verified by comparison with field results and conductivity measurements at the Voeykovo and Borok Observatories [34]. Figure 1.1.3 shows synchronous records of the air-earth current and AEF. The extremely high reliability of the field mill and differential antenna operation is illustrated by a 31-hour recording period that was obtained under extremely unfavorable weather conditions. The collecting elements of the differential antenna of 80 meters in length were installed on nylon extensions and with fluoroplastic insulators between the roof of the laboratory building and the mast, which was installed 100 m away from the building. The height of suspension of the upper collecting element of the passive differential antenna was $H(\mathrm{A1}) = 8$ meters with a spacing of 0.6 m.

The Pole-2 field mill was installed on the roof. For the convenience of data comparison, all the records in Figure 1.1.3 are given in relative units. The AEF sensor was calibrated in absolute units: a 300 V/m field corresponds to 10 rel. units of the scale used.

The correlation coefficients between parameters for 31 hours of continuous observation equal: *k*[AEF; *j*(dif.ant.)] = 0.8; *k*[AEF; *j*(grid)] = 0.6; *k*[*j*(dif.ant.); *j*(grid)] = 0.62. On a purely formal basis, records obtained by a differential passive antenna are closely related to changes in the atmospheric electric field.

The extremely flat pattern of recordings from the "grid" in the period of 5 to 26 hours and the signal minimum at the 27th hour of observation is doubtful. At the AEF and *j*(dif.ant.) channels, this minimum occurred one hour earlier, when snowfall began to decline. The recorded delay can, most likely, be attributed to leaks from the "grid" installation masts. Joint tests of measuring devices have shown that a field mill and a differential antenna comprise the meteorological sensors with the lowest noise.

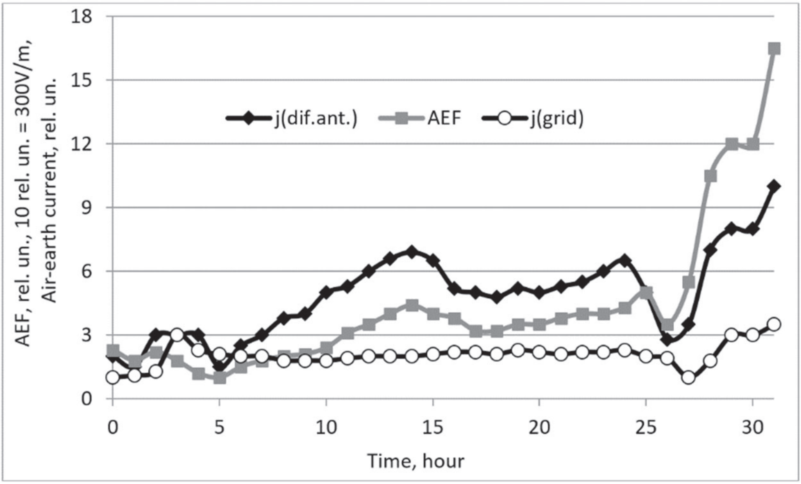

Figure 1.1.3: Synchronous recordings from the differential antenna *j*(dif.ant.), the field mill—AEF, and the gauge of "grid" type *j*(grid), obtained between 08h 00m 02/01/87 and 15h 00m 02/02/87. 31 hours of continuous recording under extremely adverse meteorological conditions: hours 2–4 fog; hours 10–15 strong wind; hour 26 snow showers; hours 29–31 strong wind, clear.

Tests of the differential antenna were carried out at one of the stations of a forecast test range in Tajikistan. Figure 1.1.4 shows nine eight-minute signal recordings using a single-wire and differential antennas with different installation heights and separations. The upper graph presents the optimal variant of installation height and separation of the differential antenna. If consecutive recordings from single-wire antennas—only the upper one H(A1) with the lower one removed or, vice versa, H(A2)—are characterized by a 40–80 % signal scatter, then recordings from the differential antenna (dif.ant.) have a separation of ΔH = 0.57 m, as expected this is much more stable and characterized by scattering with a level of 16 % in total.

The situation is somewhat worse for the case where the suspension height of the additional antenna was reduced to H(A2) = 4.15 m, and the separation was increased to ΔH = 0.82 m. The signal scatter of the single-wire antennas H(A1) and H(A2) increased by 30–77 %. At the same time, the effect of differential reception and signal amplification also deteriorated and the signal scatter during the eight-minute recording increased to 19 %.

The effect on differential reception and amplification of the signal of the drop in elevation can be seen in the lower graph in Figure 1.1.4, where the installation height of the additional antenna was H(A2) = 3.44 m and the separation was ΔH = 1.53 m. The signal scatter from the upper, H(A1), and lower, H(A2), single-wire antennas was 31–86%; while from the differential antenna it was 24 %.

The control measurements performed show that the measuring device developed significantly reduces the noise component of the signal, which is associated with convection currents, dust surface charges, and dust charge transfer. With the help of a differential antenna, several anomalous air-earth current variations were recorded; these are described below.

Since the mid-1990s, atmospheric-electrical measurements have always been performed in conjunction with observations of soil-air hydrogen and radon. In all the complex measurements described below, a radon volumetric activity sensor, RGA-01, was used, which was able to operate in an ambient temperature range of +5 °C to + 50 °C. The relative error of a single count was 30 % when operating in the range of 10^{-2}–10^{3} Bq/l. In the course of observation, each soil air sample from the sampling well at the picket was analyzed four times.

The 15-year experience of operating the measuring device, especially in temperatures of 30 °C or higher, led to the development of an optimal technique for taking four rapid and consecutive radon readings from samples of the soil air and the atmospheric air. A

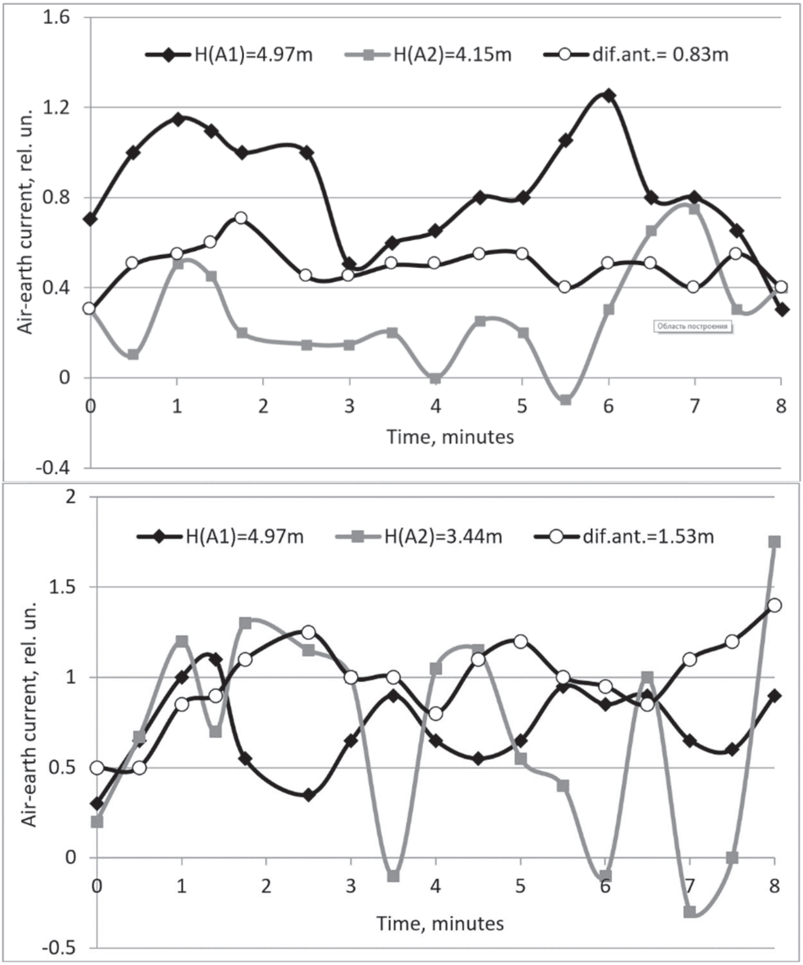

Figure 1.1.4: Examples of 8-minute recordings of the air-earth current signal recorded by single-wire and differential passive antennas with different installation heights.

minimal loss of time and accuracy at the observation picket can be achieved when the first count is read at a 200 s time interval, and the next three counts are read at 20 s intervals. The reason for this is that there is a significant difference in the temperature of the soil air and the atmospheric air, as a result of which the fluorescent coating of the operational chamber is heated during four 200 s intervals of alpha particle count accumulations. As a result, the efficiency of the coating increases, which leads to a noticeable rise in measurement errors. During measurements, the operational chamber of the radon activity sensor was insulated on the outside by polyurethane foam and periodically damped with water and the measuring device was shielded from direct sunlight.

Similarly, samples of atmospheric air were analyzed that partially equalized the measurement errors of radon in the soil and the atmosphere. The volumetric activity of radon in the atmosphere is substantially less than in the soil, usually falling to levels around tenths to units of becquerels per liter.

Taking into account the half-life of thoron, $\tau_{\mathrm{Tn}} = 57$ s, it was assumed that the number of α-decays at the first reading was additive and consisted of the bulk of the α-activity of radon, while the thoron decayed almost completely. For the next three 20 s counts, only the α-decay of radon in the working chamber of the device was discoverable. Such an assumption is fully justified since almost four half-lives of thoron fit the time interval of the first count, that is, the volume concentration of Tn in the working chamber of the measuring device naturally decreased by more than an order of magnitude.

The radon activity in a sample is calculated by averaging 2 to 4 counts. Accordingly, after averaging, the error in determining the volumetric activity of radon at each observational station decreases to about 17 %.

Following analysis of the measurements obtained over many years, one can say that the data sets on the volumetric activity of soil radon and atmospheric radon correlate to one another [35, 36]. There is no correlation of these parameters with the volumetric activity of atmospheric thoron. This is due to the minimal values of the volumetric activity of atmospheric thoron. Over the entire observation period, the volumetric activities of these radiogenic gases were comparable to one another only at a profile passing over a rock crushing zone (Pelagiada Farm, Stavropol Territory) (Figure 1.1.5). According to the drilling data, the surveyed area was located in the rock crushing zone.

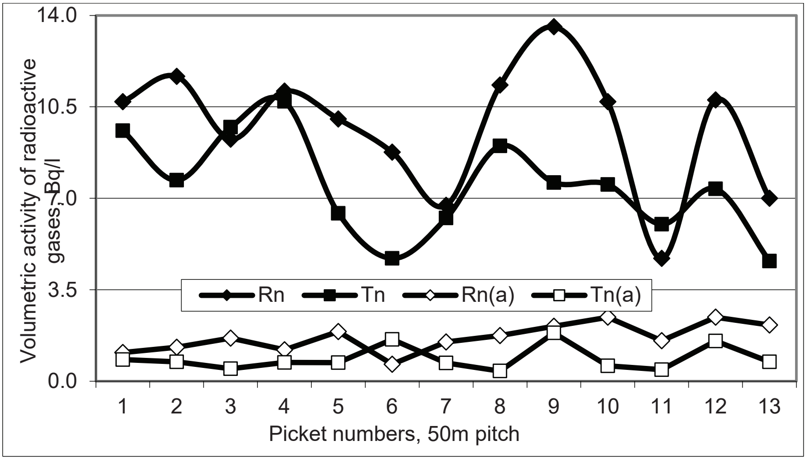

Figure 1.1.5: An example of comparable radon and thoron volumetric activities.

Before 2004, during fieldwork, one or two identical volumetric soil hydrogen concentration sensors, GVK G-01, designed and manufactured by the Moscow Engineering Physical Institute (MEPHI), were used as appropriate [37]. The principle of the sensor was based on variations in condenser capacitance, in which the permittivity of the gasket varied depending on hydrogen concentration in the working chamber of the measuring device.

The next modification of the measuring device, the hydrogen geophysical signaling device VSG-01, was designed for long-term continuous measurements of hydrogen concentrations in soil or atmospheric air [38]. Transfer of the measuring device to online recording caused some changes in the observation technique and the construction of the working chamber. In the original version, the sensor was designed for the natural flow of the soil or atmospheric air. To this end, the remote module with the sensitive element of the sensor was buried in the ground or placed in the investigated volume of the atmosphere. In the online mode, the working chamber of the remote module was sealed from direct air intake. The measurement cycle at the observation picket consisted of a series of procedures. First of all, the working chamber was pumped with atmospheric air, and the readings taken were assumed to be zeroed. Then, a sample of a tabulated volume of soil air—30 ml for the VSG-01 sensor—was introduced into the working chamber. The difference between the signal and the zero samples was assumed to be due to the volumetric hydrogen concentration in the soil.

The measured volumetric hydrogen concentrations were in the range 0.1 to 50.0 ppm, with a relative error of about 10 % of the current background values. The transition to the volumetric concentration of hydrogen in the sample in ppm is implemented according to the calibration graph. In the range of 0.0 V to 1.5 V, the sensor division value (roughly) is 1 ppm—30 mV.

Since 2005, the complex has used next-generation measuring devices: VG-2B #18 & #19 gas detectors [39]. With the same operating parameters, the sensor has a 6–8 ml working chamber, rather than a 30 ml one, consumes less power, and is structurally better suited to field operation.

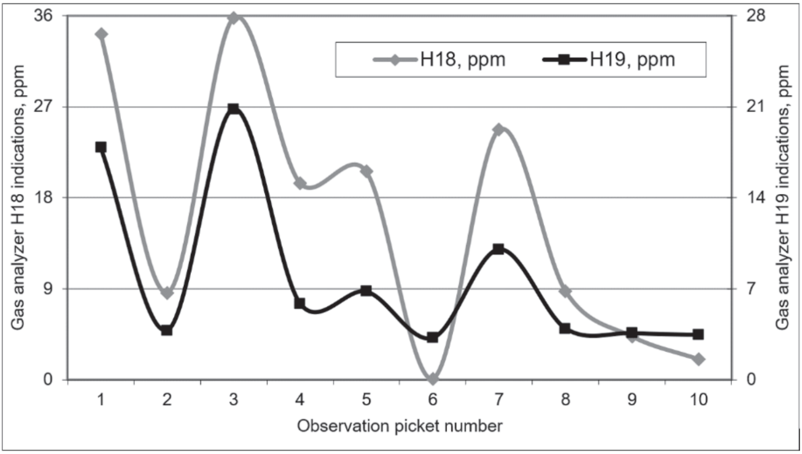

Figure 1.1.6: Verification results for the identity of hydrogen sensors VG-2B #18 & #19 before leaving for fieldwork in 2008.

In autumn 2006, in cooperation with the developer, a simultaneous sampling technique using two VG-2B sensors was improved. Sensitive elements of the instruments were introduced in the same working chamber of about 0.5 l. According to the laboratory calibration, a nonlinear transient function was introduced for each sensor with a confidence value of 0.99, which associates signals in [mV] with [ppm]: $H18_{ppm} = 0.0013(H18_{mV})^{1.589}$; $H19_{ppm} = 3.2178 \times \exp[0.0027(H19_{mV})]$. The results of the joint testing of the measuring devices are shown in Figure 1.1.6. In the latter version of air sampling at the observation picket, only one sampling well was used. The selection was performed sequentially, through a 0.5 l volume of the hydrogen sensors in the working volume of the radon sensor.

The sensors of the atmospheric electric field Pole-2 and gradient allowed for absolute calibration at the installation site. This calibration was carried out daily before and after the start of operation.

A measuring device, RGA-01, for recording the volumetric activity of radon was calibrated at the All-Russian Research Institute of Physical and Technical Measurements and Radio Metering (VNIIFTRI) before and after fieldwork. The scatter of readings fit the error limits of the measuring device. A similar procedure was carried out for the hydrogen sensors at the Moscow Engineering and Physics Institute.

Checking of the operational stability of the aspiration capacitor unit was carried out at the site in the Moscow Region. Before and after the fieldwork and in fair weather conditions, the sensor was checked at eight fixed pickets of similar profile. Over the entire observation period, the correlation coefficient of the profile variations of polar conductivities did not descend below 0.7.

1.2. Model of the Relationships between Hydrogen, Methane, Radon, and Elements of Surface Atmospheric Electricity

The first experimental results illustrating the relationships between methane, hydrogen, radon, and the atmospheric electric field were obtained at the Alexandrovsky Structure of the Gomel Region in Belarus [40, 41]. Elevated concentrations of methane, hydrogen, and radon were recorded above an oil reservoir and the fault structure was, in turn, indicated by a decline in the atmospheric electric field, AEF.

In 1998, the same regularities were observed at the Kaluga Ring Structure [42]. On two profiles intersecting at the center of the structure, with a length of 20 km and 18 km, radon and hydrogen in the soil air and the atmospheric electric field were measured using a unified system of observation pickets (21 pickets and 19 pickets, respectively). At the same time, the soil air was sampled at eight pickets for subsequent quantitative analysis of hydrogen, nitrogen, carbon dioxide, methane, and their homologs in the laboratory.

The Kaluga Ring Structure is located on the north-western plunge of the Voronezh Anteclise, at the junction of four neo-active faults. The observations aimed to study sub-vertical mass transfer in zones of tectonic deconsolidation effects against the background of the relatively weak geodynamic activity of the East European Platform in the region of platform sediment deposition.

The choice of equipment chosen for observation was determined by the hypothesis of causal-correlational relationships between the monitored parameters. For a long time, bubbles of all volatile gases in soil air were believed to be radon carriers to subsurface soil layers and the atmosphere [43]; but the high molecular weight of Rn^{222} eliminates its separate sub-vertical migration to surface layers of the soil and the atmosphere. As water-gas systems rise in the zone of increased rock permeability, volatile gases dissolved in water tend to separate into self-contained phases as separate bubbles. In the course of sub-vertical lifting, pressure in the bubbles drops and the volume—the contact area of the bubbles with the liquid and the rock—increases. Bubbles become natural degasifiers where, along with other gases, soil radon, which is formed in underground water-gas systems during the decay of dissolved radium, also drains. One of the volatile gases, hydrogen, was promptly monitored while setting up the measurements.

According to estimates [44–46], and taking into account the half-life of radon of 3.825 days, radon enters the subsurface soil layers from a depth of ten meters below the Earth's surface. The same bubbles carry hundredths to thousandths parts of an emission gas to the surface atmosphere [47, 48]. Here, according to the provisions of the surface atmospheric electricity theory, emitted radon is the only natural ionizer of atmospheric air. Ionization products—positive and negative light ions—determine the polar conductivities of the air and combine with neutral condensation nuclei to form heavy ions, which are primarily responsible for AEF.

Setting up complex observations of soil air hydrogen and radon to search for relationships between parameters requires the temporal stability of sub-vertical mass transfer. The change in the density of the sub-vertical carrier gas flow—hydrogen in the problem being considered—effects changes in the volumetric activity of radon in the surface layers of the soil. This is why the experiment was conducted at the Kaluga Ring Structure on the East European Platform. Here, on the one hand, the geodynamic situation is fairly stable and, on the other hand, there are zones with tectonic deconsolidation effects. To put it differently, here we can expect the presence of contrasting high-amplitude variations of the parameters we wished to monitor.

Figure 1.2.1 gives histograms of hydrogen concentrations and the distribution of radon volumetric activity at 40 observation pickets.

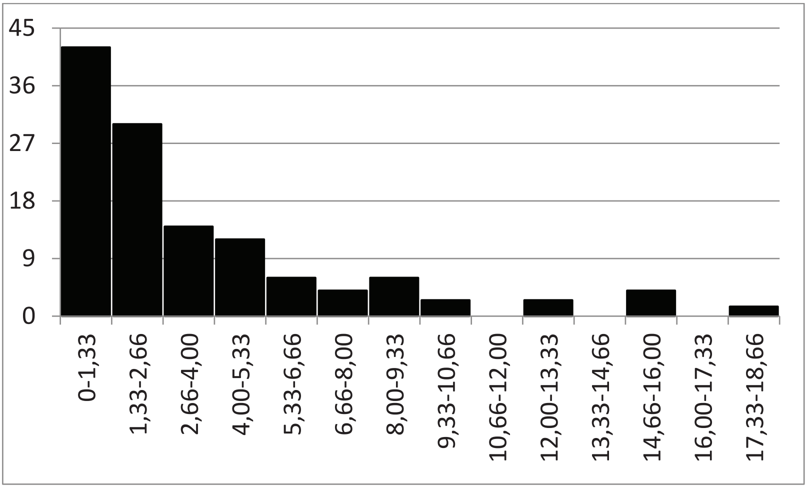

The range of changes in hydrogen concentrations, ppm

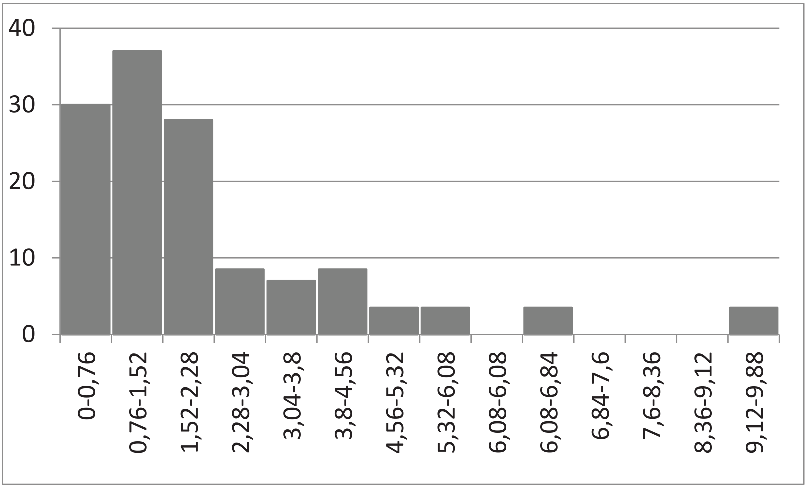

The range of changes in the radon volumetric activity, Bq/l

Figure 1.2.1: Histograms of the series of hydrogen concentration and radon volumetric activity distributions at 40 observation pickets.

Distributions of the volumetric activity of radon and the carrier gas (hydrogen) concentration were very close to one another.

The correlation coefficients between the values of AEF and radon volumetric activity in two profiles were: $k(E, \mathrm{Rn})_{\mathrm{I\text{-}I`}} = -0.66$ and $k(E, \mathrm{Rn})_{\mathrm{II\text{-}II`}} = -0.58$. These correlation coefficients are not very large, but are significant. The reason for their small value is, most likely, due the noise effects of dust formations and exhaust gases—field measurements were performed in the daytime on highways with high traffic.

As noted above, in addition to the rapid measurement of hydrogen, radon, and the AEF, in the work done on the Kaluga Ring Structure, the soil air was sampled at eight observation pickets for subsequent laboratory analysis. Figure 1.2.2 shows the results of this analysis for methane, hydrogen, nitrogen, and carbon dioxide.

The volatile gas contents given in Figure 1.2.2 would be more correctly presented as histograms—the observation pickets 1–8 are taken from different profiles with distances between them of 0.5 km to 18 km. The broken curves in Figure 1.2.2 are given to emphasize the observed correlative relationships and their absence.

The results obtained convincingly support the synchronism of methane and hydrogen content variations in the samples. The correlations of the variations of these two volatile gases with changes in the carbon dioxide and nitrogen contents, concentrations which are orders of magnitude higher, are completely absent. Concentrations of nitrogen and carbon dioxide change in opposition and manifest a rigorous correlation: $k(N_2; CO_2) = -0.99$ in the absence of a correlation with methane and hydrogen, $|k(H_2; N_2)| = 0.28$; and hydrogen, $|k(H_2; CO_2)| = 0.29$.

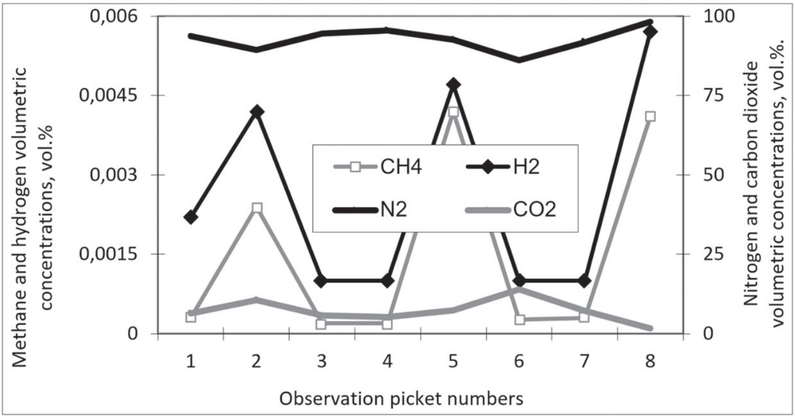

Figure 1.2.2: Concentrations of volatile gases of soil air obtained by laboratory analysis of eight samples taken at the Kaluga Ring Structure.

The correlation coefficient of hydrogen and methane is very high: $k(H_2; CH_4) = 0.97$ (Figures 1.2.2., 1.2.3). The correlation coefficients between the concentrations of two volatile gases and radon volumetric activity at eight pickets under consideration are also very high: $k(Rn; H_2) = 0.84$; $k(Rn; CH_4) = 0.90$. A slight decrease in the correlation coefficients, when compared to the graphs in Figure 1.2.2, has a clear physical explanation—the accuracy of hydrogen and methane concentrations determined in the laboratory is much higher than that of the field measurements for the volumetric activity of radon.

The results obtained allow us to refine the model of the relationships between the studied characteristics of the ground and the atmosphere. At the stage of setting up a test, it was believed that radon transfer to the surface soil layers and the surface atmosphere was performed by bubbles of all volatile gases in the soil air [43]. The measurement results shown in Figure 1.2.3 allow us to limit the number of carriers to two gases: hydrogen and methane. It makes sense that the conclusions formulated should therefore be considered preliminary and requiring further verification.

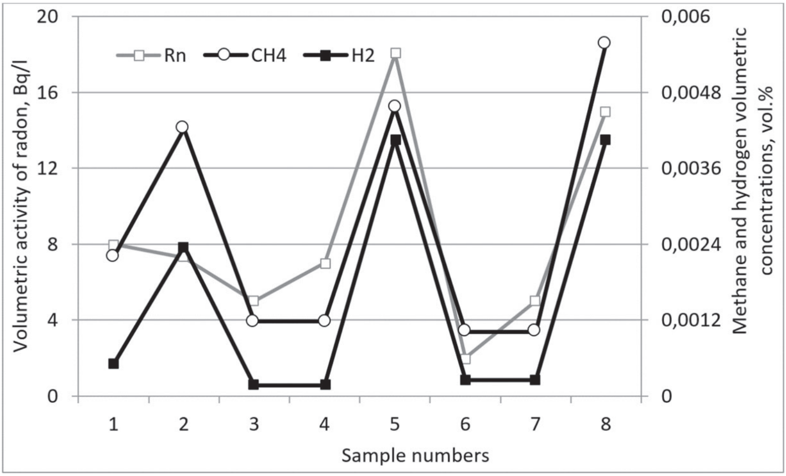

Figure 1.2.3: Variations in hydrogen and methane concentrations and radon activity at eight pickets of the Kaluga Ring Structure.

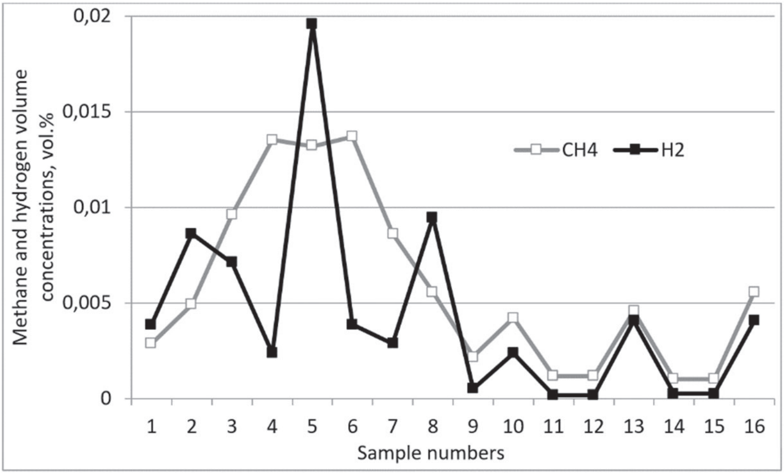

Figure 1.2.4: Results of analysis of soil air sampled in the area of the Schelkovo GSF (1–8) and at the Kaluga Ring Structure (9–16).

At first glance, the model of the relationships between methane, hydrogen, radon, and AEF performed in 1999 on the territory of the Schelkovo Gas Storage Facility (GSF) was not reliably verified by the experiment. Figure 1.2.4 shows the combined results for the samples from the Kaluga Ring Structure and the area of the Schelkovo GSF.

The correlation coefficient between two 16-point data arrays is significant—$k(\mathrm{Rn}; \mathrm{H_2})_{16} = 0.56$, although it is rather low. This increases to $k(\mathrm{Rn}; \mathrm{H_2})_{12} = 0.96$ if the analytical results of samples 3, 4, 6, and 7 are discarded from the arrays.

The analyzed array data of field observations is too small to make definitive conclusions, but it confirms the hypothesis of the relationship between methane and hydrogen and a sub-vertical flow of volatile gases. This relationship has been empirically established: 12 pairs of points in Figure 1.2.5 with a confidence level of $D = 0.91$ can be expressed by the linear dependence $CH_4 = 0.566 \times H_2 + 0.0014$ [vol. %]. Figure 1.2.5 shows the measured and calculated values of methane concentration according to the linear expression obtained.

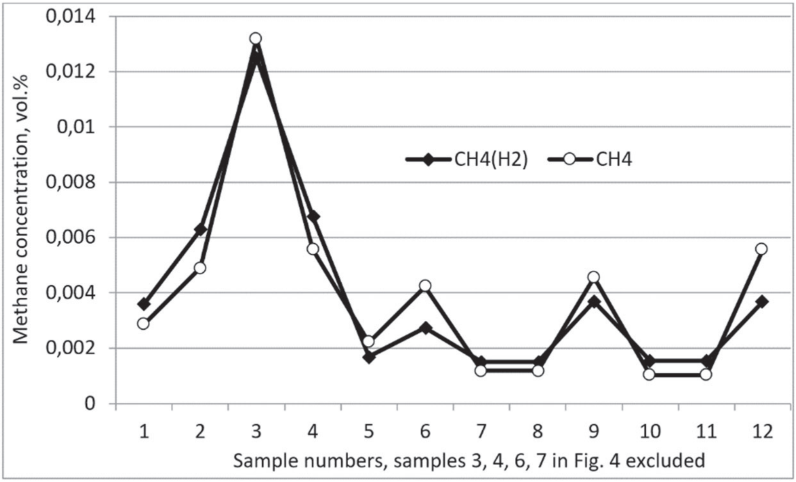

Figure 1.2.5: Methane concentrations, measured and calculated by the linear equation introduced.

Figure 1.2.6: Cracking of the soil at the North Stavropol GSF site and the Pelagiadian structure in August 2001.

Information on the hydrogen content of the soil can be obtained both from the results of laboratory analysis and from the data of rapid field observations using modern measuring equipment [37–39]. To obtain reliable results at the transition from the data from field measurements of hydrogen to data on the absolute values of methane, additional calibration of the sensor is required using material from laboratory analysis of the same samples. Moreover, based on the results of the initial experiments, the relationships between the two volatile gases can be used to solve the problem of indirect control of soil methane outside hydrocarbon accumulations.

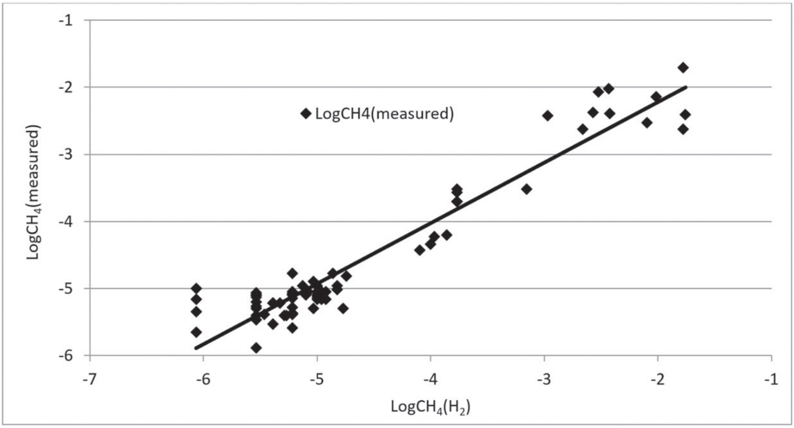

Figure 1.2.7: Linear approximation of logarithms of measured values of methane content, $LogCH_4$(measured); and calculated values of methane content, $LogCH_4$ $(H_2)CH_4$(measured) = 0.903 × $CH_4(H_2)$ - 0.4142; accuracy of approximation $D = 0.92$

In the course of fieldwork at the site of the North Stavropol GSF and Pelagiadian structure in 2006 and 2007, research into the relationships between methane and hydrogen in soil air was continued. At first glance, the choice of the area above the GSF Facility for such experiments may not be considered advantageous for research. However, the North Stavropol GSF Facility was established in a reservoir bed of the depleted North Stavropol Deposit, chosen by nature for the storing of flammable gas—this made it possible to obtain high-quality field material.

In August 2006, due to drought conditions in the Stavropol Territory, it was not possible to measure the soil air hydrogen at the GSF site and the Pelagiadian structure. Due to the cracking of the soil and soil air discharge from cracks, the hydrogen content in the samples was lower than the measuring device sensitivity of 10^{-4} vol. (Figure 1.2.6) [37, 38].

Nevertheless, at 16 pickets located at the GSF site, eight pickets at the Pelagiadian structure, and four pickets on the slopes of Ust-Nevinsky Farm, 28 soil air samples were taken for subsequent laboratory analysis of hydrogen and methane content, with a sampling sensitivity higher than ~10^{-6} vol. %.

Before sampling at the 300 observation pickets of the research sites, simultaneous observations of soil and atmospheric radon were made. The results were used in the selection of sampling pickets for laboratory analysis of soil air. The selection criteria were the maximum and minimum ratios of volumetric activity of soil radon to volumetric activity of atmospheric radon.

A similar procedure was carried out in June 2007 with 500 observation pickets this time. Using the same criteria, 24 samples of soil air were taken for subsequent laboratory analysis of the hydrogen and methane content. The presence of 72 data pairs on the content of hydrogen and methane in the samples obtained at the Kaluga Ring Structure, in Schelkovo, and the Stavropol Territory allows us to make a general analysis of the arrays. The correlation coefficient $k(CH_4,H_2)_{72} = 0.76$ is quite high. The correlation coefficient of the logarithms $\mathrm{Log}(H_2)$ and $\mathrm{Log}(CH_4)$ increases to $k[\mathrm{Log}(H_2), \mathrm{Log}(CH_4)] = 0.96$.

The construction of a linear approximation of logarithms of hydrogen and methane content measured in the soil allows us to construct a relationship between the studied parameters, with a confidence level of $D = 0.92$:

$$CH_4 = 15.83\exp[1.675\mathrm{Log}(H_2)], \text{[vol. \%]} \tag{1.2.1}$$

where hydrogen (H_2) concentration is normalized by 1 vol.%.

Figure 1.2.2 shows plots of the methane content in the soil from 72-point data sets measured and calculated by Eq. (1.2.1). The graph in Figure 1.2.8 has an intentional break in order to visually separate low concentrations of methane of (10^{-6}–10^{-5}) vol.% obtained in the samples from the North Stavropol GSF and methane concentrations of (10^{-4}–10^{-2}) vol.% in the samples taken near Kaluga, Schelkovo, and on a landslide slope near the Ust-Nevinniy Farm in the Stavropol Territory.

The difference in methane concentrations in the analyzed samples is vast—about four orders of magnitude, (10^{-6}–10^{-2}) vol.%. Of course, the expression in (1.2.1) requires further verification. It is necessary, in particular, to obtain supplementary field material on the range of soil methane concentrations (10^{-5}–10^{-3}) vol.%.

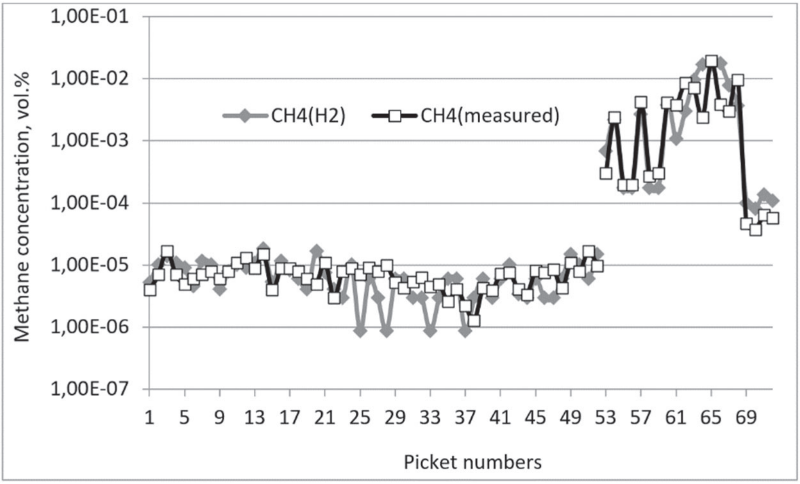

Figure 1.2.8: Calculated and measured values of methane content in the soil. The straight line shows the average background level of methane in the soil.

In support of the stated relationship between hydrogen and methane, some facts should be emphasized. Different operators sampled soil air under different weather conditions, and the analysis was carried out at different laboratories. All this allows an assumption that the results obtained are ‘ideal.’ Rejection of some points (samples 25, 28, 33, and 37 collected in 2006 at the Stavropol Gas Storage Facility) is due to the recorded concentrations falling around the sensitivity limit of the measuring equipment and thus may be erroneous.

The exponential relationship obtained between methane and hydrogen is clear. In the stationary state, the distribution of sub-vertical deep flow gases in the geological environment, as they move from the source to the surface, as well as in the atmosphere, can be described by the “barometric formula.” Of course, in a porous medium, distribution yielding to a stationary state will take a significantly longer time. Moreover, during the development of the North Stavropol Gas Field, concentrations of combustible gas at different depths were estimated using the barometric formula [49].

If differences in concentrations are insignificant—within an order of magnitude—both at low contents (56 samples taken at the North-Stavropol Gas Storage Facility (10^{-6}–10^{-5} vol.%) and extensive materials (16 samples from the Kaluga Ring Structure and Schelkovsky GSF, (10^{-3}–10^{-2}) vol.%, the exponent can be reliably approximated using the first members of the series.

Studies into the relationships between soil air hydrogen and radon and AEF have used the most general concepts of the surface atmospheric electricity theory [20–23]. It was believed that exhaled soil radon was the only natural ionizer of surface air. According to estimates [20], up to altitudes of 0.5 km, 75 % of the air is ionized by gamma radiation from soil radon and 25 % by cosmic radiation. In the altitude range of 0.5 km to 1.0 km, the situation changes—64 % of the air is ionized from space and only 36 % by soil radon.

The distribution of parent matter determines the presence of radon in the Earth’s crust. According to research data from the Academician Vernadsky Biogeochemical Laboratory on radium distribution in the Earth’s biosphere, the concentration of radium in rocks falls within the range 10^{-9} % to 10^{-10} %; in soils this is only an order of magnitude less: 10^{-10} % to 10^{-11} %. In clay, in particular, which is an aquiclude of aquifers, the average radium content is 1.3×10^{-10} %, which is twice as low as in granites: 2.58×10^{-10} % [50].

The material shown allows us to develop a model of hydrogen-methane-radon and atmospheric-electrical relationships. The processes of sub-vertical hydrogen and methane flow capture radon at a depth of several meters and lift it to the subsurface soil layers and the atmosphere. Light ions are formed there and determine polar conductivities; their recombination with neutral condensation nuclei creates heavy ions and this is mainly responsible for AEF (Table 1.2.1).

Radon concentration in the soil is at least two orders of magnitude higher than in the atmosphere [47, 48]. This means that the two-fold change in the ionizer efflux to the atmosphere will not affect the radon content in the soil at all. However, in the surface atmosphere, such changes will lead to a two-fold difference in the radon concentration—to a two-fold variation in the polar conductivities and field. To put it differently, the surface atmospheric electricity elements are susceptible to changes in the sub-vertical flow density of carrier gases—hydrogen and methane.

Table 1.2.1. Modelled representation of the relationships between hydrogen, methane, radon, and surface atmospheric electricity elements

Polar conductivities and atmospheric electric field at heights of decimeters to meters. The real installation height of the measuring devices
The Earth's surface
Subsurface soil layers—the zone of capture and efflux of radon to the atmosphere
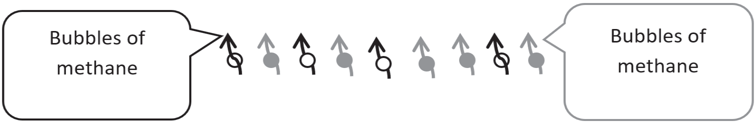 Hydrogen and methane sub-vertical flow

Based on the experimental results, the model of the relationships between hydrogen, methane, radon, and surface atmospheric electricity elements allows us to make several preliminary conclusions. The soil-atmosphere air exchange determines the space charge of the surface air layer. The magnitude of this charge depends on the content of the parent substance in the surface layers of the soil and radon ionization. Bubbles of two volatile gases transport radon that have no relation to electricity. Thus, the volumetric air charge at the Earth's surface is related to the density of sub-vertical flows of the carrier gases—hydrogen and methane.

When solving the problem of atmospheric-electrical monitoring of geological heterogeneities and zones of geodynamic processes, radon will act as an intermediary in the surface soil layers. In fair weather conditions, changes in the atmospheric electric field or polar conductivities of air are determined solely by variations in the density of the sub-vertical fluxes of volatile carrier gases.

1.3. AEF Sensitivity to Changes in the Density of Hydrogen and Methane

The model of the relationships between the gas and electrical parameters of the Earth and the atmosphere was developed based on the theory of surface atmospheric electricity. The data from complex observations show that the space charge of surface air is extremely sensitive to changes in the density of sub-vertical flows of hydrogen and methane. At the same size, bubbles of methane will be eight times heavier than bubbles of hydrogen. This means that other conditions being equal, the probability of radon transport by hydrogen will be eight times greater [51]. We checked this rough estimate against the results of experimental observation.

The first measurement cycle at the North Stavropol Gas Storage Facility was carried out in October 2001. Here, at 43 Klubnichnaya Street, Pelagiada Farm, a methane gas discharge appeared [41]. To suppress methane efflux several months before the start of work at the site of the emergency, a small relief well, No. 1, was drilled, as shown in Figure 1.3.1. Methane coming through it was drawn off and burnt.

From interviews with residents, it turned out that at a site located a distance of 60–70m eastward from a damaged and failing building, for several years "earth combustions" from a discarded cigarette butt or match had been observed. Most often, this "combustion" occurred after blasting at the Pelagiadsky Mayak opencast mine, located up the slope on a plateau, 1.0–1.5 km southwards of the surveyed area. The seismic effects of explosions intensified the soil-atmosphere air exchange, including the observed discharge of methane to the surface atmosphere.

In the course of the survey by specialists of Kavkaztransgaz, the probable direction of the methane inflow to the relief well from the northwest was established. An annulus with a diameter of about 30 m was laid along the probable line of gas release. The layout of the observation annulus and the relief well is shown in Figure 1.3.1.

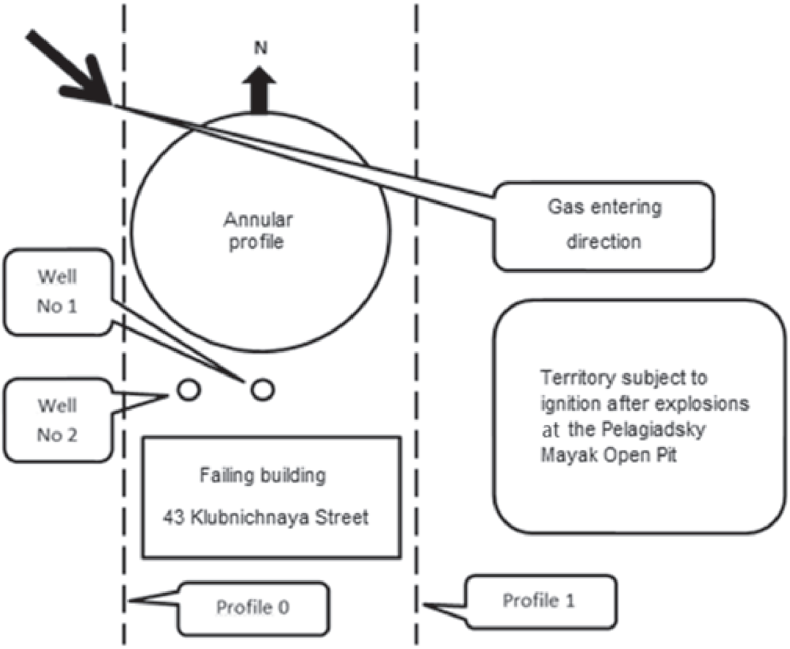

Figure 1.3.1: The layout of the relief well and the observation annulus at the site of the failing building located at 43 Klubnichnaya Street.

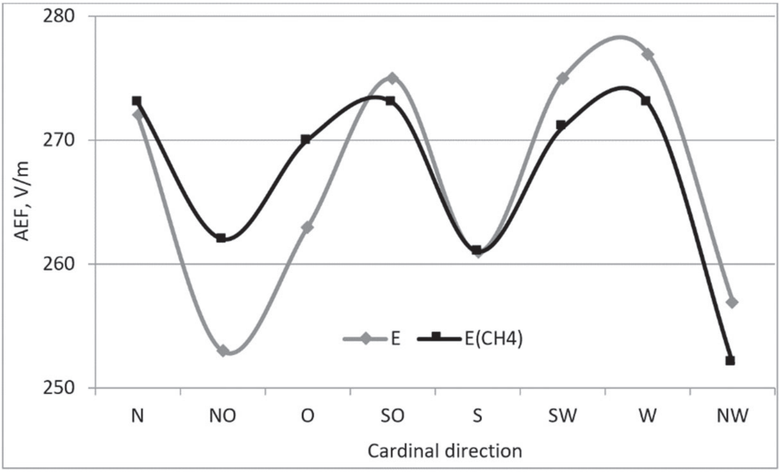

Figure 1.3.2: Measured and calculated *E* and calculated *E*(CH_4) values of the atmospheric electric field from the annular profile above relief well No.1.

Experts with Kavkaztransgaz found a probable direction of methane inflow to the relief well from the northwest. An observation annulus (Figure 1.3.1), with a diameter of about 30 m, was laid along this probable line of gas inflow. The AEF was measured twice in the annulus and samples of the soil air were taken in a number of directions for subsequent laboratory analysis of their hydrogen and methane content. Figure 1.3.2 shows the AEF values, measured and calculated as a function of the soil methane content. The correlation coefficient of the measured and calculated values of the field is $k[E; E(CH_4)] = 0.83$.

The AEF measurements show that the minimum value of the monitored parameter appears in the northwest direction, which is the line of methane inflow to the collapsed building. Two additional field minimums appeared in the south and northeast directions. These are directions to relief well No.1 and to the site where a "combustion" event was observed after blasting at the Pelagiadsky Mayak opencast mine.

The high level of correlation between methane and AEF suggests that in the survey area, transfer of the ionizer is mainly carried out by bubbles of combustible gas—the participation of hydrogen in transmission is minimal. Variations in methane concentration have a more significant effect on field changes.

With a confidence value of $D = 0.78$, AEF is set by the function $E(CH_4) = 152.33CH_4^{-0.082}$ [V/m]; the value of CH_4 is normalized to 1 vol.%. The field derived by the methane concentration is presented as $dE/dCH_4 = 152.33 \times (-0.082)CH_4^{-1.082}$ [V/m (vol.%)].

Long-term observation of the AEF shows that, in fair weather conditions [26–28], the dispersion in the current readings of the measuring device at the observation picket does not exceed 0.5 to 1.0 V/m. The reasons for this dispersion are purely meteorological, involving changes in wind velocity alongside the density of heavy ions. A change in AEF of $\Delta E = 2.0$ V/m was taken as the field threshold; this was fixed according to variations in the carrier gas density. Using the derivative obtained for the mean values of the methane concentration at the location studied, the calculations identified changes in the methane concentration of $\Delta CH_4 = 1.13 \times 10^{-5}$ vol.%. This is 10 % of the average methane concentration at eight pickets along the annulus with the field change and a threshold value of $\Delta E = 2.0$ V/m.

According to the laboratory data, the average hydrogen content of the annulus was $H_2 = 0.000024$ vol.%, which is 47 times less than the methane content at the eight observation pickets. This result suggests that the transfer of radon in the survey area is carried out exclusively by methane bubbles.

The results of AEF, radon, and hydrogen observation were similarly analyzed for an observation profile with abnormal changes in volatile gases, but, on average, absolute values that were close together. This is location 18 at the North Stavropol Gas Storage Facility, which expands beyond the boundaries of the reservoir bed to the surface ground. The average values of hydrogen recorded here were $H_2 = 0.0000103$ vol.%, while methane $CH_4 = 0.0000108$ vol.%. The abnormal variations in the monitored parameters of the location are associated with the observational route beyond the limits of the reservoir bed to the ground surface. Figure 1.3.3 shows the measured and averaged AEF variations for profile 18.

The correlation coefficients of AEF and gas parameters are quite high: $k(E; CH_4) = 0.70$; $k(E; H_2) = 0.67$. The results prove the reliability of detecting the causal relationships between hydrogen, methane, radon, and surface atmospheric electricity elements.

We repeated the treatment of the observation data, approximating the AEF measurements as a function of the soil methane content. The field was approximated by the power function $E = 0.712CH_4^{-0.501}$ [V/m] with a confidence value of $D = 0.81$; values for methane were normalized to 1 vol.%; a field derivative for methane concentration was $dE/dCH_4 = 0.712\times(-0.501)\times CH_4^{-1.501}$ [V/m vol.%]. For an average value of methane concentration, a field change by 2.0 V/m was caused by a change in the average value of methane concentration of 18 %.

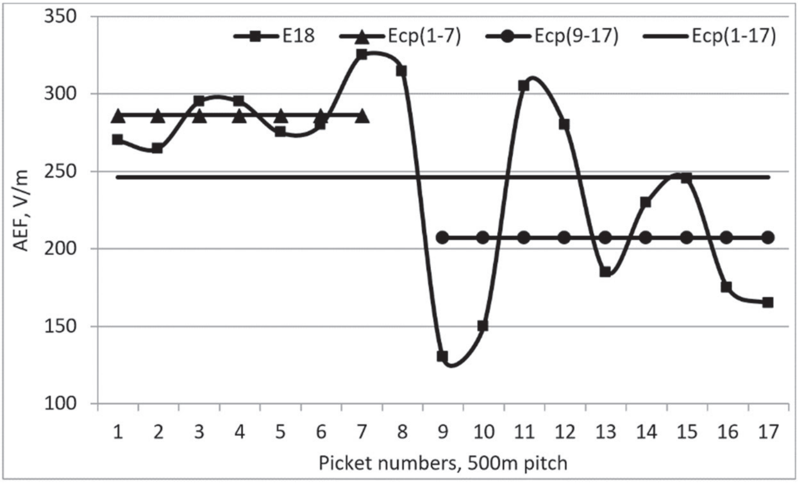

Figure 1.3.3: The measured and average AEF values at a profile that extends beyond the reservoir bed of the North Stavropol GSF (the former North-Stavropol Field).

Similar calculations for hydrogen, the second carrier gas for radon, gave the expression $E = 7.4607H_2^{-0.378}$ [V/m] with a confidence value of D = 0.83; the values for hydrogen were normalized to 1 vol.%; $dE/dH_2 = 7.46 \times (-0.378) \times H_2^{-1.378}$ [V/m vol.%]. A field change of 2.0 V/m was caused by variations in the soil hydrogen concentration of 2.6 % relative to the mean value.

The result obtained is clear. The molecular weight of hydrogen is eight times less than the molecular weight of methane. Since the carrier gas bubbles also carry their weight, the probability of the ionizer being captured and discharged to the atmosphere by hydrogen is higher than by methane. This is the reason for the high sensitivity of changes in AEF to variations in the density of a sub-vertical hydrogen flux. In particular, for the case under consideration, this value can be estimated from the ratio of percentages of hydrogen and methane, which is equal to about 6.9. It seems that this figure is roughly correct. Following the estimates of the North Stavropol Gas Storage Facility (survey of 800 pickets over two years of operation), 15 % of radon was transferred by methane and 85 % by hydrogen (85/15 = 5.7). For clarity, the estimates obtained are summarized in Table 1.3.1.

Table 1.3.1. The sensitivity of AEF to changes in the concentrations of hydrogen and methane in the surface soil layer

	Average hydrogen, vol.%	Average methane, vol.%	Sensitivity, *E*, to hydrogen variations	Sensitivity, *E*, to methane variations	H_2/CH_4
Annular profile	0.000024	0.00113	-	$\Delta CH_4 = 9.02\times10^{-5}$ vol.% – 8% of CH_4(ave) $\Delta E = 2.0$V/m	0.02
Profile 18	0.0000103	0.0000108	$\Delta H_2 = 4.0\times10^{-6}$ vol.% – 2.6% of H_2(ave), $\Delta E = 2.0$V/m	$\Delta CH_4 = 1.91\times10^{-6}$ vol.% – 18% of CH_4(ave) $\Delta E = 2.0$V/m	0.95
Profile 4	0.000493	0.0000828	$\Delta H_2 = 1.48\times10^{-5}$ vol.% – 2.8% of H_2(ave), $\Delta E = 2.0$V/m	$\Delta CH_4 = 8.29\times10^{-5}$ – 100% of CH_4(ave), $\Delta E = 0.26$V/m	5.95

At profile 4, at the site of the North Stavropol Gas Storage Facility, the average concentration of hydrogen, $H_2 = 0.000493$ vol.%, being almost six times higher than the average concentration of methane, $CH_4 = 0.0000828$ vol%. Power approximation of AEF and methane gave the expression $E = 0.0833 \times CH_4^{-0.265}$ [V/m] with a confidence value of $D = 0.73$; the methane concentration was normalized to 1 vol.%; the methane derivative was $dE/dCH_4 = -0.02207 \times CH_4^{-1.265}$ [V/m vol.%]. For the average methane concentration $CH_{4(ave)} = 8.28 \times 10^{-5}$ vol.% even a 100 % deviation from the mean value only leads to a field change of 0.3 V/m in the data under consideration.

The AEF power dependence on the soil hydrogen concentration gives the expression $E = 19.4\times H_2^{-0.321}$ [V/m] with a confidence value of D = 0.72; the hydrogen content was normalized to 1 vol.%; $dE/dH_2 = -6.23H_2^{-1.321}$ [V/m vol.%]. For the average hydrogen content of the data under consideration, $H_2 = 4.93 \times 10^{-4}$ vol.%; deviation of the soil hydrogen content from the average value by 2.8 % causes AEF variations of ΔE = 2.0 V/m. For the convenience of comparing the estimated results, they are summarized in Table 1.3.1 [36, 52].

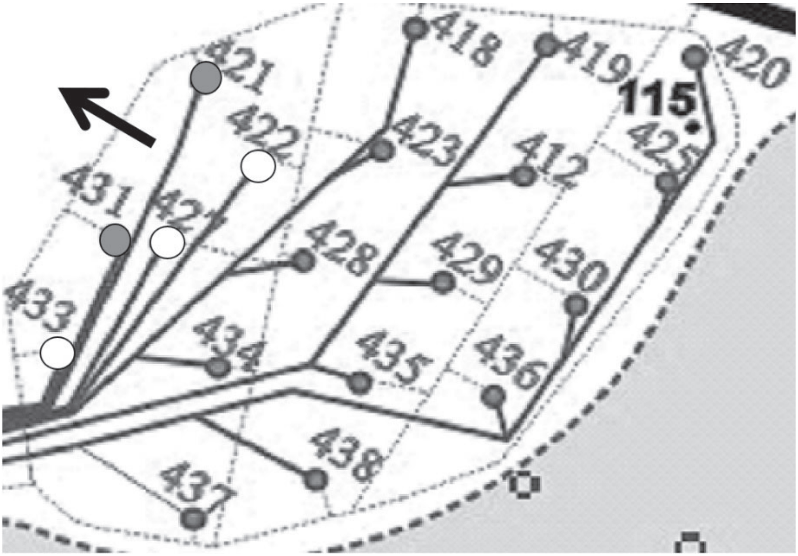

Figure 1.3.4: Plan for 19 injection wells at the site of the Kasimov GSF. The arrow shows the direction of gas discharge to the dome of the gas storage facility.

At the last stage of calculations, dealing with AEF sensitivity to changes in the density of sub-vertical flows of carrier gases, we estimated the case of relatively high concentrations of hydrogen and methane. In the autumn of 2009, a set of hydrogen-radon and atmospheric-electrical measurements were taken at the site of the 4th stage of the Kasimov Gas Storage Facility. Measurements began one day after the completion of a weekly injection cycle. Gas observations in the area of 19 injection wells were carried out over 4.5 days (with about 34 pickets per day), as shown in Figure 1.3.4.

Due to the discharge of the injected gas to the dome structure of the cover, the soil-atmosphere air exchange during this period was subject to great changes (the dynamics of gas efflux will be discussed in Chapter 4). To obtain a picture of the quasi-instantaneous air exchange, on the last day of work, a mobile survey of AEF was performed at 152 pickets (eight pickets around each well). The measurements were carried out in ideal weather conditions—a windless autumn day with no cloud. The average field values for wells Nos. 431 and 421 turned out to be equal to $E_{431.421}$ = 304 V/m; the average value for the remaining wells was E = (451 +/- 11) V/m; and the average value for wells Nos. 433, 427, 422 was $E_{433,\ 427,\ 422}$ = 468 V/m (Figure 1.3.4). The results obtained suggest that at the time of the measurements, the combustible gas had virtually left the injection well cluster and remained only on the line of wells Nos. 431, 421—the exit direction towards the northwest is towards the dome area of the gas storage facility.

Gas observations around wells Nos. 433, 427, and 422 and wells Nos. 431 and 421 (performed on the last day) provided an estimate of field sensitivity to changes in carrier gas concentrations: ΔH_2 = 0.000106 vol.% to 8.4 vol.% of H_2(ave); ΔCH_4 = 0.000089 vol.% to 0.98 vol.% of CH_4(ave). The average concentration ratio of hydrogen and methane was $H_2/CH_4 = 0.21$.

AEF observations were performed in the morning. A preview of the results indicated the need to make repeated gas observations at wells Nos. 433, 427, 422, 431, 421, which were done in the second half of the day using a shortened scheme—four pickets around each well. The correlation coefficient between the soil methane content and AEF at five wells turned out to be very high: $k(E; CH_4) = -0, 97$; the field and hydrogen correlation coefficient changed the sign of $k(E; H_2) = 0.76$. The reason for the result obtained is that during the time interval between making atmospheric-electrical and gas observations, gas residues from wells Nos. 431 and 421 were discharged to the dome of the reservoir bed. The surface pore spaces relaxed to their original state (before the injection cycle).

During the years of operation of the gas storage, due to leaks from the reservoir, the methane content in the surface soil layers had increased by almost two orders of magnitude [41]. To illustrate this growth, Figure 1.3.5 shows the results of laboratory analysis of soil air samples for the content of hydrogen and methane in the experimental profile outside the reservoir bed. The curves do not correlate with each other and the average excess methane content, when compared to hydrogen content, was CH_4/H_2 ~19. It is naturally expected that in a gas storage area, and even more so at the site of a cluster of injection wells during a period of gas injection and discharge, such a ratio will be subject to significant changes. These changes affect the relationships between hydrogen, methane, and AEF at the site of five allocated injection wells, the measurement data of which were obtained with a delay of several hours. In this case, methane, by definition, acts as the primary carrier of radon to the surface atmosphere and there is a high correlation coefficient between the field and methane. Due to apparent contradictions in the estimates, the result on AEF sensitivity to changes in the methane flux density are only considered qualitatively: with relatively high concentrations of carrier gases in the surface soil layers, the field sensitivity to variations in the levels of hydrogen and methane increases.

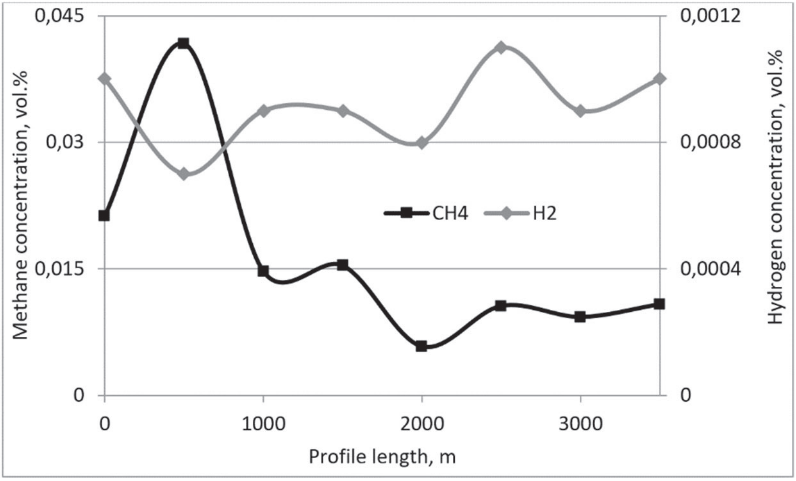

Figure 1.3.5: Methane and hydrogen content at the test profile outside the reservoir of the Kasimov Gas Storage Facility.

The results of field observations fully confirmed the model of hydrogen, methane, radon, and the atmospheric electric field relationships; as well as the calculations performed.

The main carrier gas of radon in surface soil layers and the atmosphere is hydrogen, the molecular weight of which is eight times less than the molecular weight of methane. According to the assessments made from observational results at the North Stavropol GSF, hydrogen bubbles transfer 5.7–6.9 times more ionizer than methane bubbles.

According to the classification of the surface gas halos (Russian GOST 12.01.044-89 5541-87), the standard fully complies with the international standard IEC 79-4-75* for determining the self-ignition temperature of gases and liquids. The minimum background permissible concentrations of methane (0.001–0.05 vol.%) can confidently be recorded from AEF changes with variations in the content of combustible gases at the level of the first percent.

1.4. References to Chapter 1

1. Milne, J. Earthquakes in connection with electric and magnetic phenomena, *Trans. Seismol. Soc. Jap.*, 1890, **15**, 135-164.
2. Chernyavsky, E.A. Atmospheric-electrical and electrotelluric phenomena in the course of earthquakes, *Sotsialisticheskaya Nauka i Tekhnika* (*The Socialist Science and Technology*), 1936, **112**, 26-35. [in Russian]
3. Chernyavsky, E.A. Atmospheric-electrical earthquake precursors, *Meteorology and Hydrology in Uzbekistan*, Tashkent, Izdatelstvo AN UzSSR, 1955, 317-327. [in Russian]
4. Mavlyanov, G.A. *The Earthquake in Tashkent on April 26*, 1996, Tashkent, FAN, 1971, 672p. [in Russian]
5. Bonchkovsky V.F. Measurements of the electric potential gradient in the atmosphere as one of the possible precursors, *Trudy Geofizicheskogo Instituta AN SSSR* (*Proceedings of the Geophysical Institute Academy of Sciences of the USSR*), 1954, **25** (152), 192-206. [in Russian]
6. Bonchkovsky, V.F. *Earthquakes and Methods of Their Study*, Moscow, Izdatelstvo AN SSSR. 1949, 88p. [in Russian]
7. Sidorin, A.Ya., About perturbations of the electric potential gradient of the Gharm Test Range atmosphere in 1949-50. In Coll.: *Electrical Interaction of Geosphere Shells of the Earth*, Moscow, Izd. IPE RAS, 2000, 148-165. [in Russian]
8. Sadovsky, M.A., and Nersesov, I.L. The Issues of earthquake forecasting, *Izv. AN SSSR* (*Review of Academy of Sciences of the USSR*), *Ser. Physics of the Earth*, 1978, **9**, 13-30. [in Russian]
9. Hao, J.G. Near earth surface anomalies of the atmospheric field and earthquake, *Acts Seismol. Sin.*, 1988, **1**(2), 48-54.
10. Hao, J.G., Zhang, Y.F., Li, D.R., Tang, T.M., and Liu, X.Q. Ultra-low-frequency electromagnetic wave anomaly and its spectrum characteristics before earthquakes, *Acts Seismol. Sin.*, 1995, **8**(1), 101-109.
11. Hao, J.G., Tang, T.M., and Liu, X.Q. A kind of information on short-term and imminent earthquake precursors—research on atmospheric electric field anomalies before earthquakes, *Acts Seismol. Sin.*, 1998, **11**(1), 121-131.
12. Hao, J.G. Near earth surface anomalies of the atmospheric field and earthquake, *Acts Seismol. Sin.*, 1988, **1**(2), 48-54.
13. Hao, J.G., Tang, T.M., and Liu, X.Q. A kind of information on short-term and imminent earthquake precursors—research on

atmospheric electric field anomalies before earthquakes, *Acts Seismol. Sin.*, 1998, **11**(1), 121-131.

14. Kondo, G. The variation of the atmospheric electric field at the time earthquake, *Kakioka Magn. Observ. Mern.*, 1968, **13**(1), 11-23.
15. Bufe, C.G., and Manevicz, J. Atmospheric electric field observations, animal behavior, and earthquakes, *Abnormal Animal Behavior Prior to Earthquakes*, Menlo Park: USGS, 1976, 95-106.
16. Vorobiev, A.A., and Remizov, V.P. Changes in the atmospheric electric field as a possible precursor of earthquakes, *Electromagnetic Fields in the Biosphere*, Moscow, Nauka, 1984, **1**, 311-315. [in Russian]
17. Rulenko O.P., Ivanov A.V., and Shumeiko A.V. Short-term atmospheric-electrical precursor of the Kamchatka earthquake happened on 6.III.1992, M=6.1, *Doklady RAN*, 1992, **326**(6), 980-982. [in Russian]
18. Rulenko O.P., Druzhin G.I., and Virshinin E.F. Measurements of atmospheric electric field and natural electromagnetic radiation prior to the Kamchatka earthquake happened on 13.11.1993, M=7.0, *Doklady RAN*, 1996, **348**, 814-816. [in Russian]
19. Imyanitov I.M., and Chubarinov E.V. *Free Atmosphere Electricity*, Leningrad, Gidrometeoizdat, 1965, 240p. [in Russian]
20. Tverskoi P.N. *The Course of Meteorology*, Leningrad, 1951, Gidrometizdat, 887p. [in Russian]
21. Frenkel Ya.I. *The Theory of Atmospheric Electricity Phenomena*, Leningrad, GITTA, 1949, 155p. [in Russian]
22. Chalmers J. *Atmospheric Electricity*, Gidrometizdat, 1974, 327p. [in Russian]
23. Shcherbakov D. Discoveries of radioactive mineral deposits by special survey methods, *Priroda*, **7-12**, 1923, 97-100. [in Russian]
24. Shuleikin V.N. Soil air polar conductivities observation results within boundaries of urban development, In Coll.: *Development of Methods and Means of Experimental Geophysics*, Moscow, 1996, **2**, 235-240. [in Russian]
25. Nikolayev A.V., Urdukhanov R.I., and Shuleikin V.N. Results of atmospheric electricity and seismic profiling of ore body, *Proc. 8-th Int. Conf. Atm. EI.*, Uppsala, 1988, 138-140. [in Russian]

26. Imyanitov I.M., and Shifrin K.S. The Modern State of Research of Atmospheric Electricity, *Uspekhi Fizicheskikh Nauk*, 1962, **4**, 593-642. [in Russian]
27. *The Guide for Surface Observations of Atmospheric Electricity Elements*, Leningrad, Izdatelstvo GGO im. A.I. Voeykova, 1960, 95p. [in Russian]
28. Semenov K.A. Good Weather and Atmospheric Electricity Elements, *Proc. GGO im. A.I. Voeykova*, 1982, **455**, 112-119. [in Russian]
29. *Observation Results for Surface Atmospheric Electricity (Global Network)*, Leningrad, GGO im. A.I. Voeykova, 1982-1992. [in Russian]
30. Strus' A.I. Variations of the electrical conductivity of the surface atmosphere with the electrode effect in the range of geomagnetic pulsations, *Candidate Dissertation Thesis*, Izd. IPE AS USSR, 1988, 188p. [in Russian]
31. Morgunov V.A. *et al.* Studies of pulsations of electrical parameters of the surface air layer, In Coll.: *The Structure of the Electromagnetic Field of Geomagnetic Pulsations*, 1980, M., Nauka, 148-157. [in Russian]
32. Tammet H.F. On the theory of measuring the intensity of an atmospheric electric field, *Uch. Zap University of Tarusa*, 1970, Iss. Tarusa University, 1970, **240**, 140-156. [in Russian]
33. Shvarts Ya.M. Methods and apparatus for measuring atmospheric electricity elements, In Coll.: *Atmospheric Electricity*, 1976, Leningrad, Gidrometizdat, 59-70. [in Russian]
34. Shuleikin V.N. Differential antenna for measuring the air-earth current of the surface atmosphere, *Proc. III All-Union Symposium on Atmospheric Electricity*, Tartu, 1986, 40. [in Russian]
35. Shuleikin V.N., Shchukin G.G., Kupovykh G.V. *Development of Methods and Means in Applied Geophysics – Atmospheric-Electrical Monitoring of Geological Heterogeneities and Geodynamic Process Zones*, Saint-Petersburg., Publ. TsOP RGGMU, 2015, 206p. [in Russian]
36. Shuleikin V.N. *The Earth and Atmospheric Electricity*, New York, Nova Science Publishers, 2018, 143p.
37. Nikolaev, I.N., and Litvinov, A.V. Technique of measuring low H_2 and H_2S concentrations above the water surface, *Measurement Equipment*, 2004, **5**, 54-60. [in Russian]
38. Nikolaev, I.N., Litvinov, A.V., and Khalfin, T.M. Automated hydrogen gas detectors in the range of 10^{-6}-1.0% volumetric

concentrations, *Measurement Equipment*, 2004, **7**. [in Russian]

39. Nikolaev, I.N., Kalinina, L.N., and Litvinov, A.V. MIS-sensors for measuring hydrogen concentrations in the range of 10^{-4}-10^{2} vol.%, *Journal “Sensors and Systems,”* 2004, **12**, 48-52. [in Russian]
40. Voitov, G.I., Gusev, A.S., Shuleikin, V.N. et al. Emanation (hydrogen-radon) and electric effects above complex tectonic structures (on the example of Alexandrovskaya zone of pre-fault elevations, Belarus), *DAN RAN*, 2000, **370**(1), 105-108. [in Russian]
41. Zubarev, A.P., and Shuleikin, V.N. *Complex Geophysical and Geochemical Monitoring for Underground Gas Storage Facility Operation*, Moscow, Izd. Gasprom GSF OOO, 2009, 264p. [in Russian]
42. Voitov, G.I., Rudakov, V.P, Shuleikin, V.N., Kozlova, N.S., and Baranova, L.V. Emanation and electric effects in the subsoil atmosphere above the Kaluga Ring Structure, *Russian Journal of Sciences on the Earth*, 1999, **1**(6), 503-510. [in Russian]
43. Gergelava, Sh.K., Buzinov, S.N., Shuleikin, V.N., and Voitov, G.I. Unconventional geophysics for underground gas storage facilities, *Oil, Gas and Business*, 2001, **5**(43), 2-7. [in Russian]
44. Baranov, V.I. *Radiometry*, Moscow, Izdatelstvo AN SSSR, 1956, 343p. [in Russian]
45. Shuleikin, V.N., Soil and atmosphere air radon and degassing of the Earth, *Georesources, Geoenergetics, Geopolicy*, 2010, **1**. El.No. FS77-36038.
46. Shuleikin V.N. Radon Transport to the Near Surface Soil and Air Layers, *Izvestiya, Atmospheric and Oceanic Physic*s, 2013, **49**(8), 853-859. [in Russian]
47. Sisigina, T.I. Measurements of radon exhalation from the rock surface, In Coll.: *Problems of Nuclear Meteorology*, Moscow, Gosatomizdat, 1962, 104-111. [in Russian]
48. Sisigina, T.I. Radon exhalation from the surface of soils of several types in the European part of the USSR and Kazakhstan, In Coll.: *Radioactive Isotopes in the Atmosphere and Their Use in Meteorology*, Moscow, Atomizdat, 1965, 40-48. [in Russian]
49. Metan, F.A. Alekseev, F.A., Voitov, G.I., Lebedev, V.S., and Nesmelova, Z.N. *Methane*, Moscow, Nedra, 1978, 310p. [in Russian]
50. Koshkin, N.I., and Shirkevich, M.G. *The Handbook on Elementary Physics*, Moscow, Nauka, 1976, 255p. [in Russian]

51. Shuleikin, V.N. Water vapors, atmospheric electricity and radon influx to the surface soil layers and the atmosphere, *Geophysical Processes and Biosphere*, 2014, **13**(3), 67–75. [in Russian]
52. Shuleikin, V.N. Atmospheric electric field sensitivity to changes in hydrogen and methane concentrations, *Georesources, Geoenergetics, Geopolicy: Electronic Sci. J.*, 2016, **1**(13), 19p.

CHAPTER 2

SPACE CHARGE OF THE SURFACE AIR: THE ELECTRODE EFFECT

The conductive characteristics of the first tens of meters of the surface atmosphere are generated by the ionizing radiation of radioactive elements present in the soil and the atmosphere: radon, thoron, and actinon. With the longest half-life, τ_{Rn} = 3.8 days (τ_{Tn} = 54.5 s; τ_{An} = 3.9 s), radon dominates the ionization process. During long-term observations of radon and thoron in soil and atmospheric air, only one profile was found (600 m, 13 pickets) above the rock crushing zone (according to drilling data), where the volumetric activities of radiogenic gases were comparable to each other Rn ~9.7 Bq/l; Rn(a) ~1.7 Bq/l; Tn ~7.5 Bq/l; Tn(a) ~0.9 Bq/l.

The results of numerous observational experiments have shown that the content of radon in soil air increases with the depth of sampling. On average, in loose homogeneous sedimentary rocks, the maximum volumetric activity of soil radon is reached at a depth of about 5 m. The increase in radon content with an increase in depth results from its discharge to the surface layers of the atmosphere. The observed pattern, with a relatively wide range of absolute values, has constant signs.

All measurements of the surface atmospheric electricity elements were performed at elevations of several decimeters to meters about the surface of the ground. These elevations fit with the active zone of the electrode effect. The initial solutions to the electrode effect problem considered only light ions to be present in the atmosphere and proved the existence of the classical and reverse electrode effects. This solution was obtained for a real atmospheric ratio of the concentrations of light and heavy ions, taking into account multiple charged aerosol particles and turbulent mixing.

2.1. Surface Air Ionizers

The problem of surface air ionization requires taking into account all radionuclides contained in the Earth. Their content in the soil determines the doses of radiation above-ground formed by natural radionuclides. The content, in turn, depends on the radioactivity of soil-forming rocks; processes of soil leaching by groundwater; the sorption of radionuclides by soils; and the deposition of radionuclides from soil water [1–5].

Three radioactive gases are: radon, Rn, with a half-life of τ_{Rn} = 3.82 days; thoron, Th, with a half-life of τ_{Tn} = 54.5 s; and actinon, Ac, with a half-life of τ_{Ac} = 3.92 s. These gases and their progeny are responsible for the surface atmospheric air ionization. The study in [6] presented analytical solutions for the problem of modelling radon distribution in the soil, two of which are of interest for the problem considered here. These scenarios include an endless homogeneous radioactive bed that outcrops and a non-radioactive layer covering a radioactive layer of infinite thickness.

The solution of the transfer equation for the simplest case of equality to zero of the convective transfer rate leads to the following expression:

$$\mathrm{Rn} = (Q/\lambda_{\mathrm{Rn}}) \times \{1 - \exp[-z(\lambda_{\mathrm{Rn}}/D)^{1/2}]\} \qquad (2.1.1)$$

where: Rn is the radon concentration in a unit volume of the pore space; Q is the emanation release rate to the pores per unit volume of rocks; $\lambda_{Rn} = 1/\tau_{Rn}$ is the emanation decay constant; z is the depth relative to the ground surface; and D_{Rn} is the diffusion coefficient.

Under the boundary conditions of the solution, it is assumed that the radon concentration at the ground level and, accordingly, in the atmosphere is zero. Such a limitation is fully justified. According to the statistical analyses of previous research [7–9], the ratio of the radon concentration at a depth of 2–3 m to the radon content in the atmosphere is not less than 100. The limiting ratio of the volumetric radon activity at a depth of 2 m to the atmospheric radon volumetric activity is 320 [10].

The distributions of the emanated gas for an outcropping infinite homogeneous reservoir—$Q1$, and for a non-radioactive layer 3 m thick, covering a radioactive layer of infinite thickness—$Q2$, are given in Figure 2.1.1.

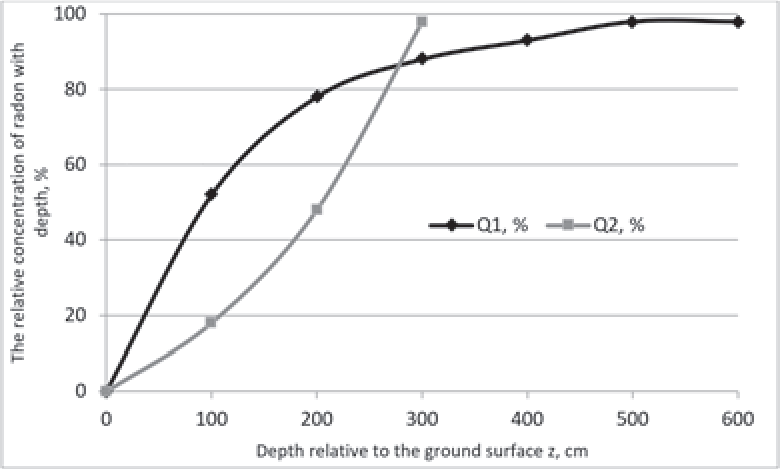

Figure 2.1.1: Concentration of radon with a depth relative to the ground surface, *z*, for the case of an infinite radioactive layer, *Q*1; and a non-radioactive layer with a thickness of $H = 3$ m, covering a radioactive layer of infinite thickness, *Q*2.

In the first approximation, the exponent in expression (2.1.1) can be written in the form of a series. Radon can be estimated as Rn $\sim Q \times z \times (\lambda_{Rn} \times D_{Rn})^{-1/2}$. The atomic weights of Rn, Th, and Ac are almost the same; the assumption of zero rates for their convective transport does not change the relative ratio of their concentrations.

As for radon, similar evaluative expressions can be obtained for concentrations of thoron, Th $\sim Q \times z \times (\lambda_{Th} \times D_{Th})^{-1/2}$, and actinon, Ac $\sim Q \times z \times (\lambda_{Ac} \times D_{Ac})^{-1/2}$. Assuming that the flowrates of their emanation into the pore space, $Q_{Rn} \sim Q_{Th} \sim Q_{Ac}$, are equal, the ratio of their concentrations is proportional to the ratio of the square roots of the ratios of their half-lives: Rn/Th = $(\tau_{Rn}/\tau_{Th})^{1/2}$ ~78; Th/Ac = $(\tau_{Th}/\tau_{Ac})^{1/2}$ ~3.7.

The control of radon and its variations in content in the surface layers of the soil and the surface atmosphere is of particular interest to urban geophysics, ecology, and medicine [6, 11]. The reason for this interest is the need to estimate and predict the content of radiogenic gas in urban areas. Underground structures, utilities, and heating lines can redistribute the pattern of its natural occurrence at a relatively low density, which does not represent a real health hazard. This can lead to the accumulation of radon in basements, and the local discharge of excess gas into the atmosphere. This problem can be solved through a better understanding of the radon transport mechanism in surface soil layers and the surface atmosphere.

Radon transport by rocks is carried out thanks to the mechanisms of diffuse and convective transfer. High speed is, of course, an inherent characteristic of convective transfer. According to experimental data, the maximum value of the ionizer transport rate in sandy-clay environments varies within a range of 40 to 60 cm/day [6, 12]. During a period of three half-lives, the concentration of radon will decrease by almost an order of magnitude.

Let us pass on to the analysis of data from the field measurements of radon distribution at depths of decimeters to meters relative to the ground's surface [10]. Here, in a period of 6.5 months from September 04 to March 19, 66 × 4 = 264 samples of soil air radon were taken at depths of 0.25 m, 0.75 m, 1.5 m, and 2.0 m. The atmospheric radon was not monitored.

The observation period stretched across autumn, winter, and spring. In winter, the freezing of the soil delays radon entry into the atmosphere, thereby contributing to its accumulation. This freezing took place from January 10 to March 01. During this period, the volumetric activity of radon at a depth of 0.25 m increased, on average, by a factor of 5.8; at a depth of 0.75 m it increased by a factor of 2.2; at a depth of 1.5 m it increased by a factor of 1.2; and at a depth of 2.0 m no change occurred.

Table 2.1.1. Average and maximum values of radon soil volumetric activity at 4 observation levels for the period September 04 to March 19 [10]

Depth, m	0.25	0.75	1.5	2
Rn (freezing), Bq/l	2.4	3.1	3.4	3.8
Rn (no-frost), Bq/l	0.4	1.4	2.7	3.8
Rn (max), Bq/l	3.1	3.3	3.5	**4.3**

The entire data array was divided into two parts: 16 groups of observations were obtained under conditions of soil freezing; the remaining 50 groups were obtained under no-frost conditions. The average values of volumetric radon activity at four levels under conditions of soil freezing and no-frost are shown in Table 2.1.1. The last line in Table 2.1.1 gives the maximum values of soil radon volumetric activity by working levels for the entire observation period.

For convenience of comparison with the calculated values, let us turn from the absolute average values of the volumetric radon activity in Table 2.1.1 to the relative values. The absolute values of volumetric radon activity were normalized to the maximum radon volumetric activity of the soil over the entire measurement period: Rn (2.0 m) = 4.3 Bq/l. Small relative average values of volumetric radon activity at a depth of 0.25 m under no-frost conditions were considered equal to zero. The relative variation in values obtained for radon from the ground surface to a depth of 2.0 m under freezing conditions, Rn(Freezing)/Rn(max) of the soil and no-frost Rn/Rn(max), are shown in Figure 2.1.2.

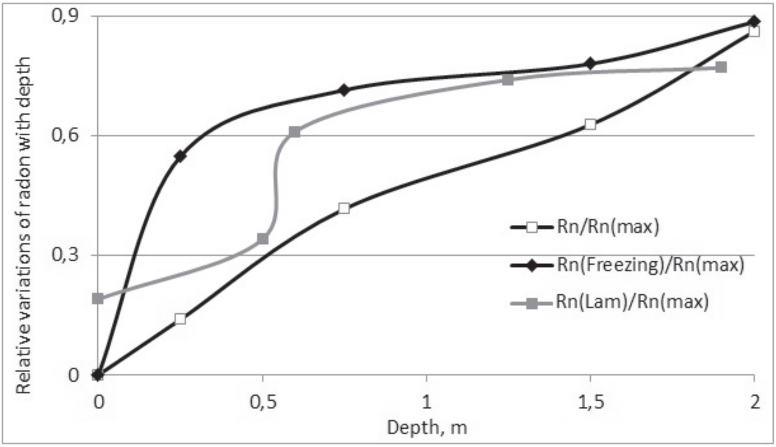

Figure 2.1.2: The relative level of soil radon content by depth under the conditions of: no-frost soil Rn/Rn(max); freezing soil Rn(Freezing)/Rn(max); high volumetric activity Rn(Lam)/Rn(max).

In the two examples considered, Rn(Freezing)/Rn(max) and Rn/Rn(max), the variations of the monitored parameter seen during the observations are close to the calculated values for the approximation of the first model for radon variations in an outcropping infinite homogeneous reservoir, as shown in Figure 2.1.1. Naturally recorded changes with deviations from the smooth asymptotic course of the calculated Q1 curve are shown in Figure

2.1.1. This is clearly explained by the heterogeneity of the real geological environment. Most likely, this is a consequence of the accidental introduction of clay inclusions, the radium content of which is Rn(clay) = 1.3×10^{-10} %; which is only 2 times less than in granites with Rn(granites) = 2.58×10^{-10} % [13].

It is interesting to consider the correlation coefficients between variations in the volumetric activity of radon sampled at different depths. In the absence of soil freezing, the correlation coefficient between radon in the samples from a depth of 0.25 m and 0.7 5m is $k_{(0.25;\ 0.75)} = 0.72$; at freezing this is $k_{(0.25;\ 0.75)} = 0.64$. The reason for the decline in the correlation is, most likely, that in no-frost conditions only the transfer process affects the radon content, while freezing causes the transfer and accumulation of radiogenic gas. The increase in radon content noted above supports this, especially at the levels of 0.25 m and 0.75 m.

The third significant correlation coefficient was obtained for variations in volumetric radon activity in the absence of soil freezing at the levels of 1.5 m and 2.0 m, with $k_{(1.25;\ 2.0)} = 0.79$. The results allow us to make some assumptions. The gas permeability values at depths of 0.25 m to 0.75 m and 1.5 m to 2.0 m are close to one another, although one would expect that there would be lower gas permeability at greater depths. A smaller correlation coefficient of radon variations at shallower depths is a consequence of additional processes affecting the radon content. This is due to the ingress and evaporation of moisture from the atmosphere into the near-surface pores of the soil and “wind suction” [12] of radon into the atmosphere.

In the example of radon distribution considered, with a depth relative to the ground surface, the recorded average values of the monitored parameter are relatively small (Table 2.1.1). An additional experiment was performed under conditions of abnormally high radon volumetric activity. The average level of volumetric activity of radon in the atmosphere over a three-day observation period was Rn(a) = 7.6 Bq/l [14, 15].

For the entire period of observation, 65 samples taken in the atmosphere and at depths of 0.5 m, 0.6 m, 1.25 m, and 1.9 m were analyzed. Measurements were made on the left bank of the Polosnya River near the village of Lamonovo, Moscow Region. The site at which the sampling was performed, was located at a height of ~2 m relative to the water’s edge, i.e., roughly at a distance of ~3m from a thick argillaceous confining bed. Otherwise speaking, the soil observation conditions were close to the $Q2$ model approximation (Figure 2.1.1). The average and maximum values of volumetric radon activity at the listed elevations are shown in Table 2.1.2.

Table 2.1.2. Average and maximum values of soil radon volumetric activity at five observation levels (Lamonovo village, Moscow Region)

Depth, m	0 [Rn(a)]	0.5	0.6	1.25	1.9
Rn, Bq/l	7.6	13.7	24.5	29.7	31.0
Rn(max), Bq/l	9.3	20.5	31.4	36.3	**40.2**

The transition from absolute to relative values was normalized to a maximum value of volumetric radon activity recorded at a depth of 1.9 m: Rn(max) = 40.2 Bq/l, shown in the last cell in Table 2.1.2. The average value of atmospheric radon volumetric activity was assumed to be equal to the volumetric activity of radon at the ground level and was also normalized using Rn(max). The relative variations of soil radon within a depth range of 0 to 1.9 m are shown in Figure 2.1.2: Rn(Lam)/Rn(max).

The Rn(Lam)/Rn(max) curve shows a noticeably higher variation, rather than Rn(Freezing)/Rn(max) and Rn/Rn(max), but it is more suitable for calculating the estimates of the first model approximation. The reason for significant deviation from the smooth curve of *Q*1, as in Figure 2.1.1, is the abnormally high value for radon activity in the selected area. Randomly scattered clay inclusions present in the depth range investigated contain abnormally high amounts of the parent substance.

At the final stage of analysis into the relationships between radon, hydrogen, and methane in the soil and atmospheric air, we illustrate the relationships of the listed gas parameters based on field observations. In August 2006, at the site of the North Stavropol Gas Storage Facility, in an area of 20 km by 30 km, volumetric activities of soil and atmospheric radon were recorded at 300 pickets. Repeated measurements with simultaneous sampling of soil air for laboratory analysis of methane and hydrogen content were performed at 28 pickets with minimal and maximal ratios of the soil and atmospheric radon.

Weather conditions were adverse for the taking of measurements. The drought in August 2006 led to a large amount of cracking of the ground, as shown in Figure 1.2.6. The presence of deep cracks of up to 50–60 cm, dramatically increased the area for soil-atmosphere air exchange, i.e., it reduced the density of exhaled soil radon: the average value of Rn(*a*) = 0.49 Bq/l; soil radon samples were taken from soil pockets with an area of ~0.5 m^2 limited by cracks and the average value of Rn = 1.04 Bq/l.

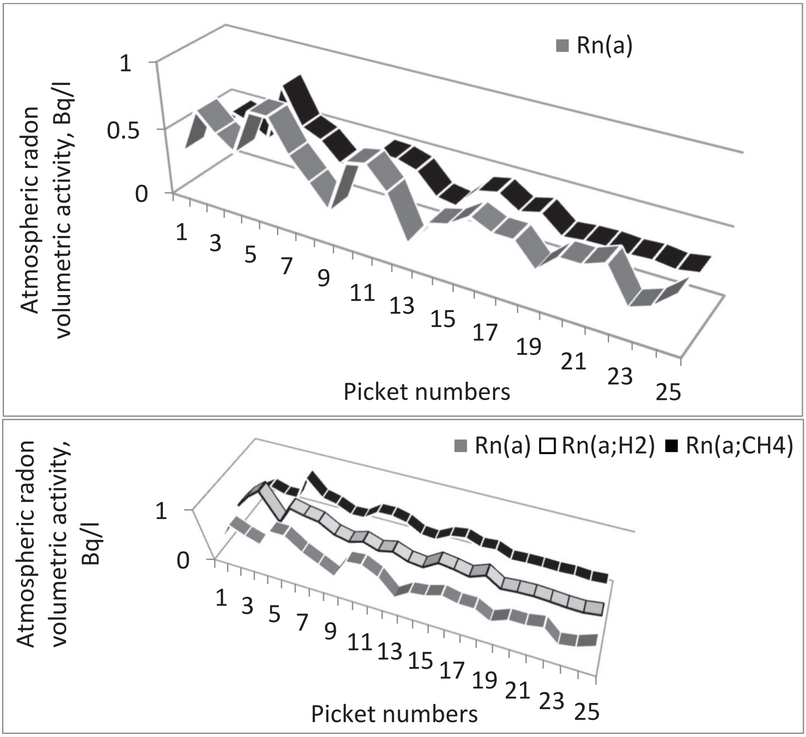

Figure 2.1.3: Measured, Rn(*a*), and calculated values of atmospheric radon volumetric activity for 3 cases of transfer: 15 % of radon transferred by methane; 85 % by hydrogen, Rn(*a*; 0.15 CH_4; 0.85 H_2); 100 % of radon transferred by hydrogen, Rn(*a*, H_2); 100 % of radon transferred by methane, Rn(*a*, CH_4).

The observations were repeated in June 2007 under normal weather conditions at 500 observation pickets with parallel sampling at 24 pickets. The recorded mean values of soil and atmospheric radon were: Rn(*a*) = 0.46 Bq/l; Rn = 1.07 Bq/l. According to the laboratory analysis of 52 samples of the soil air, recorded concentrations of soil methane varied within the range (10^{-6}–10^{-5}) vol.%.

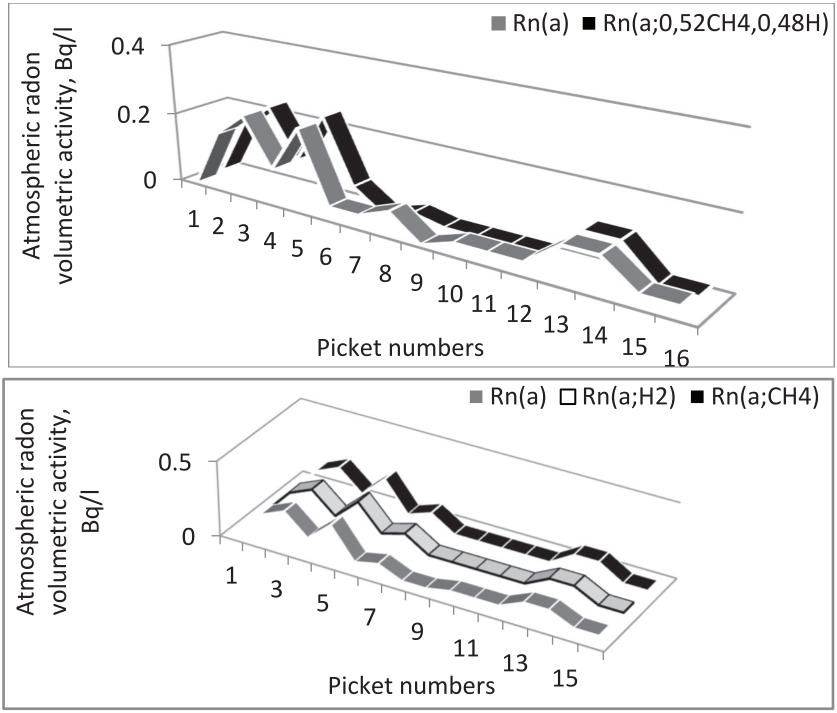

Figure 2.1.4: Measured, Rn(*a*), and calculated values of the atmospheric radon volumetric activity for 3 cases of its transfer: 52 % of radon is transported by methane; 48 % by hydrogen, Rn(*a*; 0.52 CH_4; 0.48 H_2), the upper graph; 100 % of radon is transported by methane, Rn(*a*; CH_4); 100 % of radon is transported by hydrogen, Rn(*a*; H_2)

The results from 2006 and 2007 were combined and the degree of participation of each of the two volatile gases in radon transport was estimated: 15 % of radon was transported by methane bubbles and 85 % by hydrogen bubbles. A working formula combining the soil and atmospheric radon and two volatile gases was calculated for the introduced ratio of hydrogen and methane in radon transfer. An additional experiment performed at 28 observation pickets allowed us to evaluate the work of the modelled approximation considered.

Figure 2.1.3 shows the measured and calculated values of the atmospheric radon volumetric activity for three cases: 15 % of radon transferred by methane and 85 % by hydrogen; 100 % of radon transferred by methane; 100 % of radon transferred by hydrogen.

The correlation coefficients of the measured and calculated values of atmospheric radon are: k[Rn(a), Rn(a; 0.15 CH_4; 0.85 H_2)] = 0.84; k[Rn(a); Rn(a; CH_4)] = 0.69, k[Rn(a); Rn(a; H_2)] = 0.81. The scatter of the correlation coefficients obtained was rather insignificant and all the correlation coefficients obtained were significant.

The results obtained can be clearly explained in scientific terms. Hydrogen and methane concentration pairs used in the assessment are present in the calculations of the relationship between the volatile gases (Figure 1.2.8). This means that the correlation coefficients obtained, by definition, must be close to one another. The scatter of the correlation coefficients was determined by the measurement errors of soil and atmospheric radon volumetric activity (see Section 1.1), and errors of laboratory determination of volatile gas concentrations at a level of 10^{-6} vol.%, which is the detection limit of the laboratory equipment (Figure 1.2.8).

In September 2009, the experiment was repeated, but at high concentrations of soil methane (10^{-3}–10^{-2}) vol.%. The research was performed at the site of a cluster of 19 injection wells and one observation well in a 500 m × 500 m area of the Kasimov Gas Storage Facility (Figure 1.3.4). In the course of measuring the soil and atmospheric radon, 160 pickets were surveyed at the site of the injection wells and 16 pickets at a location remote from the main observation area, about 2 km distant. On the last day of the fieldwork, after the withdrawal of injected gas from the territory of 19 injection wells, 22 pickets were selected to set the maximum and minimum soil and atmospheric radon ratios. At these pickets, repeated measurement of soil radon, with parallel sampling of soil air for laboratory analysis of methane and hydrogen, were performed. Following the review of volatile gas concentrations, 16 pairs of values were used in calculating the exponential relationship between methane and hydrogen: samples 53–58 (Figure 1.2.8).

As expected, the correlation coefficients of the measured and calculated values of atmospheric radon were: k[Rn(a); Rn(a; 0.52 CH_4; 0.4 8H_2)] = 0.92; k[Rn(a); Rn(a; CH_4)] = 0.89; k[Rn(a); Rn(a; H_2)] = 0.90. These were very high and comparable to one another. There may be several reasons for these results. The calculations were performed for high concentrations of volatile gases, with laboratory errors that were less than for concentrations of 10^{-6} vol.%. As detailed in Figure 1.2.8, it is to be noted that in analyzing many samples, laboratory equipment was working at its resolution limit. Soil air samples for the rapid determination of volumetric radon activity and laboratory analysis for hydrogen and methane contents were used in a single sampling cycle.

Radon distributed in the soil, at a depth of up to two meters, and entering the surface atmosphere, is due to the decomposition of a parent substance, which is randomly scattered in the geological environment. The closest description is given by the model of an outcropping infinite homogeneous reservoir Q1 (Figure 2.1.1). Thoron and actinon barely participate in the ionization of surface air (Figure 1.1.5).

Analysis of the results from experimental observation allows us to state that radon transfer to the surface soil layers and the surface atmosphere is performed by bubbles of two volatile gases—hydrogen and methane. In particular, the inspection carried out at the site of the North Stavropol GSF in the range of soil methane concentrations (10^{-6}–10^{-5}) vol.% showed that the correlation coefficient of the measured and calculated volumetric levels of atmospheric radon is $k[\mathrm{Rn}(a), \mathrm{Rn}(a;\ 0,15\ \mathrm{CH_4};\ 0.85\ \mathrm{H_2})] = 0.84$. The test performed at the site of the Kasimov Gas Storage Facility in the range of methane concentrations of (10^{-3}–10^{-2}) vol.% resulted in a correlation coefficient of measured and calculated values of the atmospheric radon volumetric activity $k[\mathrm{Rn}(a), \mathrm{Rn}(a;\ 0.52\ \mathrm{CH_4};\ 0.48\ \mathrm{H_2})] = 0.92$.

2.2. Radon Transfer to the Surface Soil Layers and the Atmosphere

As described in previous sections, only hydrogen and methane act as radon gas carriers in the surface soil layers and the atmosphere [16–18]. The results obtained can be clearly explained in scientific terms. In the course of experiments from onboard an aircraft, traces of radon were recorded at altitudes of several kilometers [19]. As such, it can be assumed that bubbles of carrier gases in the soil “float” up into the atmospheric air. For this purpose, however, their weight needs to be less than that of atmospheric air. This is true for hydrogen and methane and untrue for nitrogen and carbon dioxide.

Following the logic of the physical explanation presented, the pool of carrier gases for radon in the surface soil layers and the surface atmosphere should include all gases that have a lighter weight than atmospheric air, in particular, helium and water vapor. However, helium, like radon, is an inert gas. It is thus excluded from the list of carriers. A bubble of one inert gas is unable to capture a molecule of another inert gas.

Understanding the participation of water vapor in radon transfer to surface soil layers and the surface atmosphere requires more detailed discussion. Heavy ions, which are primarily responsible for AEF development, form as a result of light ions combining with neutral condensation nuclei. The presence of water vapor in the atmospheric air partially determines the presence of neutral condensation nuclei, with which light ions are recombined. The main source of water vapor is the ocean’s surface. Under continental conditions, evaporation from inland water bodies (lakes, rivers, etc.), the soil surface, and vegetation cover is permanent [20, 21]. Let us illustrate this relationship with elements of surface atmospheric electricity at a qualitative level.

During the period August 09–27, 1990, continuous recording of AEF was carried out with two field mills installed on-land, 100 m from the coastline, and on a pontoon 300 m off the coast at the Ozerninskaya Base of VNIIFTRI. When considering the difference in the averaged daily variation of the field recorded above water and on-land, a steady maximum of about 70 V/m was indicated between 7 a.m. and 9 a.m. At this time, a weak haze appeared almost daily over the water, which was produced by evaporation from the water’s surface. To put it differently, the injection of neutral condensation nuclei took place, leading to an increase in AEF above the water.

To quantify similar effects, let us use the results of observations presented in [10]. Two days of observation data on AEF, relative air humidity, and condensation nuclei density at the Zugspitze Mountain (the Northern Alps) are given. The results obtained are also of interest because during the observation period the condensation nuclei density passed an extensive range of values—from a few hundreds to 4,500 cm^{-3}; whereas for medium plain conditions the typical density equaled a few thousand nuclei per cubic centimeter.

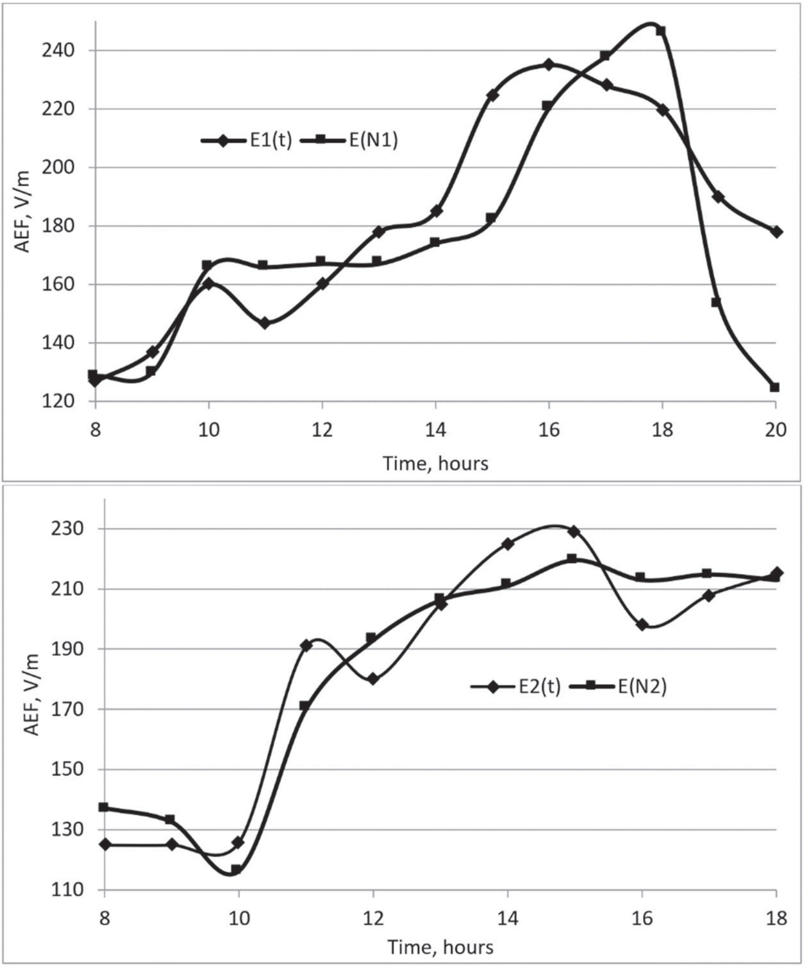

Figure 2.2.1: Measured $E_1(t)$, $E_2(t)$ values of AEF. The calculated $E(N_1)$, $E(N_2)$ AEF values developed as functions of the density of neutral condensation nuclei, N_1 and N_2 [10].

For the first and second day of observation, a pair of AEF values and the density of condensation nuclei were approximated by a logarithmic function, the values of which took the following form: $E_1(\mathrm{t}) = 42.2\mathrm{Log}(N) - 107.9$ and $E_2(t) = 38.6\mathrm{Log}(N) - 94.3$. The expressions are dimensionless: E is normalized to 1 V/m; N is normalized to 1 cm^{-3}. In the expressions presented, N is the density of condensation nuclei, which changed on the first day within the range (250–4,500) cm^{-3}; and on the second day within the range (330–4,100) cm^{-3}. Figure 2.2.1 shows the results of the AEF values measured and the calculated values of the field for the approximations $E(N_1)$ and $E(N_2)$.

The correlation coefficients between the measured and calculated field values for the first and second days are equal to $k_1[E_1(t); E(N_1)] = 0.80$; $k_2[E_2(t); E(N_2)] = 0.95$. Additional estimates showed that the relationships between the measured field values, the relative humidity, q, and the density of condensation nuclei, N, were also very large. The corresponding correlation coefficients for the first day of observation were equal to: $k_1[E_1(t); q1] = 0.90$, $k_1[E_1(t); N_1] = 0.72$. For the second day of observation, they were: $k_2[E_2(t); q2] = 0.98$, $k_2[E_2(t); N_2] = 0.93$.

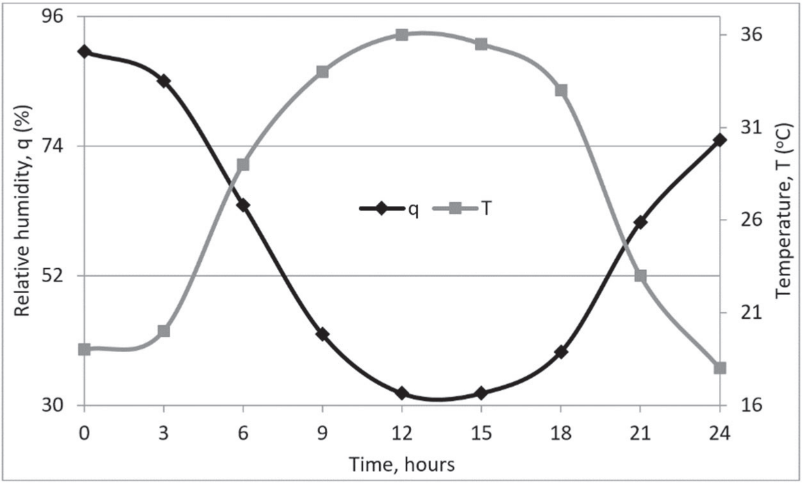

Figure 2.2.2: Daily variation of temperature and relative humidity on a hot summer's day in Central Russia.

The quantitative results obtained confirm the statement formulated above on the relationships of AEF to the density of neutral condensation nuclei. This indicates that there is a relationship between the field and the relative humidity of the air. In turn, this is an indicator of processes of evaporation in the atmosphere [21].

Moreover, on land, the relative humidity varies in antiphase with air temperature. Figure 2.2.2 presents the results of changes in temperature and relative humidity in the central region of Russia on a hot summer's day.

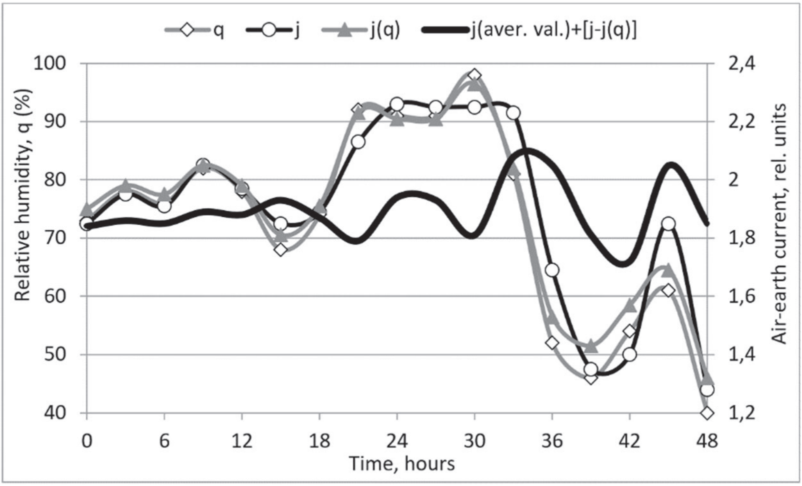

Figure 2.2.3: Two-day recording of the variation of measured, *j*, and calculated, *j*(*q*), values of the air-earth current and relative air humidity, *q*, in Molla-Kara village (Turkmenistan). The minimized two-day variations of the air-earth current with allowance for changes in relative humidity, *j*(aver. val.) + [*j*-*j*(*q*)].

Let us consider an example of the causal correlation between the elements of surface atmospheric electricity and the evaporation process—the relative humidity. Figure 2.2.3 shows two days of records of the air-earth current, *j*, recorded by a differential passive antenna [22] near Molla-Kara village in autumn 1983 and data on relative humidity, *q*, taken at the nearest meteorological station, located about 30 km away. The three-hour time interval between the points in Figure 2.2.3 was determined by the discreteness of the monitoring observations at the meteorological station. The correlation coefficient between the parameters considered is very high, *k*(*j*;*q*) = 0.96. For the selected two-day observation period at a distance up to 100 km from Molla-Kara village, no noticeable changes in seismicity were recorded, which could lead to variations in the air-earth current.

In Figure 2.2.3, the air-earth current, *j*, and scatter due to variations in the relative humidity, *q*, is about 50 %. If we take the difference characteristic [*j* - *j*(*q*)], then this scatter will decrease noticeably, *j*(ave.val.) + [*j* - *j*(*q*)]. This result is useful in solving predictive tasks on changes associated with precursors to an earthquake are highlighted with the background of daily variations in the controlled parameter.

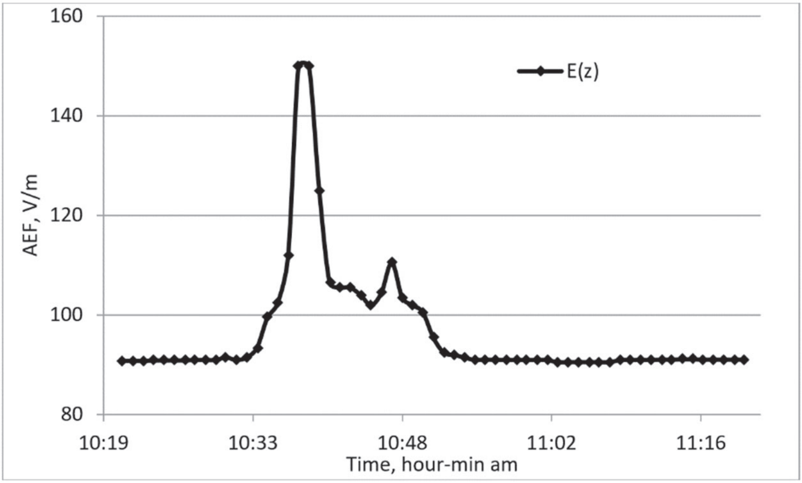

Figure 2.2.4: Field splash according to the readings of a field mill at a stationary point on June 09, 2005. The average background level was 90 V/m; the maximum surge amplitude was 150 V/m.

Let us consider another example of abrupt changes in AEF stimulated by evaporation. Figure 2.2.4 shows records of field variation registered in the Kuban River valley, near the Ust-Nevinsky farmstead in the Stavropol Territory. In the time interval of 10^h21^m–11^h20^m a.m. 06/09/2005, you can see a powerful twenty-minute signal spike, *E*(*z*) [23, 24]. The field decrease with a yield to the background level of 90 V/m, 10^h55^m a.m., visually coincided with the complete drying out of dew on the grass around the measuring device. The beginning of the growth of the field mill signal, 10^h30^m a.m., was not accompanied by any noticeable external changes. Nevertheless, it can be quite confidently assumed that it corresponded to the onset of dew evaporation due to solar warming.

Let us continue the analysis of the experimental material with examples that are not amenable clear physical explanation. Figure 2.2.5 shows the results of observation of the air-earth current, AEC, *j*(18.10)–*j*(21.10) for the period of October 18–21, 2010 [23, 24].

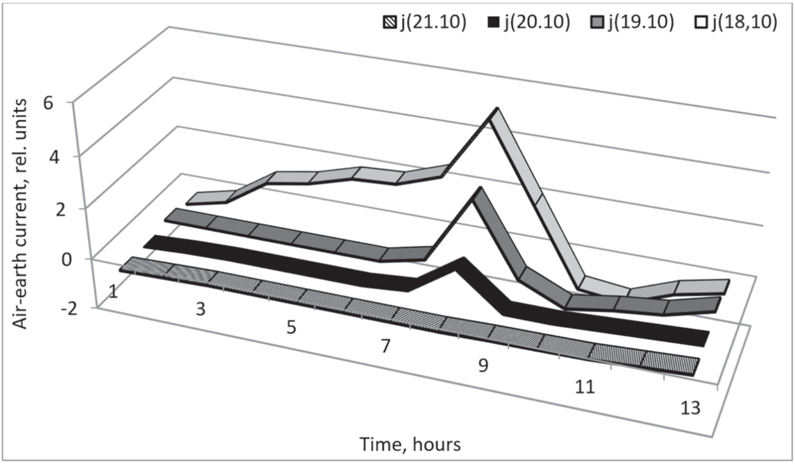

Figure 2.2.5: Variations of the air-earth current, AEC, of the surface atmosphere for the time interval of 2 a.m.–12 p.m. of October 18–21, 1983. Observation results taken in Zakataly, Azerbaijan.

The measurements were made in the foothills of the North Caucasus in autumn on the banks of an almost dried up riverbed and in the suburb of Zakataly, Azerbaijan. In the period of October 15–18, 1983, the weather was cold and it rained heavily. By the night of October 18, the rain had stopped, and a rapid warming began.

With the onset of warming on October 18, at about 3 a.m., there was a slow increase in the air-earth current. Taking into account the results obtained, this growth was associated with the evaporation process, with the injection of neutral condensation nuclei into the atmosphere, i.e., as AEF increased. Over the period 8^h00^m a.m. to 8^h30^m a.m., the amplitude of the signal almost doubled. The reason for this doubling was the release of the ionizer into the atmosphere from the pores that opened during the evaporation process. At the same time, the polar conductivities of the atmospheric air increased and the rate of recombination of light ions with neutral condensation nuclei increased as well, i.e., there was an increase in AEF. As a result, a sharp increase in the air-earth current level took place. The subsequent decrease in the signal as due to the drying out of moisture on the ground surface and grass cover with the termination of the injection of neutral condensation nuclei and minimization of soil radon delivery to the atmosphere accumulated in the surface soil layers during the rainy season.

Over October 19 and 20, a sharp increase followed by a decrease in the air-earth current level of only an hour's duration was seen. It ended with the moisture drying under the collecting elements of the differential antenna. Its amplitude naturally decreased, and it disappeared entirely on October 21 with the final depletion of radon reserves in the surface soil layers accumulated during the rainy period.

As to whether water vapor is involved in radon transport to the surface layers of the atmosphere or not remains an open question. To answer this question, let us consider the mechanism of ionizer transfer in layers of sedimentary rock. The probability of a bubble capturing a radon molecule is proportional to the concentration of radiogenic gas in the soil: it will be maximal at a depth of 3–6 meters (curves Q_1 and Q_2, Figure 2.2.1) and minimal at the level of the Earth's surface. After the capture of a radon molecule by a bubble, the probability of its transfer to the atmosphere is inversely proportional to the decrease in the concentration of the radiogenic gas as it approaches the surface. This means that the probability of an ionizer entering the atmosphere from a layer of rock thickness Δz is proportional to the thickness of the layer Δz, regardless of whether this layer is located at the ground surface or a depth of 3–6 meters.

At the beginning of solar heating, evaporation occurs directly at the ground surface; then, as it is heated, it engages the surface pore space. For the models in Figure 2.2.1, even if evaporation proceeds from a depth of 6 cm, as in curve Q1, or 3 cm, as in curve Q2, an increase in the concentration of exhaling radon due to its transfer by water vapor will be 1 % of the current background radon concentration in the atmosphere, which has little effect on changes in elements of surface atmospheric electricity. During the observation period, 18–20 October 1983, the controlled air-earth current increased many times above the background level. This result can be explained solely by an increase in the density of neutral condensation nuclei and additional ionization due to the exhaling soil radon accumulated during the rainy period. At the same time, the direct contribution of water vapor to the transfer of radon to the atmosphere is virtually imperceptible.

Analysis of the field material confirms the modelled representation of the mechanism of relationships between volatile gases, soil radon, and elements of surface atmospheric electricity.

Multiple experiments have proved that radon is transferred by hydrogen and methane through the soil and into the atmosphere. Helium, like radon, belongs to the category of inert gases and, therefore, cannot act as a carrier of an ionizer. The capture of radon by water vapor is only possible where evaporation takes place—from the vegetation cover, the soil surface, and the subsurface pore space. Moreover, even if it were the case that water vapor could capture the ionizer at a depth of 3–6 cm, its additional exhalation would only be about 1 % of the background level of the ionizer content in the surface atmosphere.

The injection of water vapor to the surface air does increase the density of neutral condensation nuclei, i.e., it will inevitably lead to an increase in AEF. On the other hand, it opens up the subsurface pore space, which has been tamped down with moisture. This all promotes the discharge of accumulated radon into the atmosphere and increases the polar conductivity of the surface air. The small thickness of the soil layer in which the process of evaporation takes place makes an extremely insignificant contribution to the transport of radon to the atmosphere and changes in the local background level of the exhaling ionizer.

2.3. The Electrode Effect in the Atmospheric Surface Layer

The bulk of observation results of surface atmospheric electricity elements were obtained under conditions of "fair weather" when installing measuring devices at the height of some decimeters relative to the ground surface. The concept of "fair weather" includes the absence of thunderstorms, precipitation, frost, fog, dust, low cloud cover, and wind speeds up to 6 m/s. Moreover, at the observation point, there were no powerful sources of ionization and the concentration of neutral condensation nuclei (aerosol) was low [25–27]. All this suggests that under such conditions the electrical characteristics weakly depend on local factors.

The results of theoretical and experimental studies suggest that even under "fair weather" conditions, the space charge of the surface atmosphere depends on the level of air ionization, the density of aerosol particles, and turbulent mixing [28–31]. The process of air ionization has both natural and artificial causes [32]. As such, the level of ionization and aerosol air pollution may be associated with anthropogenic effects on the atmosphere.

The electrical structure of the surface layer is determined by the "electrode effect," which sees a redistribution of the space charge on the negatively charged ground surface [32]. The thickness of the electrode layer in the atmosphere varies from a few decimeters to tens of meters [33, 34].

The problem of the electrode effect can be formulated as the task of finding the distribution of positive and negative light and heavy ion concentrations; the electric field intensity; and the space charge in the surface layer. Depending on the meteorological situation in the atmosphere, three extreme cases were considered: the classical electrode effect; the reverse electrode effect; and the turbulent electrode effect.

The first two cases occur in the absence of turbulent mixing in the atmosphere—it is assumed that the space-time distribution of the space charge in the surface layer is solely due to electric forces.

In the third case, the transport of light and heavy ions in the atmosphere occurs along with electrical forces caused by turbulent air flows, and turbulence may play a major role.

Since the mid-twentieth century, the theory of the electrode effect has developed [35–39]. The problem was solved for the model of the presence of light ions in the atmosphere, as presented in Figure 2.3.1. This showed a difference in AEF variations in the reverse and classical electrode effects. At a low ionization rate, $q(z)$—a low concentration of exhaling soil radon—a smooth decrease in the field is followed by a return to the background level, giving the classical electrode effect. With a high concentration of ionizer, the decline goes to a level below the background. Furthermore, a bend in the curve and yield to the background level occurs in AEF changes. The decline of the AEF below the background level is due to the formation of a layer of negative space charge above the negatively charged ground surface.

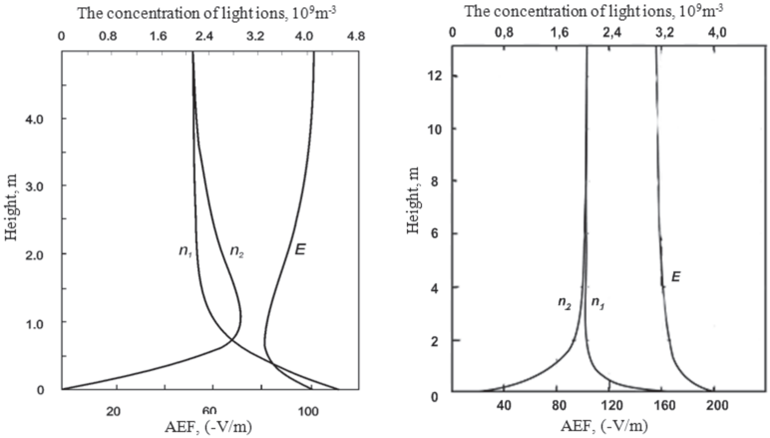

Figure 2.3.1: Reversible and classical electrode effect with ionization rates $q(z) = 7 \times 10^6 + 80 \times 10^6 \exp(-2.362z)$ ion pairs m^{-3} s^{-1} and $q(z) = [7 \times 10^6 + 4.8 \times 10^6 \exp(-2.362z) + 50\mathrm{tg}(8 \times 10^{-8} \times z)]$ ion pairs m^{-3} s^{-1}.

Under actual atmospheric conditions, the concentration of heavy ions is an order of magnitude higher than that of light ions. However, until recently, the solution of the problem had been obtained, using the Runge-Kutta method, only for comparable concentrations of light and heavy ions [40, 41]. Table 2.3.1 shows calculations of the concentrations of positive and negative light ions, n_1 and n_2; and heavy ions, N_1 and N_2, in relation to their concentrations at the background level, n and N, E in the fields E_0 (-100) V/m and (-500) V/m taking into account the presence of heavy ions in the atmosphere in the concentration range of 10^8–10^9 m^{-3}.

A mathematical model of electrodynamic processes in the surface layer of the atmosphere, under conditions of aerosol pollution, has been developed [42–44]. The system of equations describes a non-stationary electrodynamic model of a horizontally homogeneous convective-turbulent atmospheric surface layer with multiply charged aerosol particles. The solution of this system of equations has allowed us to develop an idea of the space charge distribution of the atmosphere with heights for various concentrations of light and heavy ions (Figure 2.3.2) [42].

Table 2.3.1. Electrical characteristics of the atmosphere at the ground surface for various E_o in the presence of heavy ions

E_o, V/m	$N = 10^8$ m^{-3}		$N = 5 \cdot 10^8$ m^{-3}		$N = 10^9$ m^{-3}	
	-100	-500	-100	-500	-100	-500
1	2	3	4	5	6	7
$N_1 \times 10^9$, z = 0m	2.01	1.89	1.84	1.72	1.65	1.52
$N \times 10^9$	1.94	2.03	1.85	1.85	1.63	1.52
$n_1/n, z$ = 1m	1.01	0.92	0.97	0.92	0.98	0.98
$n_2/n, z$ = 1m	0.44	0.07	0.45	0.08	0.49	0.10
$E/E, z$ = 1m	1.39	2.01	1.41	2.0	1.37	1.83
$N_1/N, z$ = 1m	1.90	3.80	1.94	3.88	1.80	3.76
1	2	3	4	5	6	7
$N_2/N, z$ = 1m	0.38	0.02	0.39	0.03	0.44	0.04
$n_1/n, z$ = 2m	1.03	0.93	0.98	0.93	0.99	1.00
$n_2/n, z$ = 2m	0.78	0.14	0.77	0.16	0.80	0.18
E_0/E	1.11	1.87	1.14	1.85	1.12	1.69
N_1/N	1.43	3.33	1.26	2.90	1.21	4.10
$N_2/N, z$ = 2m	0.95	0.01	0.78	0.09	0.83	0.10
E_0/E	1.94	2.16	2.01	2.16	1.98	2.0

The plots in Figure 2.3.2 clearly illustrate: the existence of the classical and reverse electrode effects; an increase in the contrast and height of its manifestation with the growing concentration of light and heavy ions; and the dominant influence of the concentration of heavy ions on the intensity of the manifestation of the reverse electrode effect.

The results of calculations given in Figure 2.3.2 show that ion formation depends on aerosol concentration. Concentrations of about (10^8–10^9) m^{-3} inherent to a “clean” atmosphere, cause the classical electrode effect, shown in curves 1–3; concentrations of 5×10^9 m^{-3} or higher, which can be observed in urban agglomerations and industrial zones, cause the reverse electrode effect, as shown in curves 4–7.

The growth of the AEP module with the degree of turbidity in the atmosphere (curves 4–7), and a decrease in transparency or the meteorological visibility range, is well known [45]. Experimental confirmation of this can be seen in Figure 2.2.1.

Turning back to Section 1.1, one should recall that, until now, there have only been a few examples in the scientific literature that record anomalous variations of AEF before earthquakes. As a consequence, at the end of the last century, to simulate possible processes in the Earth’s crust in the run-up to a seismic event, researchers used extensive material obtained in the laboratory in experiments with rock samples. These are well-known dynamoelectric effects and phenomena: the Stepanov effect; the piezoelectric effect; electrokinetic phenomena; electrification during friction and destruction of rocks; and deformation of electrical double layers etc. [46–53].

Unfortunately, these effects cannot explain the long-lasting quasi-stable bipolar deviations of the AEF from background values of several hundred percent. If we refer to the results of calculations shown in Figures 2.3.1 and 2.3.2, the recorded bipolar field anomalies are determined by the classical and reverse electrode effects. At low ionization rates there is a low level of soil radon exhalation and the fields are positive. At high ionization rates there is a high radon content in the surface atmosphere and the formation of a negative space charge layer above the negatively charged ground surface, leading to a change in the AEF sign.

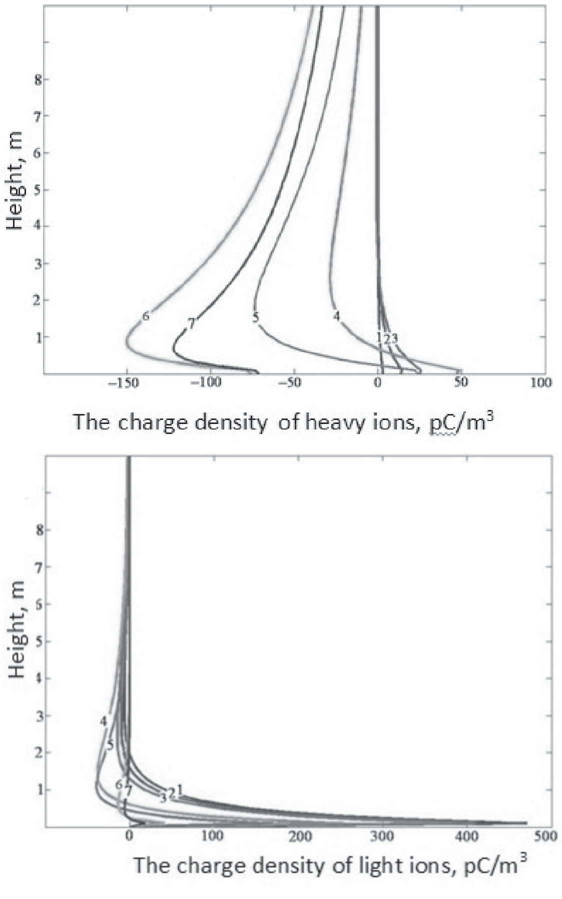

Figure 2.3.2: The space charge density formed by light and heavy ions. Curve 1 – N_1 ~10^8 m^3; curve 2 – N_2 ~5 × 10^8 m^3; curve 3 – N_3 ~10^9 m^3; curve 4 – N_4 ~5 × 10^9 m^3; curve 5 – N_5 ~10^{10} m^3; curve 6 – N_6 ~5 × 10^{10} m^3; curve 7 – N_7 ~10^{11} m^3.

2.4. References to Chapter 2

1. Voitov, G.I. Chemistry and scope of the new natural gas flow in various geostructural zones of the Earth, *Zhurnal Vses. Khim. Obsch. im. D. I. Mendeleeva*, 1986, **XXXI**(5), 533-540. [in Russian]
2. Voitov, G.I., Gusev, A.S., Shuleikin, V.N. *et al.* Emanation (hydrogen-radon) and electric effects above complex tectonic structures (on the example of Alexandrovskaya zone of pre-fault elevations, Belarus), *DAN RAN*, 2000, **370**(1), 105-108. [in Russian]
3. Klimshin, A.V. Estimation of radon flux density variations in the occurrence of free heat convection in the upper soil layer, *Uralsky Geofizichecky Vestnik*, 2009, **2**. [in Russian]
4. Klimshin, A.V., Kozlova, I.A., Rybakov, E.N., and Lukovsky, M.Yu. Influence of freezing of the surface soil layer on the radon transfer, *Vestnik KRAUNTS Nauki o Zemle*, 2010, **2**(16), 231-237. [in Russian]
5. Kozlova, I.A. The effect of meteorological factors on Rn-222 behavior in the rock mass, *Geophysics-2007: Proc. Sci-Pract. Conf.*, St.-Petersburg, 2007, 190-191. [in Russian]
6. Baranov, V.I. *Radiometry*, Moscow, Izdatelstvo AN SSSR, 1956, 343p. [in Russian]
7. Sisigina, T.I. Measurements of radon exhalation from the rock surface, In Coll.: *Problems of Nuclear Meteorology*, Moscow, Gosatomizdat, 1962, 104-111. [in Russian]
8. Sisigina, T.I. Radon exhalation from the surface of soils of several types in the European part of the USSR and Kazakhstan, In Coll.: *Radioactive Isotopes in the Atmosphere and Their Use in Meteorology*, Moscow, Atomizdat, 1965, 40-48. [in Russian]
9. Shuleikin, V.N. Soil and atmosphere air radon and degassing of the Earth, *Georesources, Geoenergetics, Geopolicy*, 2010, **1**(1), 13p. [in Russian]
10. Styro B.I. *Problems of Nuclear Meteorology*, Vilnius, 1959, 418p. [in Russian]
11. Dyachuk, V.A., Martynov, A.A., Sterkhov, P.L., and Shvarts, Ya.M. About changes in the electrical state of the atmospheric boundary layer after the accidental emission from the Chernobyl NPP, *Proc. IV All-Union Symp. on Atmospheric Electricity*, 1990, Nalchik, 26. [in Russian]
12. Styro, B.I. *Atmosphere Self-Purification from Nuclear Pollution*, Leningrad: Gidrometizdat, 1968, 290p. [in Russian]

13. Koshkin, N.I., and Shirkevich, M.G. *Handbook on Elementary Physics*, Moscow, Nauka, 1976, 255p. [in Russian]
14. Shuleikin, V.N. Radon transfer to the subsurface soil layers and the surface atmosphere, *Geophysical Processes and Biosphere*, 2013, **12**(2), 57-66. [in Russian]
15. Shuleikin, V.N., Reznichenko, A.P., and Puschina, L.V. About relationships of soil air methane, hydrogen, and radon, *Proc. All-Russ. Conf. "Degasification of the Earth: Geodynamics, Geofluids, Oil, Gas, and Their Parageneses,"* Moscow, 2008, 544-546. [in Russian]
16. Zubarev, A.P., and Shuleikin, V.N. *Complex Geophysical and Geochemical Monitoring for Underground Gas Storage Facility Operation*, Moscow, Izd. Gasprom GSF OOO, 2009, 264p.
17. Shuleikin, V.N. Water vapors, atmospheric electricity and radon influx to the surface soil layers and the atmosphere, *Geophysical Processes and Biosphere*, 2014, **13**(3), 67-75.
18. Shuleikin, V.N. Radon transport to the near-surface soil and air layers, *Izvestiya, Atmospheric, and Oceanic Physics*, 2013, **49**(8), 853-859.
19. Voitov, G.I., Starobinets, I.S., and Usmanov, R.I. About density of CH_4 flows to the atmosphere in oil and gas bearing regions (on the example of Amu-Darya Basin), *DAN SSSR*, 1990, **313**(6), 1444-1448. [in Russian]
20. Tverskoi, P.N. *The Course of Meteorology*, Leningrad, 1951, Gidrometizdat, 887p. [in Russian]
21. Fligl, R., and Buzinger, J. *Introduction to the Physics of the Atmosphere*, Moscow, Mir, 1965, 467p. [in Russian]
22. Gufeld, I.L., and Shuleikin, V.N. Atmospheric current variations in the period of earthquakes preparation, *Izvestiya AN SSSR. Ser. Physics of the Earth*, 1988, **2**. [in Russian]
23. Shuleikin, V.N. *The Earth and Atmospheric Electricity*, New York, Nova Science Publishers, 2018, 143p.
24. Shuleikin, V.N., Shchukin, G.G., Kupovykh, G.V. *Development of Methods and Means in Applied Geophysics: Atmospheric-Electrical Monitoring of Geological Heterogeneities and Geodynamic Process Zones*, Saint-Petersburg. Publ. TsOP RGGMU, 2015, 206p. [in Russian]
25. Imyanitov, I.M., and Shifrin, K.S. The current status of research of atmospheric electricity, *Uspekhi Fizicheskikh Nauk*, 1962, **4**, 593-642. [in Russian]

26. *The Guide for Surface Observations of Atmospheric Electricity Elements*, Leningrad, Izdatelstvo GGO im. A.I. Voeykova, 1960, 95p.
27. Semenov, K.A. Good weather and atmospheric electricity elements, *Proc. GGO im. A.I. Voeykova*, 1982, **455**, 112-119. [in Russian]
28. Kupovykh, G.V. Negative space charge formation in the vicinity of the Earth's surface under high-mountain conditions, *Proc. VGI*. St.-Petersburg. Gidrometeoizdat. 1996. Iss. 89, C.73-80. [in Russian]
29. Kupovykh, G.V. Simulation of contamination effects on electrical characteristics of the surface atmospheric air, Taganrog. *Izvestiya TRTU*, 2004, No. 5, 259-262. [in Russian]
30. Kupovykh, G.V. Volumetric electric charge in the surface atmosphere layer, Taganrog. *Izvestiya TRTU*, 1998, No. 3, 202-205. [in Russian]
31. Kupovykh, G.V. The surface atmosphere layer electricity, *Izvestiya Vysshikh Uchebnykh Zavedeniy Sev.-Kav. Regiona*. Estestv. Nauki. 1995, No. 4, 32-34. [in Russian]
32. Bricard, J. The effect of radioactivity and contaminations on the atmospheric electricity elements, In Coll.: *Problems of Electricity of the Atmosphere*, Leningrad, Gidrometeoizdat, 1969, 68-105. [in Russian]
33. Kudrinskaya, T.V., Kupovykh, G.V., and Redin, A.A. Comparison of the mathematical simulation results for the electrode effect with the experimental data, *Izvestiya YuFU. Technical Sciences. Actual Problems of Mathematical Simulation*, 2013, No. 4, 72-81. [in Russian]
34. Kupovykh, G.V. Negative volumetric charge formation in the vicinity of the Earth's surface under high-mountain conditions, *Proc. VGI*, St.-Petersburg, Gidrometeoizdat, 1996, **89**, 73-80. [in Russian]
35. Chalmers, J.A. The theory of electrode effect I, *J. Atm. and Terr. Phys.,* 1966, **28**, 565-572.
36. Chalmers, J.A. The theory of electrode effect II, *J. Atm. and Terr. Phys.,* 1966, **28**, 573-579.
37. Chalmers, J.A. The theory of electrode effect III, *J. Atm. and Terr. Phys.,* 1966, **28**, 1029-1033.
38. Chalmers, J.A. The theory of the electrode effect IV, *J. Atm. and Terr. Phys.,* 1967, **29**, 217-219.
39. Crozier, W.D. Atmospheric Electrical Profiles below Three Meters, *J. Geophys. Res.*, 1965, **70**(20), 2785-2790.

40. Kupovykh, G.V., Morozov, V.N., and Shvarts, Ya.M. *The Theory of the Electrode Effect in the Atmosphere*, 1998, Izd. TRTU, Taganrog, 122p. [in Russian]
41. Kupovykh, G.V., The electrode effect in the surface atmosphere layer, *Doctor Thesis*, 2005, Nalchik, 35p. [in Russian]
42. Redin, A.A. Mathematical modeling of electrodynamic processes in the surface layer in conditions of airborne contamination, Taganrog: *Candidate Thesis*, 2011, 19p. [in Russian]
43. Pedin, A.A., Kupovykh, G.V., and Boldyrev, A.S. Electrodynamic model of the turbulent near-surface layer in the presence of multiply charged aerosol particles, *VII All-Russian Conference on Atmospheric Electricity*, St. Petersburg, 2012, 199-201. [in Russian]
44. Pedin, A.A., Kupovykh, G.V., Boldyrev, A.S., and Bukantis, A.A. Electrodynamic model of convective-turbulent surface atmosphere, *VII All-Russian Conference on Atmospheric Electricity*, St. Petersburg, 2012, 202-203. [in Russian]
45. Khrgian, A.Kh. *Physics of the Atmosphere*, Leningrad, Gidrometizdat. 1969, 646p. [in Russian]
46. Gokhberg, M.B., Gufeld, I.L., and Dobrovolsky, I.P. Sources of Electromagnetic Earthquake Precursors, *DAN SSSR*, 1980, **250**(2), 323-326. [in Russian]
47. Gokhberg, M.B., Gufeld, I.L., Gershenzon, N.I., and Pilipenko, V.A. Electromagnetic Effects at the Earth Crust Crushing, *Izvestiya AN SSSR*, *Ser. Physics of the Earth,* 1985, 1, 72-78. [in Russian]
48. Gokhberg, M.B., Gufeld, I.L., Dobrovolsky, I.P., and Nersesov, I.L. Processes of preparation, signs, and precursors of core earthquakes, *Izvestiya AN SSSR*, *Ser. Physics of the Earth,* 1986, No. 2, 59-67. [in Russian]
49. *A Search for Electromagnetic Precursors of Earthquakes*, In Coll. Ed. by M.B. Gokhberg, Publ. IPE AS USSR, 1988, 243p. [in Russian]
50. Sobolev, G.A., and Demin, V.M. *Dynamoelectric Phenomena in the Earth*, Moscow, Nauka, 1980, 215p. [in Russian]
51. *Electromagnetic Precursors of Earthquakes*, In Coll. Ed. by Academician M.A. Sadovsky, Moscow, Nauka, 1982, 88p. [in Russian]
52. *A Search for Electromagnetic Precursors of Earthquakes*, In Coll. Ed. by M.B. Gokhberg. Publ. IPE AS USSR, 1988, 243p. [in Russian]

CHAPTER 3

ATMOSPHERIC ELECTRICITY ABOVE GEOLOGICAL HETEROGENEITIES

The established relationships between hydrogen, methane, radon, and the elements of surface atmospheric electricity prove that earth-atmosphere air exchange determines the space charge of surface air. Stimulation of air exchange is typical of the fault zones of the Earth's crust. Observations of the atmospheric electric field in the profile crossing the fault lead to a reverse electrode effect; research in a seismically active region (Dagestan), showed that field decline is accompanied by a change in sign. Similar effects can be observed over a zone with an abrupt basement roof settling and a sharp increase in the thickness of sedimentary rocks. The polar conductivities of the air increase above underground utilities and karst cavities.

An increase in the density of the deep sub-vertical flow of hydrogen and methane is accompanied by excessive exhalation of radon and a decrease in the atmospheric electric field. Observations of the field above an ore body recorded a signal failure in the projected area of the deposit on the surface. This was the result of gas formation in the ore body cap. Excessive methane content in the surface soil layers above an oil field and above an underground gas storage facility in an artificial reservoir leads to the same effects.

3.1. Surface Atmospheric Electricity above Fault Zones and Areas of Geological Deconsolidation

A fault at the ground surface was chosen to be representative of a relatively broad zone of manifestation of paragenetic related faults, framed in the periphery of areas of increased fracturing. The internal structure was determined by the degree of tectonic activity, the stage of development, the size, and the morphogenetic type of fault. Fault zones are characterized by increased release of volatile gases into the atmosphere. This results in the increased concentration of exhaled radon, the growth of polar air conductivities, and a decrease in AEF.

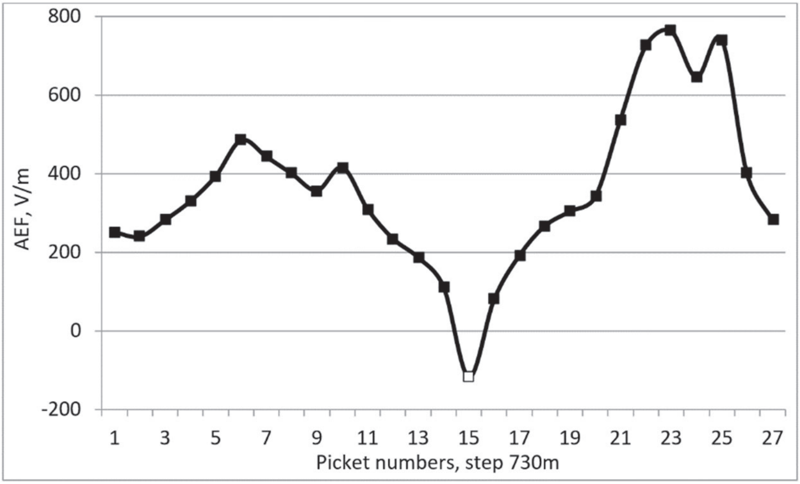

Figure 3.1.1: The averaged three-time AEF-profiling results of the fault zone of the Aktash River, Dagestan. Negative field values (picket 15) were observed in the fault crossing area.

When performing specialized observations of AEF in a seismically active region, such as the Republic of Dagestan, one of the observation profiles was located in the fault zone of the Aktash River between the towns of Khasavyurt and Dylym [1, 2]. The measurements were performed using a field mill Pole-2 installed on the roof of a UAZ-452 off-road vehicle. The instrument plates were installed 2.3 m above the ground. Observation conditions were ideal: an open flat terrain, a lack of traffic on the road, and the meteorological situation fully correspondent with the definition of "fair weather" conditions [3–5]. The total length of the route, which was traversed three times at an average profiling speed of about 35 km/h, was 19 km.

An analog data recorder was used to record AEF variations along the observation profile. Copies of the records from this triple pass are presented in [6, 7]. The correlation coefficients of field variations in the first and second passes of the profile were $k(E_1; E_2) = 0.68$; and in the first and third passes, $k(E_1; E_3) = 0.74$.

Along the central part of the route (picket 15), on a segment 1 km in length, a repeated field decrease with a change in sign to -100 V/m was recorded. At this picket, the profile crosses the fault zone of the Aktash River, where stimulation of the soil-atmosphere air exchange could be observed. The increased density of deep sub-vertical flows of hydrogen and methane led to increased ionizer transport to the surface atmosphere, and negative AEF values were recorded over a kilometer segment. High AEF values along the last third of the route of E ~800 V/m suggested that the geological environment in the observation zone was in a state of contraction, with minimal radon exhalation.

For a comparison of the results of specialized observations of AEF in the fault zone of a seismically active region, we turn to similar measurements on the East European Platform at the Kaluga Ring Structure (Section 1.2) [8]. Based on microscopic studies of the crystalline schist and granite-gneiss breccia, the Kaluga Ring Structure can be characterized as an impact formation. Here, three systems of ring faults, 12–14 km, 22–26 km, and 36–40 km in diameter, were outlined by drilling.

Observations were performed from the center of the structure using four radial profiles. AEF measurement profiles were performed with lengths of 11 km, 12 km, 11 km, and 8 km; the gas observation profiles were 11 km, 7 km, 7 km, and 6 km long. Gases were sampled at 1,000 m intervals, and the field was observed continuously from onboard the moving vehicle.

Field measurements on profiles 3 and 4 yielded little information. At profile 3, 4 km from the center of the structure there was a forest area close to the observation route and the AEF was shielded; from the fifth kilometer of profile 4, there were road works and the surface air layer was saturated with dust and exhaust gases from machinery. Nevertheless, at the gas observation pickets, the correlation coefficients between the volumetric activity of the soil radon and AEF values turned out to be significant, fitting the range *k* = (0.54–0.84).

Most deserving of attention were the AEF variations recorded at profiles 1 and 2. They stretched from the southwest to the northeast and were 23 km in length; they were combined into one measurement profile [2, 9]. The field values at each picket, except for the first and the last ones, were averaged over a segment of +/- 300 m from the kilometer mark. At pickets 1 and 21, averaging on a 300 m segment was performed. Figure 3.1.1 shows the results obtained for spatial field variations.

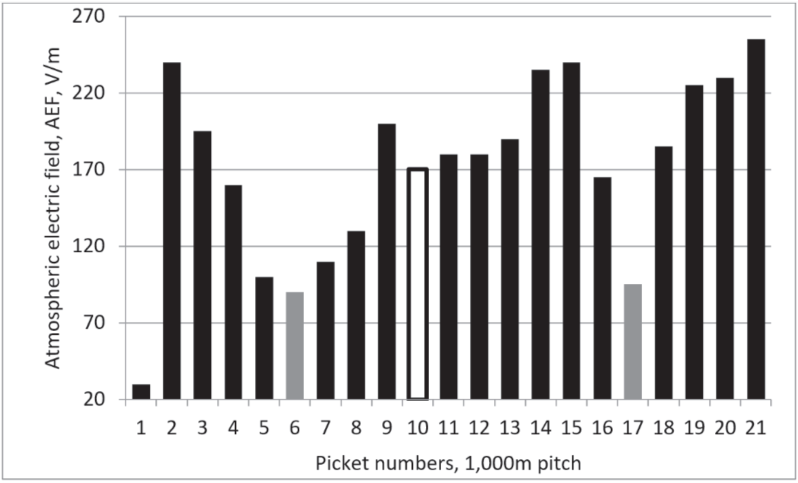

Figure 3.1.2: AEF spatial variations from the combined profiles of 1 and 2.

As each point was taken by averaging over a 600 m segment of the profile, the field variations are presented in the form of a histogram. Picket 10 was located at the central point of the ring structure. According to drilling data, the intersection of the profile with the first ring structure falls at pickets 6 and 17. The sharp decline in the field at the first picket was determined by the high content of the parent matter in the gravel at the site on the side of the road where the AEF observations were performed.

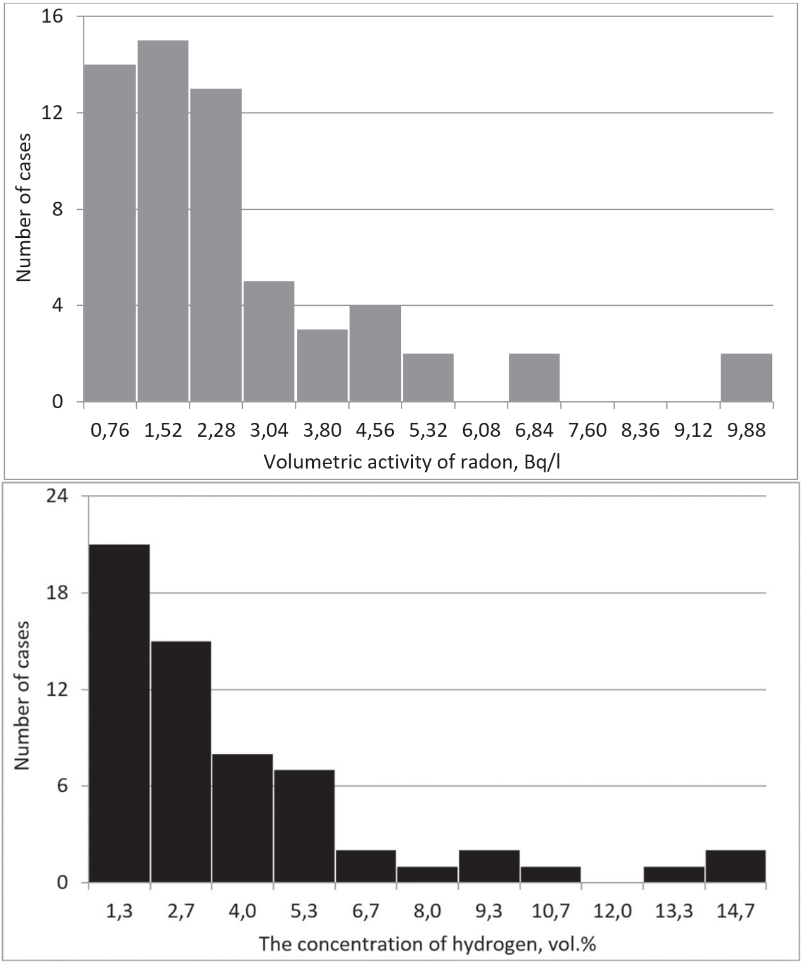

Figure 3.1.3: Histograms of volumetric radon activity and soil hydrogen concentration distribution along observational profiles at the Kaluga Ring Structure.

Figure 3.1.2 gives histograms of radon activity distribution and the concentration of hydrogen in the soil, the maximum flows of which were concentrated in tectonically disrupted structures. At the majority of the observation pickets, the soil hydrogen concentration within the ring structure did not exceed the background values of the East European Platform [10]. The same was true for radon flows. These equilibria are disturbed in areas influenced by the faults that define the ring structure's perimeter and regional tectonic faults that intersect it.

In autumn 1999, another series of specialized AEF observations were carried out over the Aleksandrovsky Fault (Belarus, Gomel Region) [11]. The measurement conditions were perfect: the surveyed area was kilometers away from the nearest highway and even the dirt roads were grassed; there was total calm and no cloud.

The measuring device (a Pole-2 field mill) was installed on a 2 m long rod and fixed on the front bumper of the UAZ-452. The elevation of the measuring plates was 0.8 m. For this instrument, a reduction factor of 3.84 was used. The measurement profile across the Aleksandrovsky Fault was passed over twice. The relative scatters of average values in the fault zone did not exceed 7 %; on the sides of the fault this figure was 5 %. The measured variations of the field from two passes, *E*, and those calculated with the reduction factor of *E*/3.84, are shown in Figure 3.1.3.

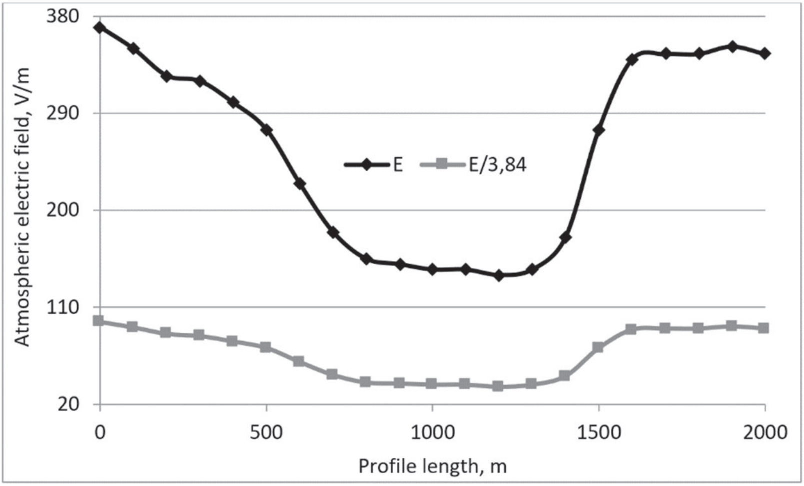

Figure 3.1.4: Atmospheric electric field variations measured across the Alexandrovsky Fault (Belarus, Gomel Region), *E*; field variations with the reduction factor, *E*/3.84.

Measurements of soil air radon and hydrogen in some points above and at the sides of the fault showed an almost two-fold increase in the volumetric activity of the ionizer and hydrogen content in the soil air above the fault zone compared to [11].

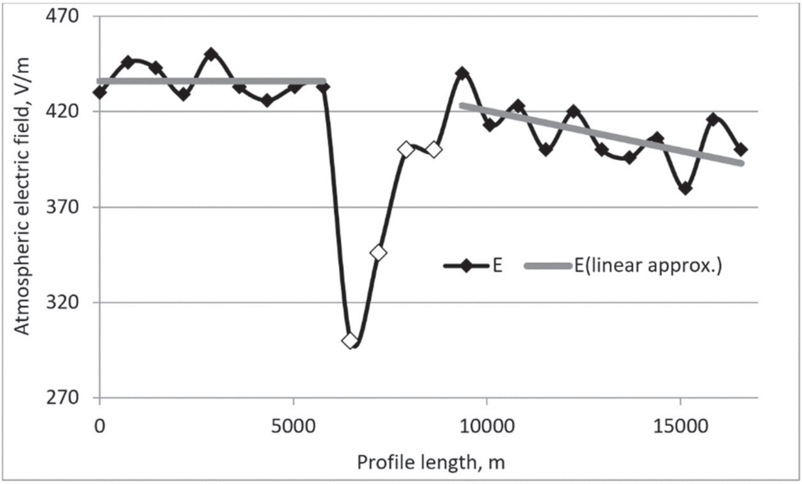

Figure 3.1.5: AEF variations above the area of sharp basement roof settling and an increase in sedimentary rock thickness.

If the soil-atmosphere gas exchange in the fault zones mainly occurs through faults and zones of increased fracturing, then in sedimentary rocks this process occurs through the pore space. The gas permeability of sedimentary rocks is substantially higher than that of bedding rocks. During geoelectric prospecting by the Stepyanka Geophysical Expedition (Belarus), a section with a sharp lowering of the basement roof was revealed along a segment of the Minsk-Brest highway, with a sharp increase in the thickness of sedimentary rocks. Figure 3.1.4 shows AEF variations from the averaging of the results of two passes along the route.

Profile sections for 0 m–5,800 m and 9,400 m–16,600 m are shown in the graph to illustrate the recorded background signal level along the route. For ease of comparison with the field decay in the area of sharp lowering of the basement roof, linear approximations are given. As one would expect, the cause of AEF decline along the 5,800 m–9,400 m segment is the increase in the density of sub-vertical volatile gas fluxes with increasing sedimentary rock thickness.

The results shown allow us to speak of the atmospheric electric field as a fully-fledged geophysical parameter, which can be used effectively in the study of fault zones. Several reasons support this conclusion:

- AEF profiling was performed continuously from a moving vehicle, which eliminated the possibility of missing the desired geological object;
- AEF variations above the fault zone showed the highest contrast since they were determined by the product of the ionizer (radon) density present in the soil and the total density of the carrier gases (hydrogen and methane);
- a high observation rate allows us to consider AEF to be a parameter and characteristic that allows the monitoring of the current dynamics of a fault zone with a low labor cost.

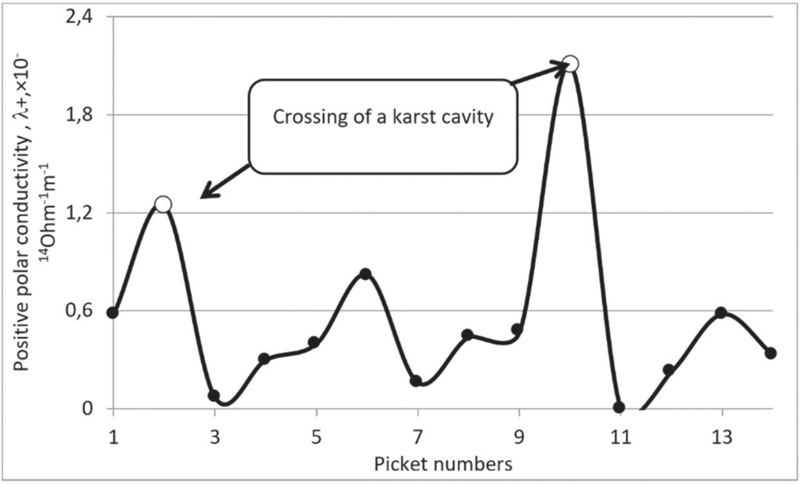

Figure 3.1.6: Variations of the positive polar air conductivity in the profile twice crossing a karst cavity.

At the current rate of industrial and civil construction and broad urbanization of the territory being studied, preliminary geological analysis and geotechnical surveys of future construction sites are insufficient. Underground karst formations are a typical cause of damage to objects under construction or operations of city building. The conventional solution to the problem of identifying karst features is through a geodetic survey of the area. In recent years, seismic and geoelectrical prospecting, microgravimetric surveys, and radio wave scanning have all been applied [12, 13]. The results presented above indicate the possibility of using atmospheric-electrical observations to detect soil loosening.

However, due to the shielding effect of buildings, power lines, and planting, the use of AEF within the urban area is impossible. Let us consider the results of the profiled observations of polar conductivities in the air in solving this problem.

Measurements were performed in Tula City above a long karst cavity, the location of which was confidently tracked by following cracks in the walls of houses. The observation profile passed around one house that was horseshoe-shaped, which allowed us to cross the karst cavity twice (Figure 3.1.5) [6, 7].

Unfortunately, the negative polarity channel amplifier failed during measurement. Nevertheless, the position of the karst cavity could be clearly distinguished by maxima in the variations of positive polar conductivity, which coincided with the position of cracks in the walls of failing building.

The experiments were continued in Moscow where subway lines of various depths were investigated as areas with soil loosening. Figure 3.1.6 shows the results of profile observations of polar air conductivity across a subsurface subway line, about eight meters beneath the ground surface (near Kon’kovo Subway Station in Moscow) [14, 15]. Measurements were carried out at 11 pickets, set up with a 4 m pitch. The exception was the section of the profile in the 28–44 m segment, where a road with reasonably heavy traffic passed. The total length of the profile was 52 m.

The plots shown allow us to confidently map the intersection profile of the subway line from the surface of the ground. The excess of the signal level of total polar conductivity at the maximum (mark 28 m) against the average background value at the interval of 0–28 m was about 5.9.

As expected, the recorded negative conductivity in the realizable technique of observing soil air polar conductivity exceeded positive conductivities. The observed result logically followed from the redistribution of positive and negative light ions above the negatively charged ground surface—the electrode effect.

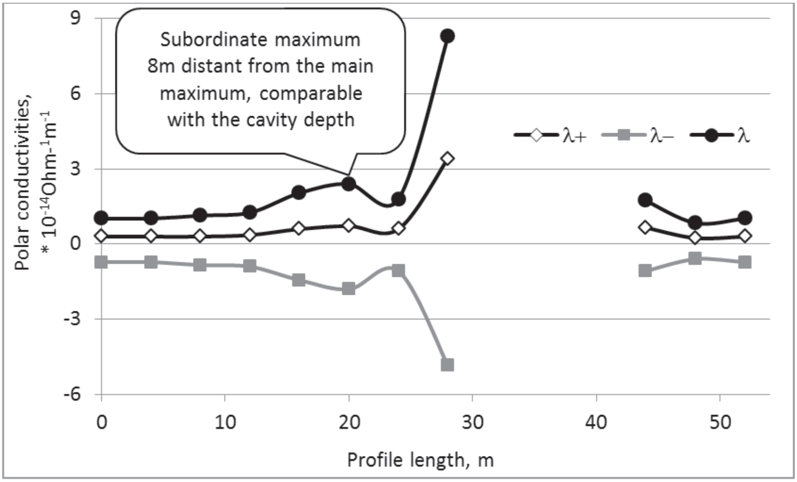

Figure 3.1.7: Variations of air polar conductivities recorded in the profile crossing the line of the subsurface (~8 m) subway line.

Attention is drawn to the presence of an additional maximum on the plots in Figure 3.1.6. Its occurrence was associated with the specific features of the sub-vertical soil air flux flowing around an underground engineering facility. The air flow density reached its maximum above a cavity; at a distance comparable to half the depth of the cavity, a minimum occurred; the next maximum appeared at a distance comparable to the cavity depth. To put it differently, variations of polar conductivities along the distance from the cavity were close to CosX/X function, and the distance between the first and the second maxima was comparable to the depth of the cavity [16].

It is necessary to notice another experimental fact. Each measurement, the value of which is shown in Figure 3.1.6, was performed in the absence of trains in the tunnel. When a train was passing, in the positive and negative polar conductivity channels, a virtually two-fold increase in the signal was recorded, as a result of soil-to-atmosphere air exchange stimulated by human-generated seismic noise and excessive air pressure in the tunnel, as the air is pushed by the train.

The experiment was repeated above a deeper level subway line with a depth of about 25–30 m: the middle of the metro bridge on the Vorobyovy Mountains to the university station leg (Figure 3.1.7).

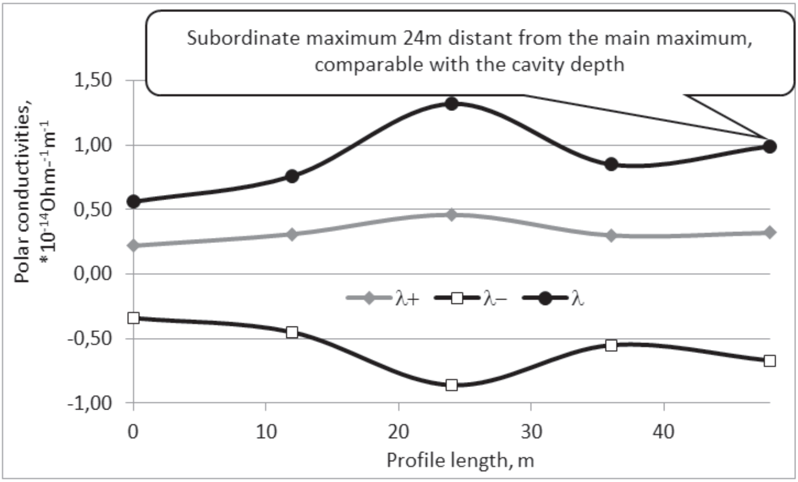

Figure 3.1.8: Variations of polar air conductivities recorded in the profile crossing the deep subway line at a depth of 25–30 m.

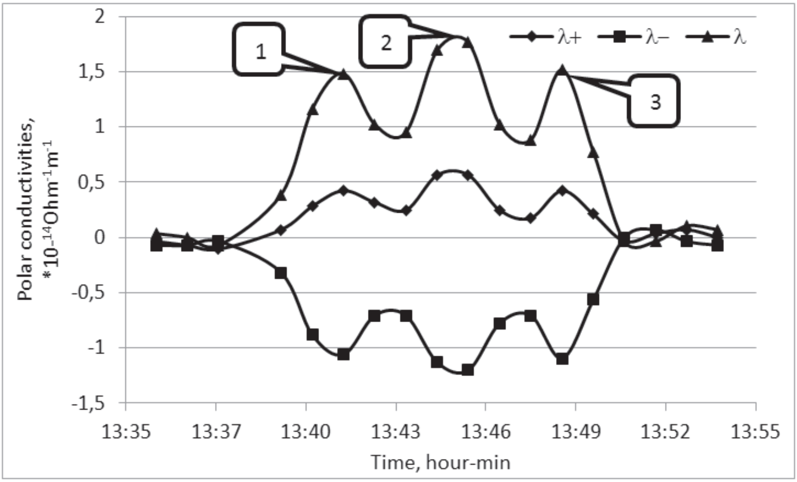

Figure 3.1.9: Temporal variations of positive, negative, and total polar conductivities above a deep level subway line. Time intervals at 1^h35^m–1^h39^m p.m. and 1^h50^m–1^h54^m p.m. present records of zero-level aspirating condensers. Points 1–3 were recorded as subway trains passed beneath the observation picket.

Above the metro line—the 24 m point—the total polar conductivity exceeded the signal level at point 0 by a factor of 2.4. Moreover, at the 48 m point, a subordinate maximum was seen at a distance of 24 m from the main one.

In addition to the profile observations at point 24, directly above the tunnel, a ten-minute temporary recording of the positive and negative polar conductivities was made (Figure 3.1.8) [6, 7].

The man-made seismic effects caused by a train passing noticeably increased the signal level, primarily in the negative conductivity channel.

Data shown from the field observations convincingly indicate that the atmospheric electric field and the polar air conductivities undergo contrast changes above fault zones and small loosening effects of the Earth's crust. As assumed in Section 3.1, these changes range from several tens to several hundred percent of background levels and, correspondingly, exceed possible instrumental errors by many times. Moreover, the presence of collateral extremes in records outside the studied anomalous contour made it possible to estimate the occurrence of loosening at the depth being studied. The presence of a seismic disturbance in the medium inevitably increased soil-to-atmosphere air exchange, as can be seen in the records of the polar air conductivities above subway lines when a train was passing.

3.2 An Ore Body and an Oil Deposit

Electrochemical processes at the interface between media with electronic and ionic conductivity, for example, at the interface of an ore body and host rocks, create conditions for excessive gas liberation. In a case of a shallow ore body (with a depth comparable to the transverse size of the deposit), the ascending sub-vertical flow of volatile gases had a higher density, exceeding the flow density above the host rocks. With the presence of hydrogen and methane in the ascending stream, radon transport to the atmosphere inside the contour close to the projection of the ore body to the ground surface increased, inevitably leading to a decline in the AEF.

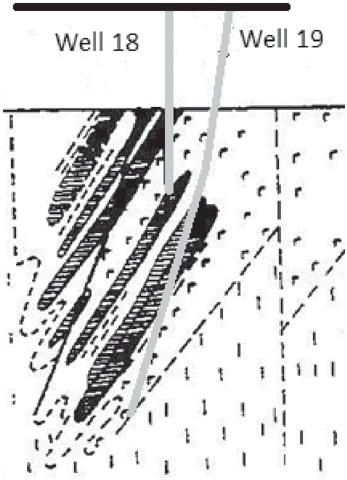

Figure 3.2.1: Section of the Novoselkovsky ilmenite-magnetite ore occurrence.

The assumptions made above were verified in June 1986 at the Novoselkovskoe ilmenite-magnetite ore, which has a depth of about 200 m and a typical transverse size of about 400 m. Exploration work on the ore body was carried out by the Stepyanka Geophysical Expedition (Belarus). A cross-section of the ore body is shown in Figure 3.2.1.

AEF measurements on the ore body area were carried out using two Pole-2 field mills. One of the measuring devices was installed in a stationary position near the object of study and was used to control for temporal field variations. The second measuring device was used to record core field variations above the geological heterogeneity. Field sensor noise was 2 V/m [17].

Before starting the work, a two-day sensor check was performed. Through comparison of individual sections of the continuous two-day recording period, it could be seen that the maximum discrepancy of the readings reached 9 %. The most likely reason for such a discrepancy was the temperature drift in the amplification and measuring elements of the sensors; discrepancies were observed in the afternoon.

Initial specialized AEF observations at the Novoselkovskoe ore body were performed on June 24, 1986. Unfortunately, the area to be studied was crop-seeded, which made it possible to set up only one profile. The technique of continuous profile observations had not yet been developed. Therefore, the measuring device at each of the pickets was taken off the vehicle and installed on a mown area of about 1 m^2. The elevation of the measuring plates of the Pole-2 field mill was 0.4 m; the height of the crops was 0.5–0.6 m and so the signal was partially shielded by seeded crops.

Along the observation profile of 800 m in length, nine observation pickets were set up with a 100 m pitch. The first two and the last three pickets were set outside the projected ore body; 3–6 pickets were set in the ore body zone.

Unfortunately, the meteorological situation was not conducive to taking measurements, with 4 points on the cloudiness scale and blustery wind. Measurements at each observation picket were carried out over 1–2 minutes with strict matching of the readings of the stationary field mill. At these time intervals, the recording of the signal of the stationary device stabilized. The full measurement cycle took about three hours.

The measurements were repeated the next day under more favorable weather conditions. The recorded mean decrease in AEF over the ore body zone was ΔE_{1986} ~40 V/m, which exceeded the errors of the measuring devices [18–20].

In 1986, the AEF profile observations were preliminary, being a first experimental investigation into the spatial field distribution over the geological heterogeneity. In work performed between August 15 and September 01, 1987, a multi-profile AEF survey of the Novoselkovskoye ore deposit was carried out. Before starting the measurements, the studied area was mown to make it possible to set up 11 observation profiles in the projection area of the ore body. The first four profiles followed the profile line in a north-northwest direction, with a 50 m pitch and a length of 1,300 m. The rest of the profiles were set across the first ones with a 100 m pitch and 200–450 m in length. The length of the shorter profiles was limited by the topographic features of the terrain.

The first time, the measurements were carried out using two field mills. However, as weather conditions were conducive for observation, strict matching of the measurement time intervals was not required. Field measurements across the profiles were carried out continuously; the mobile field mill was installed on the roof of the UAZ-452 vehicle with a 2.3 m elevation of the measuring plates. On the sled trailer, the elevation of the measuring plates was 0.5 m to 0.6 m. The data obtained with the latest installed version of the measuring device is shown in Figure 3.2.2 [6, 7].

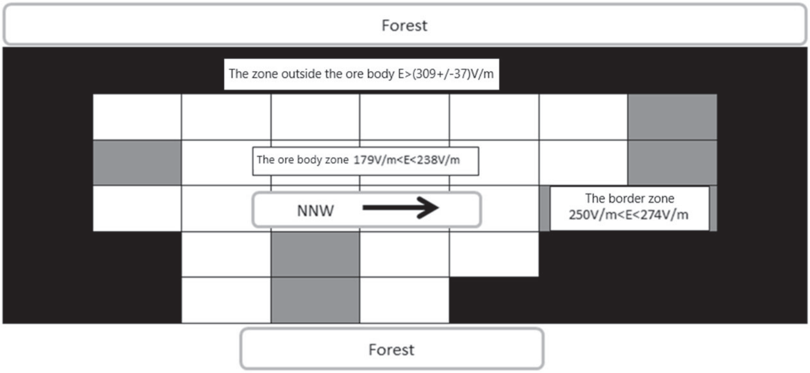

Figure 3.2.2: Results of the multi-profile AEF survey of the Novoselkovsky ilmenite-magnetite ore deposit.

The average AEF decline above the ore body zone was ΔE_{1987} ~88 V/m, which is almost twice as large as the measurement data obtained in 1986 of ΔE_{1986} ~40 V/m. The reason for this discrepancy is, partly, the shielding of the field by sown crops and, partly, the different meteorological conditions of the experiment and the higher elevation of the measuring plates in the work performed in 1987.

The main task of the work at the Novoselkovsky ilmenite-magnetite ore deposit was reduced to a demonstration of the possible use of profiled AEP observations for non-contact determination of an ore body's contour from the ground surface. The results obtained were entirely consistent with the proposed model of relationships between gas fields of the Earth and AEF. Excessive discharge of hydrogen, formed by electrochemical processes in the ore body cap, to the surface atmosphere inevitably led to an increase in soil radon exhalation and to a decrease in the atmospheric electric field.

Methane is the second carrier gas to bring the ionizer to the surface soil layers and the atmosphere; this was the same in the oil reservoir plume. Let us consider the effect of oil-plume methane to changes in the atmospheric electric field.

According to data in the literature, the concentration of methane in the troposphere is influenced by the oil-and-gas potential of the subsoil [21]. Methane content in the troposphere above oil and gas structures in the Bukhara-Chardzhou Tectonic Stage is 1.2–1.5 times higher than the mean planetary content. To put it differently, excessive discharge of methane to the surface soil layers and the atmosphere takes place.

Field studies have shown that within the contour of an oil deposit projection to the ground surface, the concentration of combustible gas in the surface layers of the soil increases [22, 23]. The results of laboratory analysis of soil air samples for methane content taken above the oil field and outside it are shown in Figure 3.2.3. The level of soil methane concentration turned out to be rather small, about (0.5–1.7) × 10^{-4} vol.%, which is comparable to the average world level of methane concentration of 0.8 × 10^{-4} vol.% [24].

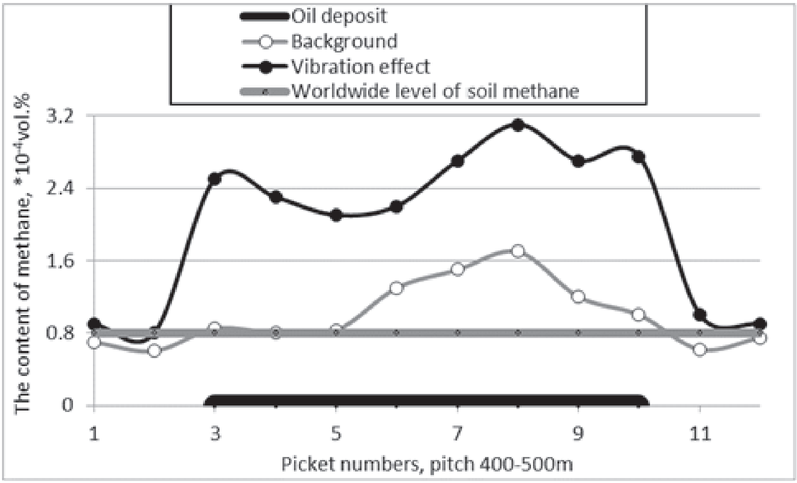

Figure 3.2.3: Soil methane content in the profile across the oil deposit before (background) and after the vibration effect.

To increase the contrast in the difference in methane content above the deposit and beyond its limits, active vibrational exposure to the soil was used. The experiment with sampling was repeated, but each soil air sample was taken after 10 minutes of operation of the SV 20/60 or SV 10/100 type seismic vibrator in the range of anthropogenic microseisms of 5–25 Hz. The second curve in Figure 3.2.3 shows that with the ratio of the average methane concentration above the deposit and host rocks, the sampling value was about 1.7; after vibration exposure, it was significantly higher—above 2.8.

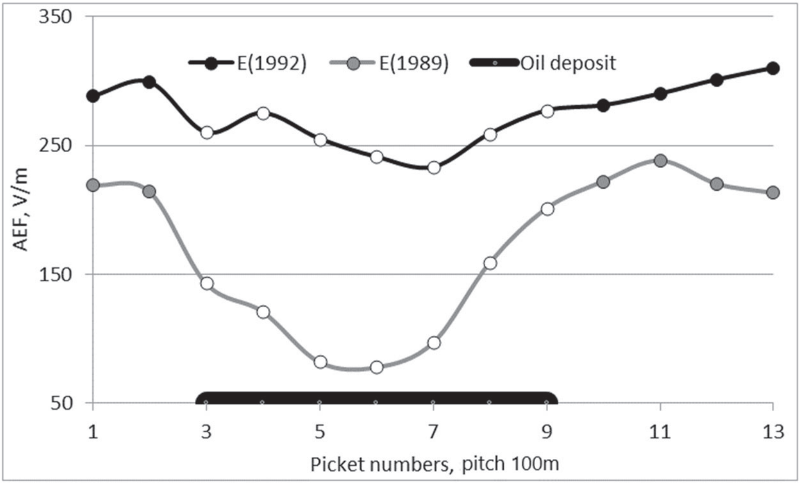

Figure 3.2.4: Variations in the atmospheric electric field across the profile of an oil well. *E*(1989) - the beginning of operations; *E*(1992) - the result of a 3-year well operation. The Third Rechitsky Oilfield, Belarus.

The initial results of profile AEF observations above the oil deposit were obtained at the site of the Third Rechitsky Oilfield, Belarus [25, 26]. The work was carried out twice. The first stage took place in the summer of 1989, when a new well was commissioned. Repeat observations were carried out in the summer of 1992, after three years of well operation (Figure 3.2.4). As might be expected, in three years the AEF decline above the deposit significantly decreased as a result of a lowering in the pore pressure during operation and flooding of the reservoir—this caused a reduction in the methane density of the oil plumes.

Soil radon is the intermediary between methane in the oil deposit plume and AEF. First of all, bubbles of the carrier gas increase the radon content in the surface soil layers and only then do they carry the ionizer to the surface atmosphere. Let us consider the results of observations of the soil radon volumetric activity and AEF at the Aleksandrovskoe Oilfield in Belarus (Figure 3.2.5) [6, 7].

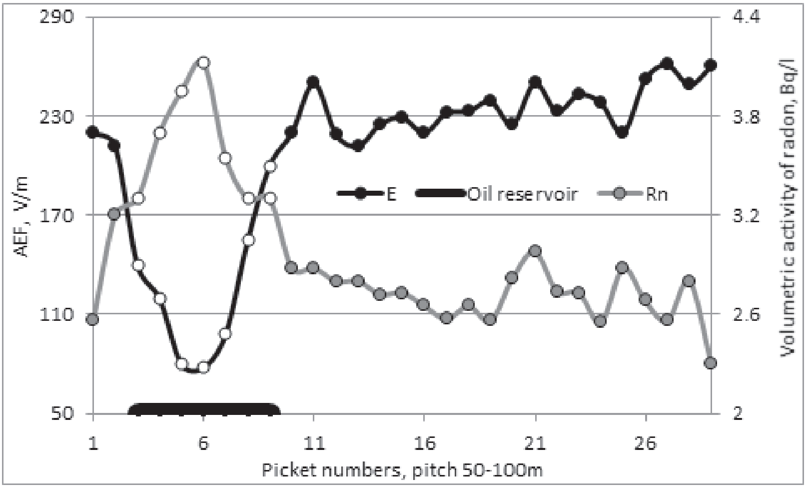

Figure 3.2.5: Variations in the atmospheric electric field and volumetric activity of soil radon above the Aleksandrovskoe Oilfield, Belarus.

Numerous bushes and trees were scattered across the study area shielding the field; there were also small boggy areas where biogenic methane could have been present. The selected observation profile traced out a broken line and consisted of 29 pickets set up with a pitch of 50–100 m. In the zone of pickets 3–9, the profile studied crossed the oil reservoir and provided low field values due to the elevated soil radon content transported by methane in the petroleum plume. The array of 29 pairs of observation data was divided into two parts—above the reservoir and beyond the reservoir. The linear relationship between the field and radon was examined. These approximations are presented as follows, with a confidence value of about 0.8: $E(\mathrm{Rn})_{2\text{-}9} = 553.3 - 119.2 \times \mathrm{Rn}$ and $E(\mathrm{Rn})_{1,\,2,\,10\text{-}29} = 377.4 - 55.2 \times \mathrm{Rn}$ (Figure 3.2.5). The numerical coefficients take the dimension of V/m and values of soil radon volumetric activity are normalized to 1 Bq/l.

As follows from the plot in Figure 3.2.3, the average volumetric activity of soil radon beyond the reservoir contour was quite stable and amounted to $\mathrm{Rn(ave)}_{1.2,\,10\text{-}29} = (2.73 +/- 0.18)$ Bq/l. The increase in soil radon volumetric activity above the oil deposit can be explained by the participation of oil plume methane in radon transfer. The increase in the contribution of petroleum plume methane to this growth can be roughly estimated from the ratio of volumetric radon activity in the petroleum plume to that beyond the deposit, which was about 1.3. This value was slightly lower than the estimate obtained in Figure 3.2.4 of about 1.7.

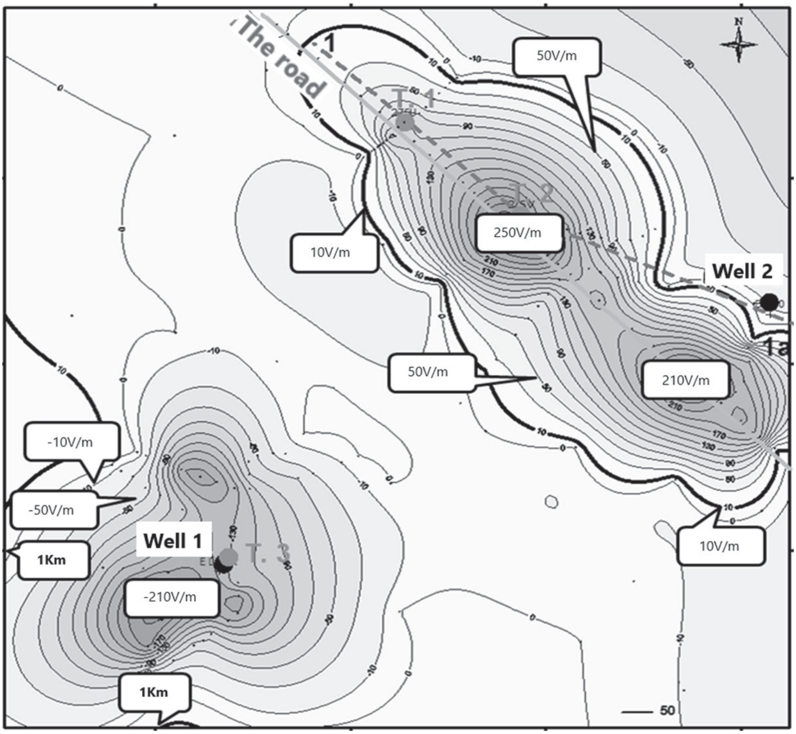

Figure 3.2.6: AEF isolines near the Satybaldy-Karsak Structure, Guryevsky Arch, West Kazakhstan. A positive field anomaly of 210 V/m to 250 V/m was found in the NE part above a productive oil deposit; a negative field anomaly of about -210 V/m was found in the SW part above a non-productive deposit.

The results from above the ore body (Figure 3.2.2) and the oil reservoir (Figures 3.2.3 to 3.2.5) fully fit the framework of the model of the relationships between gas and electric fields at the ground and in the atmosphere (Table 1.2.1). Increased release of hydrogen and methane to the atmosphere inevitably leads to an increase in soil radon exhalation and to a decline in AEF above the geological heterogeneity being studied. However, in the scientific literature, one can find a study [27] that shows the inverse result to Figure 3.2.6. In the northeastern part of the Karsak Structure, Guryevsky Arch, western Kazakhstan, a positive AEF anomaly was recorded. The anomaly of the northeastern extension showed two distinct maxima of about 250 V/m. Drilling results found oil reserves beneath it.

In the southwestern part of the structure (Figure 3.2.6), another anomaly was detected; this time it was negative. Its minimum value reached -210 V/m. According to the survey results, this territory was considered to be unproductive in terms of commercial oil reserves, as the reservoir beds are saturated with saline water.

According to the geological data, the identified productive and nonproductive oil deposits are overlapped by the Karsak Salt Dome Structure. The dimensions and location of the salt dome have been defined through electrical prospecting and drilling. For the oil deposits shown in Figures 3.2.3 to 3.2.5, the reservoir covers weakly prevent the sub-vertical spreading of the petroleum plume, increasing methane flow density. The sealed salt dome eliminates the possibility of the movement of the deep sub-vertical flow of volatile gases and petroleum plumes to the ground surface. There is an accumulation of gases under the dome and subsequent sub-vertical discharge along its perimeter. This is most likely the cause of negative AEF values in the southwestern part of the study area. As such, in the case being considered, shown in Figure 3.2.6, deep and shallow sub-vertical flows of volatile gases from oil deposits are regulated by the salt dome and do not overburden the area of the deposit.

3.3. Atmospheric Electricity above a Gas Deposit

The atmosphere and the world's oceans act as reservoirs where cold degassing products—methane and its homologs; hydrogen, and other volatile gases—inflow from the Earth's solid sphere. The photochemical reactions of hydroxyl, with the participation of solar radiation, work with methane flow in the atmosphere, and encourage the fixation of carbonates at the bottom of the oceans. The average life span of methane molecules in the atmosphere is about five years. The constancy of atmospheric methane content is achieved by its discharge from the Earth's surface at the volume rate of 2.0 l/m^2 per year [28].

Chemical analysis of gas bubbles in ice samples from Greenland and Antarctica [29, 30] have shown that 60,000 years ago the methane content in the surface atmosphere was about 0.5 × 10^{-4} vol.%; 20,000 years ago this value was 0.36 × 10^{-4} vol.%; 10,000 years ago, it returned to the level of 0.5 × 10^{-4} vol.%; and 300 years ago it was equal to 0.8 × 10^{-4} vol.%. Assuming that climatic, seismic, and deformation processes acting on the Earth have changed little over the past 300 years, it is possible to suggest that this methane flux per unit area of the ground surface is close to the modern value.

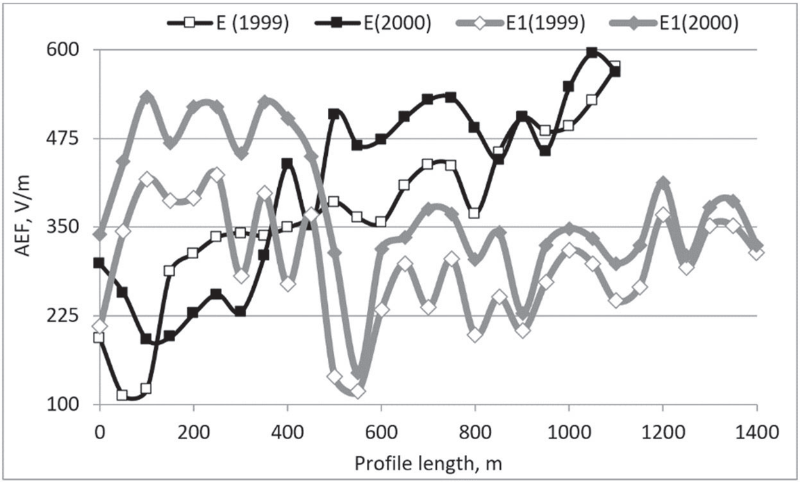

Figure 3.3.1: AEF profile variations registered in 1999 and 2000 at the site of the Schelkovskoe GSF. The decline in the signal E_1 at 0 m and 50 m is due to the screen effect of the lightning conductor.

In the seventeenth century, the Industrial Revolution, through anthropogenic activity, increased the atmospheric methane concentration. According to observations made in 1975, it was at a level of 1.4 × 10^{-4} vol.%; by 1987, this value had reached 1.7 × 10^{-4} vol.% [24]. Using the results of atmospheric-electrical and hydrogen-radon observations, let us consider the influence of the operation of underground combustible gas storages on this anthropogenic discharge.

The North Stavropol Underground Gas Storage Facility is located in the depleted reservoir bed of the North Stavropol Field [31]. Figure 1.3.3 shows the measured and average AEF values in the profile, extending beyond the contour of the reservoir bed. The average field beyond the reservoir bed declined by 1.4 times. This was caused by an increase in the concentration of methane in the soil by a factor of 2.3.

A slightly different situation could be observed at gas storage facilities in artificial reservoir beds. The initial results were obtained at the Schelkovskoe Gas Storage Facility. Figure 3.3.1 shows recordings of the field variations in two profiles crossing the reservoir bed contour with a yield to the injection-zone side. AEF variations in the profiles obtained in 1999 and 2000, fit well with each other: $k[E(1999); E(2000)] = 0.80$; $k[E_1(1999); E_1(2000)] = 0.81$. The profile yield to the contour of the injection zone volume was accompanied by a confidently recorded field decrease.

About 15 km of profiles were defined at the site of the gas storage facility and beyond its contour. At each site repeated measurements of the AEF were performed. According to the observations performed in 1999, the average AEF above the gas storage was equal to $E(1999)_{\text{gas storage}} = 284$ V/m; the average AEF value beyond the gas storage was equal to $E(1999)_{\text{beyond}} = 557$ V/m. Following the observations made in 2000, similar estimates led to the following average AEF values: $E(2000)_{\text{beyond}} = 599$ V/m; $E(2000)_{\text{gas storage}} = 368$ V/m.

Work performed in 2000 at the site of the Kasimov Gas Storage Facility saw similar, but less contrastive results. The average field values along the segments of three profiles located above the injection volume were equal to 138 V/m, 136 V/m, and 140V/m. Field values outside the area of the injection volume projected to the surface fell within a range of 184 to 240 V/m.

Geodetic surveys on the territories of gas storage facilities confidently indicate modern vertical movements of the Earth's crust recorded during the process of injection. In particular, a vertical ground uplift of 2 cm was recorded during leveling at the Krasnopartizansky Gas Storage Facility (Ukraine). Ground movements caused by the injection process could be clearly seen. The injection of a combustible gas at excess pressure into a reservoir bed causes deformation of the cap rocks, eventually reaching the Earth's surface. Here the pore space packed with volatile gases of soil air is deformed, i.e., it will expand. Volatile gases are discharged into the surface atmosphere; i.e., intensifying soil-atmosphere air exchange [32, 33].

Over the decades of operation of underground gas storage facilities in reservoir beds, the methane content in aquifers and surface soil layers increases due to poor quality caps. Naturally, the maximum stimulation of the soil-atmosphere air exchange is observed during the injection cycle. Figure 3.1.1 illustrates this, presenting observations from 1999 and 2000 at the Schelkovskoe Gas Storage Facility, which were carried out in the first ten days of September—the final days of the autumn injection cycle.

Figure 3.3.2 shows the field variations in the profile crossing the line of methane spreading from the injection well cluster to the dome of the Kasimov Gas Storage Facility.

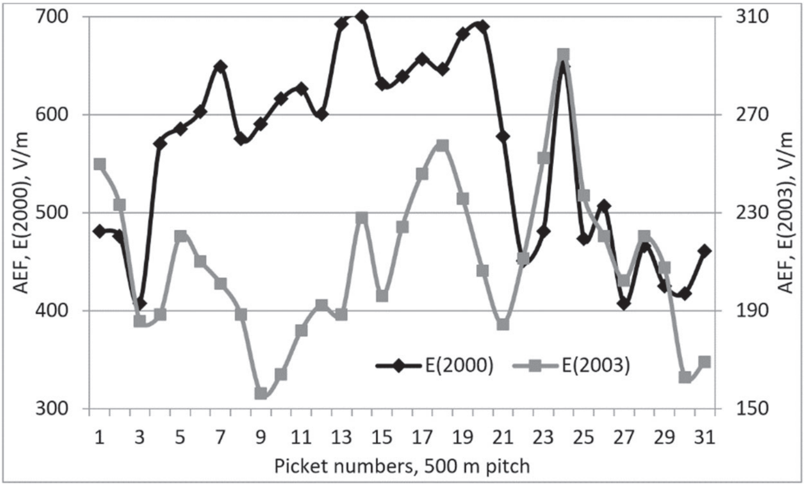

Figure 3.3.2: The results of AEF observations from a profile crossing the line of methane spreading from a group of injection wells to the dome of the gas storage facility.

Various meteorological conditions led to the average AEF values in the profile recorded in 2000 exceeding the field average of 2003 by a factor of 2.7. Therefore, for the convenience of comparing recorded variations, their absolute values are given for different scales. The correlation coefficient for the entire array of observation data in the profiles of 2000 and 2003 is insignificant, $k = 0.14$. However, if the measurement data are separated into two parts according to the pickets (1–3, 22–31) and (4–21), then the correlation coefficients become significant: $k(1–3, 22–31) = 0.82$ and $k(4–21) = 0.51$. Signal failure at the line of pickets 6–17 in 2003 was a consequence of the gas spreading towards the dome of the gas storage facility.

In the proposed model (see Section 1.2), except for methane, all the listed gas and electrical parameters are amenable to rapid field observation, opening up the possibility of its indirect assessment. Let us consider the results of such an assessment performed at the site of an underground gas storage facility. On the one hand, this is extremely important from the standpoint of the environmental safety of a facility and, on the other hand, it is dictated by the developed dynamics of soil methane content in the repeated annual cycles of injection and removal of combustible gas [25, 33].

Working formulas were introduced as functions of pairs of values (soil radon—atmospheric radon); (soil radon—AEF); and (soil radon—polar air conductivity) [34]. We turn our attention to the working formula for the first pair of values, since the single reading error of the radon sensor was at its maximum. In particular, in an area with a methane concentration of (10^{-6}–10^{-5}) vol.%, the working formula [6, 7, 34] was:

$$CH_4 = (20.31 \times Rn - 2.70)/10^6 \times Rn, \text{ [vol.\%]} \qquad (3.3.1)$$

Rn and Rn(a) values were normalized by 1 Bq/l. The participation of hydrogen and methane in radon transport was 15 % and 85 %, respectively (see Section 1.3).

Let us evaluate the errors of the introduced working expression to calculate the methane content. The total error of methane determination, as a function of the soil and atmospheric radon expressed in (3.3.1), can be written in the form:

$$\Delta CH_4 = \{[\Delta Rn(a) \times dCH_4/dRn(a)]^2 + \\ + (\Delta Rn \times dCH_4/dRn)^2\}^{1/2} \qquad (3.3.2)$$

The average value of the soil and atmospheric radon volumetric activity over the data array used at the introduction of the expression (3.3.1) - Rn(ave) = 0.97 Bq/l, Rn(a; ave) = 0.48 Bq/l; the average concentration of methane was $CH_4 = 7.26 \times 10^{-6}$ vol.%. The relative measurement error of the soil and atmospheric radon volumetric activity was about 17 % (see Section 1.1). For these average values, the absolute error of methane determination was equal to $\Delta CH_4 = 2 \times 10^{-6}$ vol.% and, consequently, the relative error was $\Delta CH_4/CH_{4(ave)} = 28$ %.

One more feature of Eq. (3.3.1) should be emphasized. The required concentration of soil methane is proportional to the ratio Rn(a)/Rn, which means minimizing the daily variations of the controlled parameters. In turn, these are capable of increasing the uncertainty of the calculation.

Figure 3.3.3 shows the results of the soil methane content calculations from observations made in 2006 [6, 7, 35, 36].

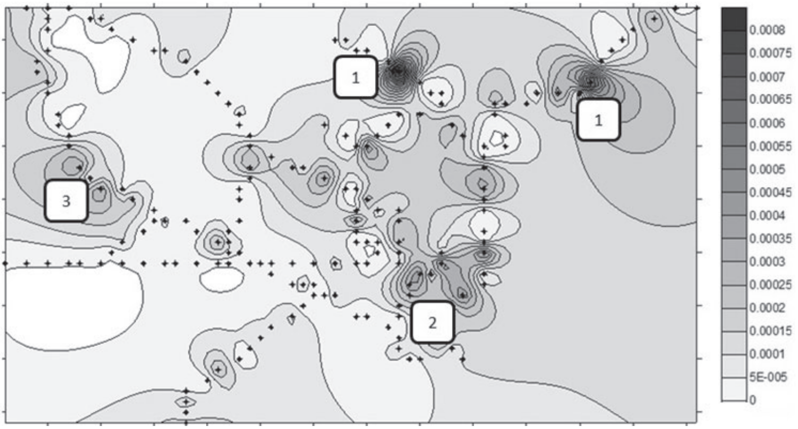

Figure 3.3.3: 2D representation of soil methane content distribution at the site of the North Stavropol GSF according to measurements performed in 2006, × 10⁻¹ vol.%.

In the northeastern and northern sectors of the study area, two pronounced methane anomalies, of grade 1, are located. In both cases, observation profiles crossed boggy areas (the presence of reeds is distinctive), i.e., in these sections, biogenic methane was obviously present.

Point 2 marks the second most significant, but less pronounced anomaly of methane content in the southwestern sector. This is the area of Ryzdvyany Farmstead, where household gas leaks are possibly aggravated by man-made seismicity from motor and rail traffic.

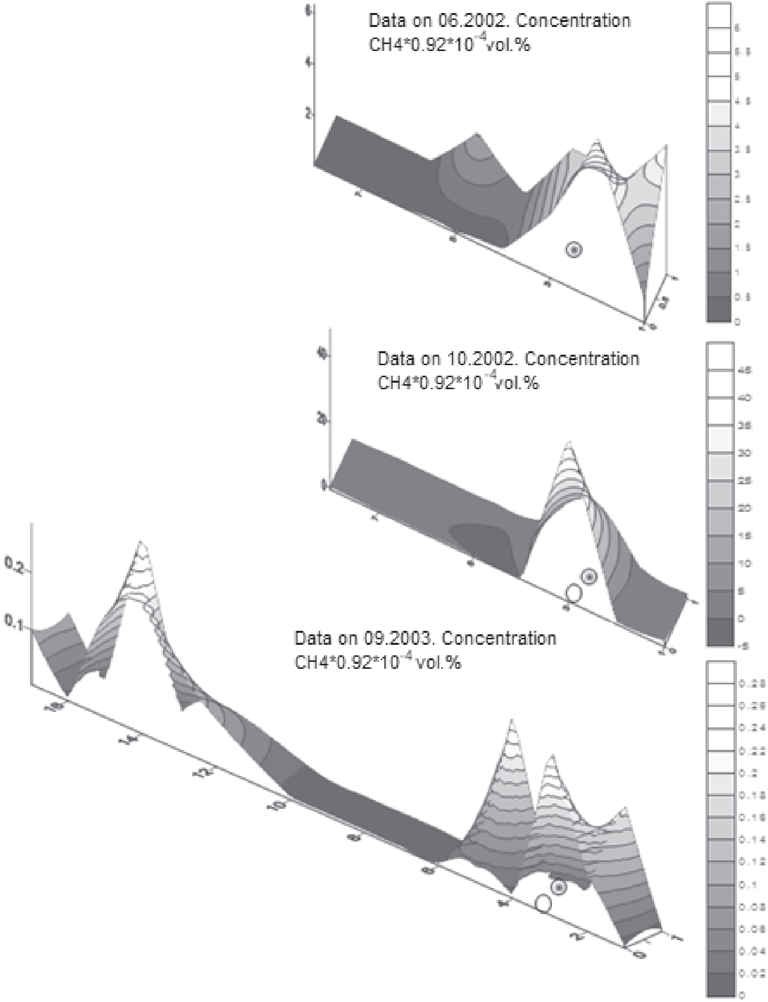

Figure 3.3.4: Dynamics of the soil methane volumetric concentration according to observations in linear profiles 0 and 1 during relief activities, Figure 1.3.1: o—relief well #2; ◉—relief well #1.

An artificial methane anomaly is also present at the traverse of a booster compressor station—point 3. Here, the methane concentration increases due to man-made seismicity.

The first cycle of atmospheric-electrical and hydrogen-radon measurements at the site of the North Stavropol Gas Storage Facility was carried out in October 2001 at the Pelagiadian structure. Here, at 43 Klubnichnaya Street, Pelagiada Farm, an emergency gas outbreak occurred; see Figure 1.3.1 [34].

In 2001, the method for estimating soil methane content based on observations of hydrogen, radon, and elements of surface atmospheric electricity had not yet been developed. The working formula (3.3.1) allowed us to retroactively evaluate the soil methane content dynamics over three consecutive observation cycles.

In addition to the profile of the annulus, two linear profiles, 0 and 1, were set around the failing building. The first series of atmospheric-electrical and gas measurements was carried out in June 2002. By that time, discharge well #1 had already been drilled. Information about its depth is not available. Nevertheless, based on the location of the peaks in the concentration of soil methane (the graph for June 2002, Figure 3.3.4), one can confidently assume that it is a few meters. A collecting bell of 1.5 m in diameter was put on the wellbore.

Three months after the commissioning of the deep relief well #2, the pattern of methane distribution had changed dramatically, as presented in the graph for October 2002 (Figure 3.3.4). High peak values of soil methane content, at about 42×10^{-4} vol.%, were observed only in the vicinity of the wellbore. Such high values resulted from a depression crater in the collector area of the well, which slowed down the air-earth air exchange at the wellhead and promoted gas accumulation in the surface soil layers.

Finally, 11 months after the operational start of the second discharge well, the relief process could be considered complete. Even the peak values of soil methane content were lower than the background values at 0.8×10^{-4} vol.%. There was a surge in the soil methane content at picket 14, at a distance comparable to the depth of the second discharge well. Most likely, sub-vertical gas permeability in the area of picket 14 was comparable to the area of the sub-horizontal gas line to discharge well #2.

In Figure 1.2.8, 16 pairs of points obtained by laboratory analysis of samples 53–68, from the Kasimov Gas Storage Facility, are presented. Changes in soil methane concentrations at these pickets fell within the range 10^{-3} vol.% to 10^{-2} vol.%. The criteria for choosing pickets when sampling soil air for subsequent laboratory analysis were the maximum and minimum ratios of soil radon volumetric activity to atmospheric radon. Repeat sampling of radon was done. Correlation analysis of the measured, Rn(a), and calculated, $Rn(a)_{calc} = f(Rn)$, allowed the establishment of the degree of participation of volatile gases in ionizer transfer: 48 % of radon was transported by hydrogen and 52 % by methane. By analogy with the expression in (3.3.1), a similar working formula was introduced for the high concentrations of methane recorded [6, 34, 37].

$$CH_4 = [0.020436 \times Rn(a) + 0.0004]/Rn \ [\text{vol.\%}], \qquad (3.3.3)$$

where oil and atmospheric radon volumetric activity values are dimensionless and normalized to 1 Bq/l. The relative error of the expression (3.3.3) is $\Delta CH_4/CH_4(ave) = 14$ %. In the surveyed area, with the soil methane concentration of (10^{-3}–10^{-2}) vol.%, at 28 control pickets, 26 calculated concentration values were within 14 % of the variance of the laboratory test results. Therefore, an increase in the concentration of ionizing carrier gases in the surface atmosphere can be seen to lead to an increase in the accuracy of indirect determination of soil methane content.

3.4. References to Chapter 3

1. Shuleikin, V.N. Atmospheric-electrical and gas fields above fault zones, *Proc. Third Tectonic Physical Conference "Tectonophysics and Actual Problems of the Earth Sciences,"* 2012, **2**, 477-480. [in Russian]
2. Shuleikin, V.N. Atmospheric-electrical monitoring of geological heterogeneities and geodynamic processes in the Earth, *Proceedings of VIII Science and Technology Conference "Systems for Observation, Monitoring and Remote Probing of the Earth,"* Divnomorskoe, 2012, 271-274. [in Russian]
3. Imyanitov, I.M., and Shifrin, K.S. The current status of research of atmospheric electricity, *Uspekhi Fizicheskikh Nauk*, 1962, **4**, 593-642. [in Russian]
4. *The Guide for Surface Observations of Atmospheric Electricity Elements*, Leningrad, Izdatelstvo GGO im. A.I. Voeykova, 1960, 95p. [in Russian]
5. Semenov, K.A. Good Weather and Atmospheric Electricity Elements, *Proc. GGO im. A.I. Voeykova*, 1982, **455**, 112-119. [in Russian]
6. Shuleikin, V.N., Shchukin, G.G., and Kupovykh, G.V. *Development of Methods and Means in Applied Geophysics: Atmospheric-Electrical Monitoring of Geological Heterogeneities and Geodynamic Process Zones*, Saint. Petersburg. Publ. TsOP RGGMU, 2015, 206p. [in Russian]
7. Shuleikin, V.N. *The Earth and Atmospheric Electricity*, New York. Nova Science Publishers, 2018, 143p.
8. Voitov, G.I., Rudakov, V.P., Shuleikin, V.N., Kozlova, N.S., and Baranova, L.V. Emanation and electric effects in the subsoil atmosphere above the Kaluga Ring Structure, *Russian Journal of Sciences of the Earth*, 1999, **1**(6), 503-510.
9. Kozlova, N.S., Rudakov, V.P., Shuleikin, V.N., Voitov, G.I., and Baranova, L.V. Emanation and electric effects in the subsoil atmosphere above the Kaluga Impact Ring Structure, *Russian Journal of Sciences of the Earth*, 1999, **1**(6), 503-510.
10. Voitov, G.I., Nikolaev, I.N., Utochkin, Yu.A. *et. al.* About hydrogen flow to the surface atmosphere in geodynamically different geostructural Earth zones. *DAN*, 1995, **344**, 110-114. [in Russian]
11. Voitov, G.I., Gusev, A.S., Shuleikin, V.N. *et al.* Emanation (hydrogen-radon) and electric effects above complex tectonic structures (on the example of the Alexandrovskaya Zone of pre-

fault elevations, Belarus), *DAN RAN*, 2000, **370**(1), 105-108. [in Russian]

12. A set of geophysical methods for studying karst, *Recommendations on the Study of Karst by Geophysical Methods,* Moscow, Stroiizdat, 1986, 189p. [in Russian]
13. Kochev, A.D., Chertkov, L.G., Zaionts, I.L., and Afonasiev, V.Yu. The technique and results of comprehensive studies of karst-suffusion processes in Moscow, *Engineering Geology*, 1989, **6**. [in Russian]
14. Shuleikin, V.N. The features of polar conductivity redistribution for soil air around long induced disturbances of the Earth's crust, *Thes. III Sem. "Alternative Methods for Studying Heterogeneities of the Earth's Crust,"* Moscow, 1993, 86-87; 110, 172. [in Russian]
15. Shuleikin, V.N. Soil air polar conductivities observation results within boundaries of urban development, In Coll.: *Development of Methods and Means of Experimental Geophysics*, Moscow, 1996, **2**, 235-240. [in Russian]
16. Shuleikin, V.N., and Shchukin, G.G., Petrochenko V.M. Atmospheric-electrical survey of underground utilities, *Proc. A.F. Mozhaysky Military-Space Academy*, **653**, 126-132. [in Russian]
17. Mikhailovskaya, V.V. The instrument for measuring the electric field intensity, *Proc. A.I. Voeykov MGO*, 1977, **350**, 142-146. [in Russian]
18. Eryshev, A.P., Nikolaev, A.V., Urdukhanov, R.I., and Shuleikin, V.N. *The Results of Atmospheric-Electrical and Seismic Observations Above an Iron-Ore Deposit*, Moscow, Preprint #5, IFE AS USSR, 1987, 11p. [in Russian]
19. Nikolayev, A.V., Urdukhanov, R.I., and Shuleikin, V.N. Results of atmospheric electricity and seismic profiling of the ore-body, *Proc. 8-th Int. Conf. Atm. EI.*, Uppsala, 1988, 138-140. [in Russian]
20. Shuleikin, V.N. Delineation of the ore body zone according to spatial AEF variations, *Proc. IV All-Russian Symposium on Atmospheric Electricity*, Nalchik, 1990, 60-61. [in Russian]
21. Voitov, G.I., Starobinets, I.S., and Usmanov, R.I. About density of CH_4 flows to the atmosphere in oil and gas bearing regions (on the example of Amu-Darya Basin), *DAN SSSR*, 1990, **313**(6), 1444-1448. [in Russian]
22. Ammosov, S.M., Voitov, G.I., Korobeinik, G.S., Kuznetsov, V.V., Nikolaev, A.V., and Fedorova, G.S. On two types of gas-

geochemical effects in the seismic vibrator field, *DAN SSSR*, 1988, **301**(1), 62-68. [in Russian]

23. Shuleikin, V.N. Atmospheric electric field above hydrocarbon accumulations, *Proceedings of VII Russian Conference for the Atmospheric Electricity*, Saint-Petersburg, 2012, 271-273. [in Russian]
24. Gergedava, Sh.K., Buzinov, S.N., Shuleikin, V.N., Rudakov, V.P., and Voitov, G. I. Unconventional geophysics for underground gas storage facilities, *Oil, Gas, and Business*, 2001, **5**(43), 2-7. [in Russian]
25. Shuleikin, V.N. Atmospheric electric field above HC accumulations, *Georesources, Geoenergy, Geopolicy*, 2010, **2**. [in Russian]
26. Shuleikin, V.N. Atmospheric electric field—the indicator of HC accumulation plumes, *Georesources, Geoenergy, Geopolicy*, 2013, **1**(7). [in Russian]
27. Levashov, S.P., Yakimchuk, N.A., Korchagin, I.N., and Taskinbaev, K.M. Geoelectric surveys of oil-bearing salt-cap and subsalt deposits of the Karsak Dome (Western Kazakhstan), *Geoinformatics*, 2004, **3**, 28-32. [in Russian]
28. Ehhalt, D. H., The Atmosphere cycle of Methane, *Tellers*, 1974, **26**(1-2), 58-70.
29. Stauffer, B., Methane concentration in the glacial atmospheric was only half in the preindustrial Holocene, *Nature*, 1988, **332**(6167), 812-814.
30. Stauffer, B., Increase of the atmospheric methane recording in the Antarctic ice core, *Science*, 1985, **229**(4720), 1386-1388.
31. Alekseev, F.A., Voitov, G.I., Lebedev, V.S., and Nesmelova, Z.N. *Methane*, Moscow: Nedra, 1978, 310p. [in Russian]
32. Shuleikin, V.N. Non-contact method for monitoring GSF and gas wells sealing, *Oil & Gas Journal Russia*, 2012, **6**(61), 86-90. [in Russian]
33. Shuleikin, V.N., and Pshenitsyna, E.A. Methane distribution monitoring by the gas storage reservoir bed, *X-th International Conference on Geoinformatics—Theoretical and Applied Aspects*, Ukraine, Kyiv, 2011, A-65. [in Russian]
34. Zubarev, A.P., and Shuleikin, V.N. *Complex Geophysical and Geochemical Monitoring for Underground Gas Storage Facility Operation*, Moscow, Izd. Gasprom GSF OOO, 2009, 264p. [in Russian]
35. Shuleikin, V.N., Reznichenko, A.P., and Puschina, L.V. About relationships of soil air methane, hydrogen, and radon, *Proc.*

All-Russ. Conf. “Degasification of the Earth: Geodynamics, Geofluids, Oil, Gas, and Their Parageneses,” Moscow, 200, 544-546. [in Russian]

36. Shuleikin, V.N. Lecture on the Atmospheric-electrical sounding of inhomogeneities and dynamic processes in the geological environment, *The 4th All-Russian Scientific School and Conference “Radiophysical Methods in the Remote Sounding of Natural Media*,” Murom, 2009, 1-29. [in Russian]
37. Shuleikin, V.N. Operational control of methane above hydrocarbon accumulations, *Proc. Third Tectonic Physical Conference “Tectonophysics and Actual Problems of the Earth Sciences*,” 2012, **2**, 477-480. [in Russian]

CHAPTER 4

GEODYNAMIC PROCESSES AND SURFACE ATMOSPHERIC ELECTRICITY

Initial results on microseismic stimulation of soil-atmosphere air exchange were obtained at the Uznozh Test Site (Belarus). The comparison of soil air hydrogen and methane in samples taken before and after vibration showed increases in the concentration of volatile gases by some tens of percent. Continuous monitoring of the polar conductivity of air above a deep subway line showed that microvibrations of the ground caused by a train passing under the measuring device increased the signal from the aspiration condenser unit by 50–60 %. Micro-vibration of the earth at railway shunting tracks, on which the constant coupling of trains takes place, reduced the level of the atmospheric electric field by ~200 V/m compared to the background level of the field at a distance of ~500 m.

Minimum soil air exchange was observed above the depression funnel of the city water intake station where the peak values of the atmospheric electric field were ~400–900 V/m. The reverse process, the injection of fluid into the ground for hydraulic fracturing, led to a decline in the field, which reached negative values.

A comprehensive analysis of the annualized data set of observations of global oceanic microseisms of the North Atlantic region with periods of 4–9 s (Pulkovo Seismic Station); water levels in observation wells of the Leningrad region (with average levels of 6m, 30m, and 60m); and the atmospheric electric field (the Voeykovo Observatory) showed that average monthly measured and calculated (as functions of the water level and amplitudes of microseisms) field values correlated at the level of 0.72–0.78. Variations in the field saw changes in the water levels of wells. Finally, during periods of microseismic storms, when the amplitudes of oceanic microseisms increase to 4–6 μm, the field variations determined the microseisms.

The increase in levels of upper water and groundwater with a drop in atmospheric pressure during pre-storm periods leads to an increase in the exhalation of soil radon and a correlation with changes in the air-earth current and the atmospheric electric field.

4.1. Complex Hydrogen-Radon and Atmospheric-Electrical Observations of a Landslide

Primary gas pipelines from gas production sites to consumers, cross a significant number of slopes with unstable soil structures. The operational experience of pipeline transport shows that, despite ensuring the stability of slope areas, the construction of pipeline structures leads to a disruption of the natural equilibrium of soil masses. Pipeline construction is likely to involve the movement of large amounts of soil [1–3]. In the case of landslides, the impact of soil masses on a pipeline is inevitable and significantly complicates its safe operation. This increases the possibility of an emergency event occurring.

Landslides involve the sliding displacement of rock masses down a slope by the action of gravity. The masses of the rock that form the slopes become saturated with moisture and lose support as a result of being caved in by the action of water. The strength of a rock formations is weakened by: weathering; water logging from precipitation and groundwater; natural seismic effects; and construction or commercial activities carried out without due consideration of geological conditions.

For many decades, landslide stress-states have been investigated using geodetic surveys, seismic surveys, and geoelectric prospecting. Magnetic and high-precision gravimetric imaging has been less used [4–6]. Unfortunately, setting up such geophysical investigations is rather laborious. Let us consider the possibility of using a complex of atmospheric-electrical and hydrogen-radon observations to monitor the stress-state of a potential landslide.

A landslide’s length is much greater than its thickness [5, 7]. As a landslide moves, zones of increased fracture—zones of stretching and zones of compression—form in its body. These have a sub-vertical direction. Already at 30 % soil humidity, soil-atmosphere air exchange will occur exclusively through cracks, as the pore space becomes squeezed with water. Expansion zones redistribute the flow density of volatile gases, driving them from deep underground to the landslide body, where maximum soil-atmosphere gas exchange takes place. These features of a landslide suggest the possibility of monitoring its stress-state and dynamics using relative gas permeability, for which observational control measurements can be performed under natural conditions of occurrence in relative units [8–10]. For this purpose, it is sufficient to carry out operational measurements of any volatile gas in the soil and normalize the obtained values to the maximum recorded value of the selected parameter in the test area with a system of observation pickets. A single value can be observed at the landslide, where the tension at the time of observation is maximal. The minimum value can be found in the area of maximum compression.

Soil air hydrogen can be chosen as the measured gas, the rapid assessment of which is possible using measuring devices developed and manufactured for more than 20 years at the Moscow Engineering Physics Institute [11–13]. According to the model developed (see Section 1.2), hydrogen is a carrier gas of radon to the surface atmosphere. In the case of hydrogen and methane being exponentially interconnected (Figure 1.2.8), hydrogen can be considered to be the only carrier gas of the ionizer, and its density will partially determine the total polar conductivity of the surface air: λ.

Experimental verification of the proportionality of total polar conductivity in the redistribution of the soil-atmosphere air exchange over geological zones of compression and extension was carried out at a failing building, constructed in the 1930s on a bulk terrace of the left bank of the Moscow River. At the time the measurements were taken, a crack had formed in the middle of the building, which, according to seismic observations, continued to grow with up to two micro-earthquakes per hour.

During construction, the bulk terrace and the building were reinforced with buttresses: two buttresses were rigidly connected to the ends of the building; one buttress was located below the left wing of the building; and at the front of the facade of the right wing of the building a chapel built in the nineteenth century acted as a buttress (see Figure 4.1.1). Observation profiles were set: at the right end of the building, with pickets 1–4 above and picket 5 below the working buttress; pickets 6–8 and 9–11 were set below the non-working buttress.

Figure 4.1.2 shows the variations in relative gas permeability $G(\lambda)$ of the selected profiles. The buttress at the right end of the building was in working condition: picket 1 was compressed, and pickets 2–5 were extended.

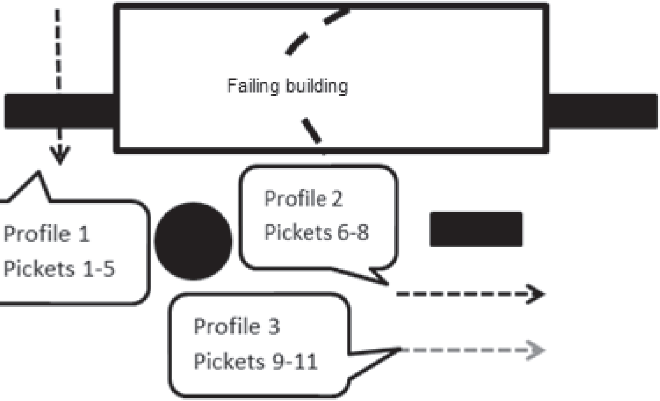

Figure 4.1.1: Plan of the failing building, buttresses, and observation profiles.

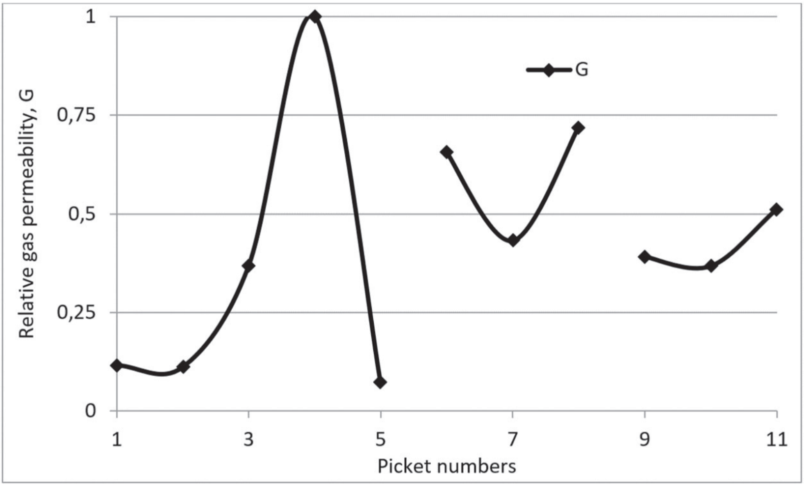

Figure 4.1.2: Relative gas permeability: at the working buttress, Profile 1, pickets 1–5; at the non-working buttress, Profile 2, pickets 6–8; Profile 3, pickets 9–11.

The ratio of relative gas permeability at the picket of maximum extension, picket 4, and the picket of maximum compression, picket 5, were $G(1)_4/G(1)_5 = 8.6$.

Due to the presence of an expanding crack in the failing building (tracked through seismic observations), the left half of the building, together with the bulk terrace, slid down the slope. Moreover, the reason for the movement of the left half of the bulk terrace was water leakage from the heating main. This leak provoked the left half of the bulk terrace to creep down the bank thanks to a clay aquiclude along which precipitation and meltwater flow to the Moscow River. The average values of the estimated parameter in profiles 2 and 3 $G(2)$, $G(3)$, are about equal to 0.5. In the framework of the scale (0–1) considered, this suggests that the soil is not stressed in the study area.

Research into a landslide near Ust-Nevinsky Farm (in the Stavropol Territory), the modern movements of which were provoked by the laying of a gas pipeline, allowed us to choose soil air hydrogen, H_2, as the primary control parameter. The array of hydrogen measurement data from the system of observation pickets was normalized to the maximum value of the monitored parameter for relative gas permeability, $G(H_2)$. A laboratory study of four soil air samples taken at a landslide showed an exponential relationship between hydrogen and methane (samples 69–72 in Figure 1.2.8).

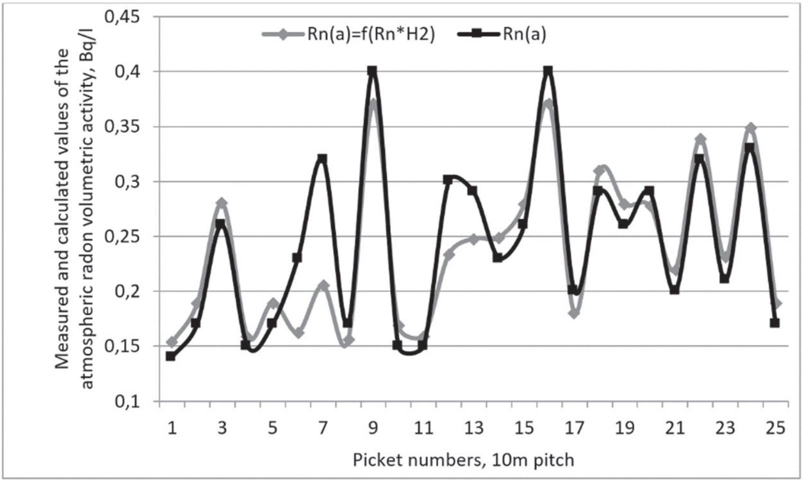

Figure 4.1.3: Measured, Rn(a), and calculated values of atmospheric radon volumetric activity, Rn(a) = $\boldsymbol{f}$(Rn×H_2).

To illustrate the validity of the assumptions made, Figure 4.1.3 presents the variations of the measured and calculated values of atmospheric radon volumetric activity obtained from the measurements along one of the profiles of the studied territory. The calculated values represent a linear approximation of the product of the soil radon volumetric activity and the soil hydrogen volume concentration. The reliability of this linear approximation is Rn(a) $= \boldsymbol{f}(\mathrm{Rn} \times \mathrm{H_2})$ equals $D = 0.86$.

This, in turn, allowed assessments considering hydrogen to be the sole carrier of soil radon, Rn, to the surface atmosphere. It follows that the volumetric activity of radon exhalation, Rn(a), in the atmosphere can be estimated through:

$$\mathrm{Rn}(a) = A_1 + B_1 \times \mathrm{Rn} \times \mathrm{H_2} \tag{4.1.1}$$

Within the framework of the proposed model, the total polar conductivity of air and AEF can similarly be presented as:

$$\lambda = A_2 + B_2 \times \mathrm{Rn} \times \mathrm{H_2} \tag{4.1.2}$$
$$1/E = A_3 + B_3 \times \mathrm{Rn} \times \mathrm{H_2} \tag{4.1.3}$$

From the expressions (4.1.1)–(4.1.3), it is possible to calculate expressions for hydrogen: $\mathrm{H_2}[\mathrm{Rn}; \mathrm{Rn}(a)]$, $\mathrm{H_2}(\lambda; \mathrm{Rn})$, and $\mathrm{H_2}(1/E; \mathrm{Rn})$. Using them, by normalization to maximum values, we can calculate values for relative permeability: $G[\mathrm{Rn}; \mathrm{Rn}(a)]$, $G(\lambda; \mathrm{Rn})$, and $G(1/E; \mathrm{Rn})$. When processing the observation results, the final value of relative gas permeability was obtained by averaging $G(\mathrm{H_2})$, $G[\mathrm{Rn}; \mathrm{Rn}(a)]$, $G(\lambda; \mathrm{Rn})$, and $G(1/E; \mathrm{Rn})$.

It is important to emphasize that for a single measurement cycle, 1 m^3 to 2 m^3 of atmospheric air is pumped through the aspiration capacitors of the polar conductivity sensor; the volume charge within a hemisphere of about 2 m in diameter in the dynamic capacitor, the AEF sensor, is used to record the local field. Therefore, the use of atmospheric electrical measurements significantly increases the representativeness of the final result. In the case of force-majeure circumstances, if it is impossible to obtain the measurement data of any parameter from the complex, or reject them, it is possible to achieve the desired result for the remaining observable characteristics.

Figure 4.1.4 shows the structure of the landslide slope, the observation pickets, and the profile locations, as well as their intersection by the gas pipeline.

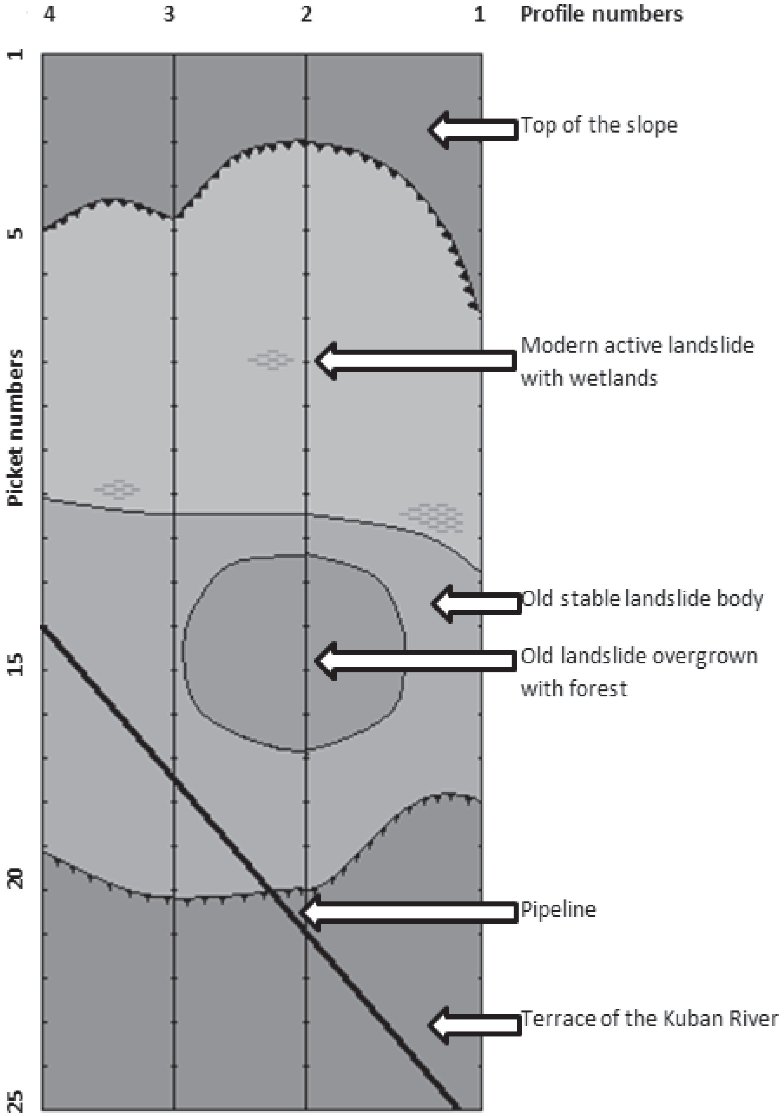

Figure 4.1.4: The structure of the landslide slope.

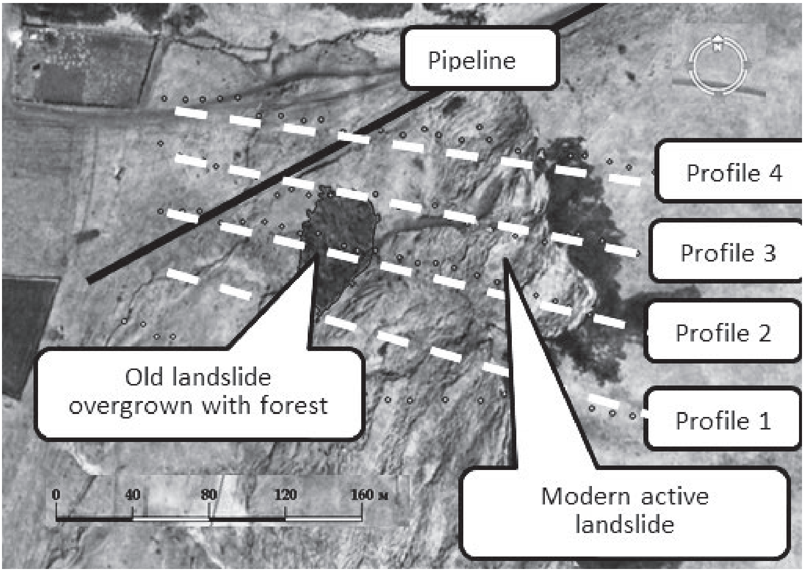

Figure 4.1.4 (continued): The structure of the landslide slope.

The difference in elevation between the margin of the separation niche and the foot of the landslide is about 30 m with a slope of 1/6. In the first quarter of its length, close to the separation niche, the thickness of landslide deposits smoothly increase from 4 m to 10 m down the slope; the slope of the landslide is negligible. Between the second and third quarters, the thickness of landslide deposits increase from 10 m to 24 m. At the same time, the slope of the surface increases sharply. In the lower quarter, the thickness of landslide deposits decreases from 24 m to zero. The main volume of landslide deposits is of eluvial-deluvial origin. In terms of their physical and mechanical properties, these deposits are related to the geotechnical elements $dpQ_{IV}(d)$ and dpQ_{IV}.

The geotechnical elements that form the main volume of the landslide body and the upper part of the root slope, and affect their gas permeability, are listed in Table 4.1.1.

As follows from Table 4.1.1, the root slope and the landslide body, which are composed of argillaceous rocks, have the same negligible gas permeability at about 10^{-3} millidarcys. Variations in the granulometric composition of the rocks of the study area in terms of gas permeability can be ignored.

Table 4.1.1. Properties of the landslide deposits and rocks of the upper part of the bedrock slopes

Geo-technical element	Moisture load	Density	Porosity	Moisture degree	Rock age, description, genesis
Landslide deposits	29	1.96	44.4	0.991	dpQ_{IV}(d) olive lumpy clay, a lot of multi-oriented slickenside panels, with land waste and sandstone wastes of deluvial genesis.
Landslide deposits	30.9	1.94	45.7	0.999	dpQ_{IV}(d-e) greenish-brown lumpy clay with fragments of stratification, with ferruginized sand interbeds and lenses, much gypsum, slickenside panels of deluvial-eluvial genesis.
Poorly defined formations, deposits that are not affected by modern landslide	27.12	2.01	42.5	1.000	dQ_{IV} greenish brown lumpy clay with land waste and sandstone wastes of deluvial genesis.

Table 4.1.1 (continued). Properties of the landslide deposits and rocks of the upper part of the bed-rock slopes

Geo-technical element	Moisture load	Density	Porosity	Moisture degree	Rock age, description, genesis
Poorly defined formations, deposits that are not affected by modern landslide	29.7	1.84	49.1	0.916	$e_{2\text{-}3}Q_{IV}$ an interbedding of dark brown, faulted laminated clay and ferruginized sand, gypsum inclusions of eluvial genesis.
Poorly defined formations, deposits that are not affected by modern landslide	29.8	1.92	45.6	0.948	$e_{3\text{-}4}Q_{IV}$ dark brown thin-laminated faulted clay, with sand additions and ferruginization spots, gypsum nests of eluvial genesis.

The porosity of landslide and eluvial-deluvial deposit samples showed similar values: 42 % to 49 %. The water saturation degree of landslide and eluvial-deluvial sediments was almost the same and the pore space of the landslide body was thoroughly tamped down.

The results of observations made of the landslide are described in detail in [14–17]. Recording of the relative gas permeability from cycle to cycle allowed us to introduce a new parameter into consideration, that of differential relative gas permeability. This characteristic allows the evaluation of changes in the landslide deformation state during the period between surveys. To illustrate the developed and implemented methods of observation, let us dwell on the variations of the differential relative gas permeability in profile 4, which crosses the gas pipeline at picket 14 (see Figure 4.1.5).

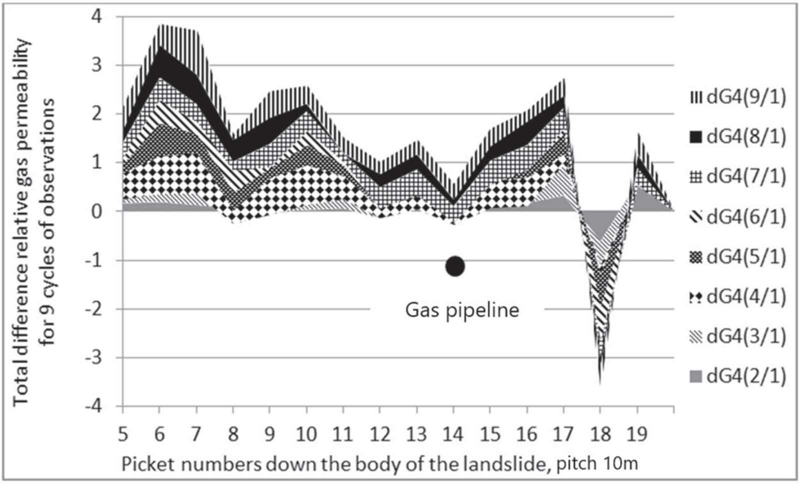

Figure 4.2.5: Dynamics of differential relative gas permeabilities for 9 observation cycles at profile 4.

The sum of differential relative permeability values at the level of the gas pipeline varied around zero. This means that over the entire measurement period, the stress-state of the landslide body did not change. At pickets 14–17, a steady extension was observed. Most likely this is due to the removal of moisture through the drainage system of the gas pipeline.

Nine cycles of hydrogen-radon and atmospheric-electrical observations of the landslide slope stress-state dynamics proved the efficiency of the technique developed. Let us consider the possibility of improving its accuracy in determining the control parameter—relative gas permeability.

In the course of implementing these experimental observations, the method was improved from cycle to cycle. Let us take the results from measurements of the last cycle of observations when the method had been worked out completely. Table 4.1.2 presents the correlation coefficients between Rn(a), l, and the product of $Rn \times H_2$; the inverse AEF value, $1/E$, Rn(a); and the product of $Rn \times H_2$ at four observation profiles. The last column shows the number of observation pickets directly on the landslide body (see Figure 4.1.4).

The lowest correlation coefficient was recorded for profile 2, between the product of $Rn \times H_2$ and the inverse field value, $1/E$. There may be two reasons for this. Four profile pickets were set up on the old landslide, which was overgrown with forest, and so the field was shielded and, accordingly, was not observed. Three pickets located above the young landslide, were set up on a marshy area, where radon could be transferred by methane of biogenic origin.

Table 4.1.2. Checking the relationship of gas and electrical characteristics at the landslide body (9th cycle of observation)

	$k[Rn(a);Rn\times H_2]$	$k[Rn(a);1/E]$	$k[Rn\times H_2;1/E]$	$k[Rn(a);\lambda\ ]$	Profile length on the landslide body
Profile 1	0.73	0.74	1.00	0.83	12 pickets
Profile 2	0.7	0.72	0.54	0.75	18 pickets
Profile 3	0.86	0.76	0.82	0.92	16 pickets
Profile 4	0.95	0.8	0.74	0.95	15 pickets

Taking into account the actual errors of the measuring equipment (see Section 1.1) and the accuracy of currently existing measuring devices, let us estimate errors in the calculation of the relative gas permeability according to the technique developed. Recording of hydrogen in the surface layers of the soil was carried out simultaneously using two sensors: VSG-01, (see Section 1.1) [12, 13]. The developer certified the measuring devices before we left for fieldwork; the relative error of a single sample at each sensor was 10 %, or 7 % after averaging the results. The measurement error of the concentration of the sample for hydrogen can be estimated by the value of $\Delta G(H_2) = \Delta H_2 \times dG(H_2)/dH_2 = \Delta H_2/H_{2max}$. A transition to a relative error in estimating relative gas permeability as a function of soil air hydrogen gave a value of 7 %, as a relative error in measuring hydrogen.

The resulting relative error of the instruments in the estimation of relative gas permeability, $G(H_2)$, is satisfactory for geophysical measurements. However, the existence of daily variation in the controlled parameter should also be noted. For eight hours of operation, this was about 10 %. Taking into account the daily variation of soil hydrogen concentration, the total relative error of the estimate $G(H_2)$ gives us a rough figure of 12 %.

At the next stage of analysis, we considered the errors in estimating relative gas permeabilities using the proposed model of the relationships between gas and electrical parameters in the Earth and the atmosphere. The relationships between atmospheric radon, $\mathrm{Rn}(a)$; polar conductivity, λ; the inverse field value, $1/E$; and the product of $\mathrm{Rn} \times H_2$—expressions (4.1.1-4.1.3)—were introduced. From this, we have:

$$H_2 = [\mathrm{Rn}(a) - A_1]/(B_1 \times \mathrm{Rn}) \quad (4.1.4)$$
$$H_2 = (1/E - A_2)/(B_2 \times \mathrm{Rn}) \quad (4.1.5)$$
$$H_2 = (\lambda - A_3)/(B_3 \times \mathrm{Rn}) \quad (4.1.6)$$

It should be noted that the considered expressions include the ratio of pairs of measured interconnected parameters. This means that when they are recorded simultaneously, errors associated with the daily variation are minimized.

As noted in Section 1.1, in nine working cycles on the landslide, the radon volumetric activity sensor RGA-01 was used to record the soil and atmospheric radon. After averaging 2–4 air samples, the relative measurement error of radon was equal to about 17 %. Modern scintillation radon sensors (Cedar MR-106N, PPA-01M-01) have a similar measurement accuracy.

Genitron Instruments GmbH has built an AlphaGuard radon volumetric activity sensor, which uses a pulsed ionization chamber as a detector. The relative error of this measuring device is reduced to 5 % [18, 19]. The calculation errors of relative gas permeabilities $G[\mathrm{Rn}(a)]$, $G(\lambda)$, and $G[(1/E)]$ can be composed from two terms $\{[\Delta \mathrm{Rn}_k \times dG_i/d\mathrm{Rn}_k]^2 + [\Delta X_k \times dG_i/dX_k]^2\}^{1/2}$, where $k = 1, 2, 3$; and $X_k = \mathrm{Rn}(a), \lambda, (1/E)$. Figure 4.1.6 gives the relative values of these errors calculated from the instrumental errors of the measuring equipment used. The histograms show that the highest errors—from 22 % to 35 %—occurred in calculations of relative gas permeability as a function of soil and atmospheric radon. The reason for such a high error is obvious—it is the error in recording radon using the RGA-01 radon scintillation sensor.

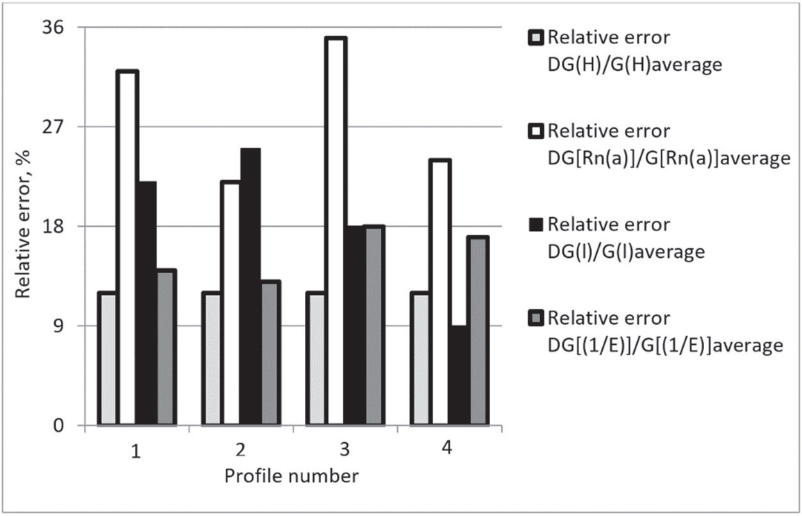

Figure 4.1.6: The values of relative permeability errors calculated from the instrument errors of the measuring equipment used.

Figure 4.1.7 presents similar calculations for the use of the AlphaGuard radon activity sensor, which has a relative error of 5 % [18, 19].

When using the AlphaGuard sensor, the maximum error of the results should be expected when using data from measurements of polar conductivities in the atmospheric air.

A single observational cycle on the landslide at Ust-Nevinsky Farm took about 4–5 days. On the first day, the location of measurement points was checked and under fair weather conditions, a survey of 100 observation pickets took only 3.5 to 4 days.

The work, using 100 observation pickets, was carried out exclusively to test and illustrate the capabilities of the integrated gas and atmospheric-electrical measurement technology, while monitoring the dynamics of the stress-state of the landslide. To solve the problem of changing the load of a landslide sliding down onto the pipeline, it was enough to check 2–3 dozen pickets along 2 or 3 short profiles at the pipeline crossings and in areas of protrusion.

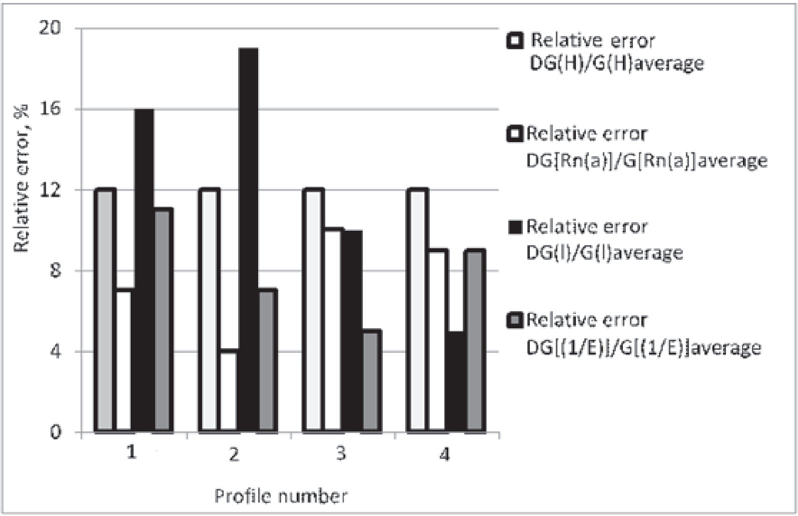

Figure 4.1.7: The values of relative permeability errors calculated using the AlphaGuard volumetric radon activity sensor.

To simplify the repeated polling of the surveyed landslide after the selection of short profiles with the observation pickets, collection bells needed to be installed at a depth of 1 m, with hoses from them to the surface. This makes it easier to find the measurement points during the next series of checks, and makes the gas observation procedure easier in any weather conditions; atmospheric-electrical observations, in turn, can be carried out with a very short time interval in stable meteorological conditions.

The effect of deformation processes on the soil-atmosphere air exchange and the elements of surface atmospheric electricity is rather small in scale. The controlled parameters vary by less than an order of magnitude and the areas covered by these changes do not exceed tens of square meters. Even if we turn to landslides of more than a kilometer in size, the area of change increases, at most, by a single order of magnitude. All this suggests that changes in the stress-state of landslides only have a local effect on gas and atmospheric-electrical parameters.

The largest scale changes in soil-atmosphere air exchange and surface atmospheric electricity are to be expected in fault zones, particularly in terms of precursors to a seismic event. As suggested in the review given in Section 1.1, observations of AEF before earthquakes provided recorded field values of about 1,000 V/m. At the same time, the areas covered by such changes can be measured in tens of square kilometers.

In the early twentieth century, fieldwork carried out by the French geologist A. Schlumberger in the Alps and the Russian geologists I.V. Mushketov and D.I. Mushketov in Central Asia, highlighted an undefinable phenomenon. Above the fault zones of the Earth's crust, motionless formations of clouds could be observed [20]. In the second half of the twentieth century, with the beginning of the era of space geology, the contours of clouds on images of the Earth taken from space turned out to be sufficiently pronounced to be used for mapping faults along the shelf zones of continents [21]. Images with cloud ridges were used to search for oil and gas regions in the Middle Volga and the Mangyshlak Peninsula in the Caspian Sea [22]. Analysis of satellite images indicated that the length of such linear clouds could reach several hundred and even thousands of kilometers. Such clouds lasted from several minutes to several hours, or even days. According to [23], the cause of this phenomenon lies in the influence of a fault on the atmosphere during times of tectonic activity. Similar cloud anomalies have a lithospheric origin and their occurrence serves to signal the onset of geodynamic processes.

We evaluated the formation of clouds that were not dissipated by the prevailing winds in Central Asia; the atmosphere was relatively stable and with a weak haze, which is known as the Afghan. The aerosol formations that compose this haze are suspended by heat flows ascending from the ground. The diameters of particles forming these aerosol formations range from tenths of microns to microns.

Above the fault zone, which undergoes compression prior to an earthquake, the exhalation of soil radon leads to high positive fields. Charges of aerosol particles have different signs. Under normal conditions, these may fall within the range 10 e to 100 e (where e is the electron charge). As a result of friction and, primarily, the action of the electric field, the charge of these particles can increase to 10^7 e. Using these estimates, let us examine three cases of drop charges, q: 10 e, 100 e, and 1,000 e.

The occurrence of the Afghan in a region with high positive fields leads to a separation of charges of different signs: negatively charged particles are deposited on the ground and positively charged particles, due to the introduction of an electric force $F = E \times q$, float in the positive field, hanging at a height at which the weight of droplets is compensated by heat fluxes and the electric force. As aerosol particles accumulate in this “hanging” zone, they take the form of a stagnant cloud formation.

In Table 4.1.3, assuming they have a spherical shape, the weight of the droplets are calculated as being in the range of diameter of 0.5 to 2.0 μm. The last three columns present the ratio of the electric force acting on the droplet to its weight.

Table 4.1.3. The ratio of electrical force and the weight of droplets

The diameter of drops, micron	Drop weight, N		The ratio of electric force to drop weight		
		Charge drops	10*e*	100*e*	1,000*e*
0.5	6.41E-16		2.50E+00	2.50E+01	2.50E+02
1.0	5.13E-15		3.12E-01	3.12E+00	3.12E+01
1.5	1.73E-14		**9.25E-02**	9.25E-01	9.25E+00
2.0	4.11E-14		**3.89E-02**	3.89E-01	3.89E+00

In recent decades, based on the analysis of numerous satellite images of linear cloud formations, the concept of detecting a complex of anomalous variations of geophysical fields in the area before a seismic event has been developed. The concept is based on the results of multi-parameter measurements within the framework of a synergistic approach to complex open dissipative systems [24–27].

The most straightforward estimate of the occurrence of stagnant cloud formations above a fault zone during the period before an earthquake was not constructed to illustrate the forecast cloud conditions. The purpose of this assessment is to demonstrate the effect of the classical electrode effect on the redistribution of charged aerosol formations present in the atmosphere.

4.2. Experimental Verification of the Causal Relationships between the Microseismic, Hydrogeological, and Atmospheric-Electrical Fields

The proposal on the existence of a causal relationship at the level of microseisms with local variations of hydrogeological and atmospheric electrical parameters required direct verification. Testing of this was performed using experimental data from the period 1984–1986 that had been obtained independently at three different locations: the Pulkovo Seismic Station, which gave data on North Atlantic microseisms of periods lasting 4–9 s [28]; A. I. Voeykov MGO, which gave data on regimented observations of the atmospheric electric field around the Observatory of Voeykovo village (Leningrad Region) [29]; and the North-West Department of Geology provided data on water level variations in observation wells for aquifers at depths of 6 m, 30 m, and 60 m relative to the ground surface. The experts of the North-West Department of Geology selected three wells in Leningrad and the Leningrad Region (Nos. 14, 371, & 2331), where economic activity had minimal impact on the water level.

At the first stage of analysis, we considered the correlation coefficients of monthly mean AEF values, E; water levels in observation wells $z1$–$z3$; and the level of global oceanic microseisms in the North Atlantic, A: $k(z1; E) = 0.72$; $k(z2; E) = 0.27$, $k(z3; E) = 0.41$, $k(A; E) = 0.11$. Despite low correlation coefficients, we constructed a linear equation of the relationships between the considered parameters:

$$k[E; E(z1, z2, z3, A)] = 185.6 - 381.3z1 + 70.3z2 + \\ + 11.2z3 - 7.94A, \qquad (4.2.1)$$

where numerical coefficients have the dimension of [V/m]; the measured water levels ($z1$, $z2$, $z3$) are normalized to 1 m; and the microseism amplitudes (A) are normalized to 1 μm [30–32]. Figure 4.2.1 shows the monthly variations of the measured and calculated characteristics for 1984.

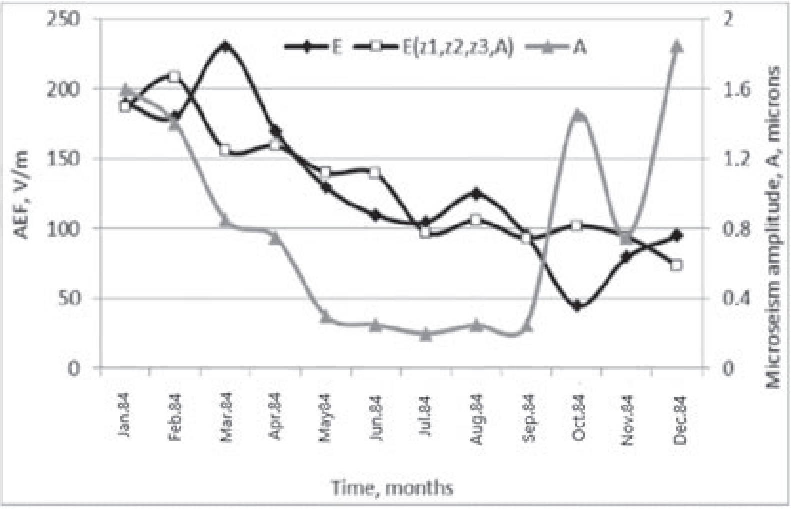

Figure 4.2.1: Average monthly measured AEF, *E*; estimated values of *E*(z1, z2, z3, *A*); and average monthly amplitudes of the global oceanic microseisms of the North Atlantic, *A*, for 1984.

The correlation coefficient between the measured and calculated AEF values was equal to $k[E; E(z1, z2, z3, A)] = 0.79$; between the calculated field values and the amplitude of the global microseisms the coefficient was $k[E(z1, z2, z3, A); A] = 0.22$. However, if we exclude the results of observations for three months—March, October, and December—the correlation coefficient with the amplitude of global microseisms for nine months sharply increases to $k[E(z1, z2, z3, A); A]_9 = 0.80$. The same happens with the correlation coefficient for 10 months between the measured and calculated field values, if we exclude from consideration the values for March and October, $k[E(z1, z2, z3, A); A]_{10} = 0.92$.

Returning to the expression (4.2.1), let us consider the sequential influence on the correlation coefficient between the measured and calculated AEF values when sequentially entering *z*1, (*z*1, *z*2), (*z*1, *z*2, *z*3), and (*z*1, *z*2, *z*3, *A*) into the working formula (Figure 4.2.2).

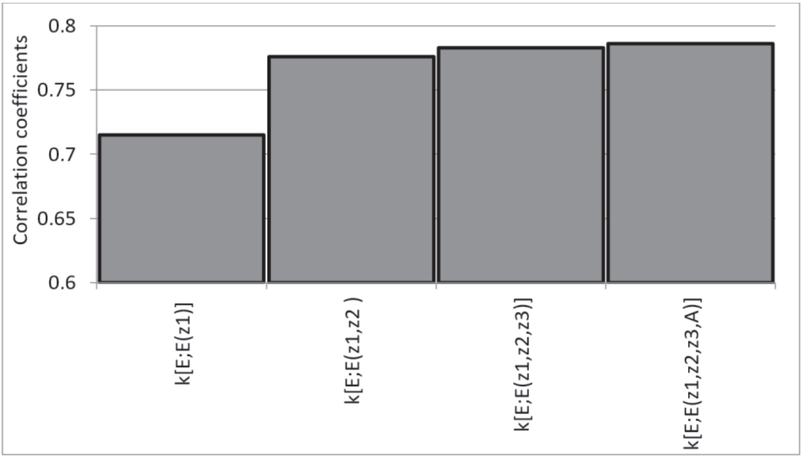

Figure 4.2.2: The correlation coefficients between the measured and calculated AEF values, depending on the arguments considered, are $z1$, ($z1$, $z2$), ($z1$, $z2$, $z3$), and ($z1$, $z2$, $z3$, A).

At first glance, variations in the field appear to be mostly affected by variations in the leakage water, $z1$, and the aquifer, $z2$. However, this is not the case, as can be seen from a consideration of AEF variations during the periods of microseismic storms in the North Atlantic (Figure 4.2.3).

The graphs in Figure 4.2.3 show that in periods of microseismic storms, when the amplitudes of oscillations reach a maximum of $A = 4–6$ µm, they determine the powerful exhalation of radon, leading to a reverse electrode effect (see Section 2.3). Here, the correlation coefficients of the measured and calculated field variations are equal to: $k[E; E(A)]_{3\text{-}10.02} = 0.70$; $k[E; E(A)]_{27.02\text{-}4.03} = 0.84$.

The influence of man-made microseismic oscillations in the ground on the electrical characteristics of the surface atmosphere has already been considered in Chapter 3: Figure 3.1.8 shows an increase in the polar conductivities of the air when a subway train passes under the measuring device; Figure 3.2.3 illustrates these changes indirectly in the increase of soil methane concentration above an oil reservoir exposed to vibration. Let us consider the results of changes in AEF in a profile in an area where railway shunting takes place and trains are constantly being coupled.

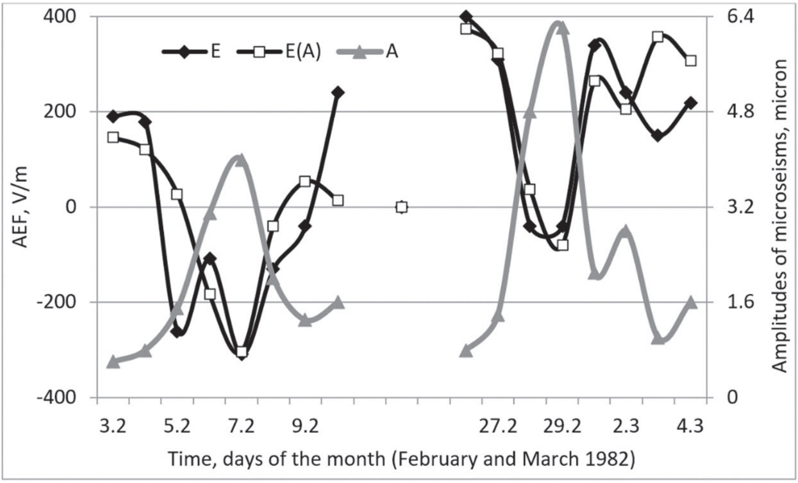

Figure 4.2.3: Changes in measured and calculated AEF variations and amplitudes of global microseisms during periods of microseismic storms.

The measurements were carried out under extremely adverse weather conditions: air temperature at -12 °C to -15 °C and snow cover of 5 to 7 cm. Figure 4.2.4 shows the AEF variations when passing along the profile away from the railroad and towards the railroad [14, 17, 32].

In the time intervals of 1 to 6 minutes and 24 to 29 minutes, Figure 4.2.4 shows the AEF background changing over time at the railway, while vehicles are standing still.

Temporal background field variations near the railroad are comparable to the time intervals of the profile measurements; they are quite stable in duration and fit the limits of (250–350) V/m. In the time interval of 7–13 minutes, spatial changes of the field in the profile from the railroad can be seen—the AEF grows by ~200 V/m. In the time interval of 17–23 minutes, the field decreases from 497 V/m to 243 V/m, when returning from the turning point to the railroad.

Low AEF values at the railroad and subsequent increase of the field by 150 to 200 V/m while moving along the profile, can be confidently associated with a high level of man-made seismic noise due to the maneuvering of rolling stock. At the beginning of the profile, 10 m from the railroad at the location of background AEF recording, microvibrations caused “by feet” were perceived, i.e., their amplitudes were at least hundreds of microns.

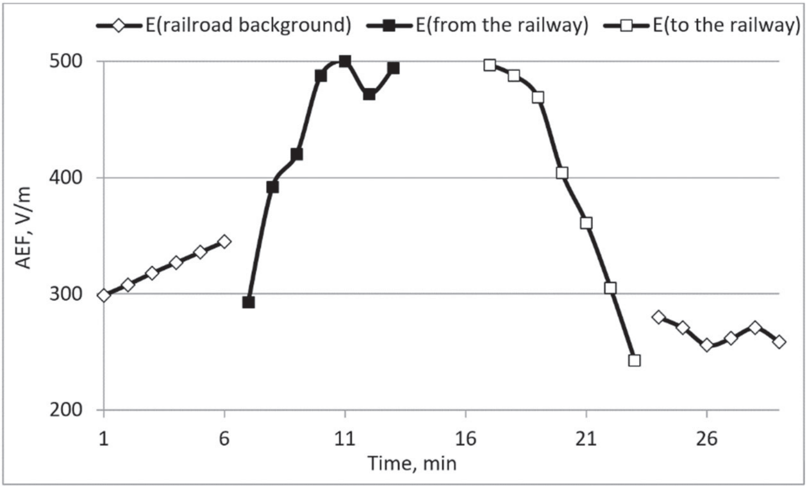

Figure 4.2.4: AEF variations when passing along the profile from the shunting railroad and back.

In the examples given of the relationships between microseismic vibrations and the elements of surface atmospheric electricity, the level of microseisms was very high. During the making of observations, similar relationships at a very low level of vibrations of long duration were successfully recorded [33, 34].

The work was carried out in July 2003 at the site of the Kasimov Gas Storage Facility, where the injection cycle had already been taking place for three months. The source of seismic noise was a booster compressor station that, for decades, had been pumping combustible gas into a reservoir bed. The measurements were carried out on two profiles, the mid-points of which were located at a distance of 3–4 km and about 1 km from the compressor station. To minimize the effect of random sources of microvibration, seismic measurements were performed for three days in the evening and at night, from 10 p.m. to 2 a.m. The registered speeds of microvibrations were very low: $v_1 \sim 10^{-7}$ m/s and $v_2 \sim 10^{-8}$ m/s.

During data processing, the frequency range of the seismic receivers was divided into several sub-bands: 10 to 20 Hz; 20 to 40 Hz; 40 to 80 Hz; 80 to 160 Hz; 160 to 320 Hz; and 10 to 394 Hz.

The correlation coefficient of the total velocity in the selected ranges and AEF is shown in Figure 4.2.5.

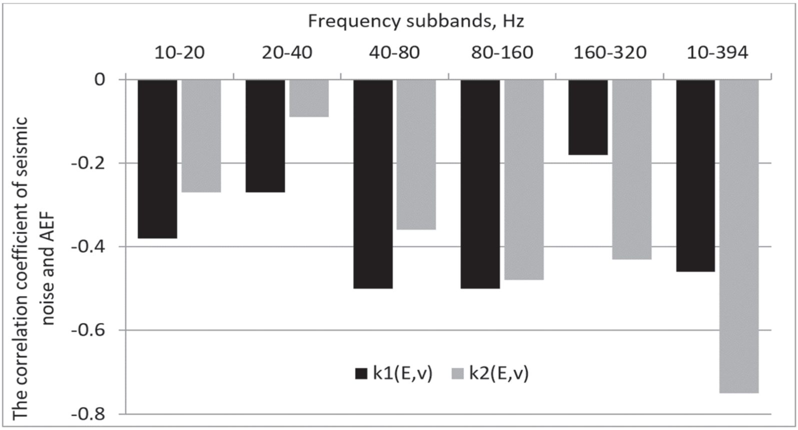

Figure 4.2.5: Correlation coefficients of AEF and seismic noise, $k_1(E, v)$ and $k2(E, v)$, on profiles 1 and 2.

Significant correlation coefficients were successfully obtained for the full velocity vector of microvibrations in the range of 10 to 397 Hz: $k_1(E, v)_{10\text{-}397} = -0.46$, $k_2(E, v)_{10\text{-}397} = -0.75$; in the sub-range of frequencies of 40 to 80 Hz: $k_1(E, v)_{40\text{-}80} = -0.46$; in the sub-range of frequencies of 80 to 160 Hz: $k_1(E, v)_{80\text{-}160} = -0.50$, $k(E, v))_{80\text{-}160} = -0.48$. The results show that the relationship observed between ground microvibration and AEF variations may result from a long-term accumulation of seismic energy in the geological environment.

Figures 4.2.1 and 4.2.2 show the relationship between AEF and the dynamics of aquifers. Let us give another example of the hydrogeological regulation of the field. Figure 4.2.6 shows the repeated AEF-profiling over the depressed funnel of the urban water intake (Svetlogorsk, Belarus) [14, 32, 35–37].

The measurements were performed using a stationary and a mobile field mill Pole-2. A stationary sensor was continuously operated at the Uznozh Test Site; the mobile one was used to measure AEF on the Uznozh-Svetlogorsk highway. The background level of the field at the test site at the time of the profile measurements varied from 90 V/m to 110 V/m at pickets 28 and 29. The peak AEF values at the fifth picket (with the traverse of the water intake station) varied at the levels of 400 V/m, 900 V/m, and

600 V/m. The conical depression minimized the soil-atmosphere air exchange reducing soil radon exhalation and leading to high values of the recorded field.

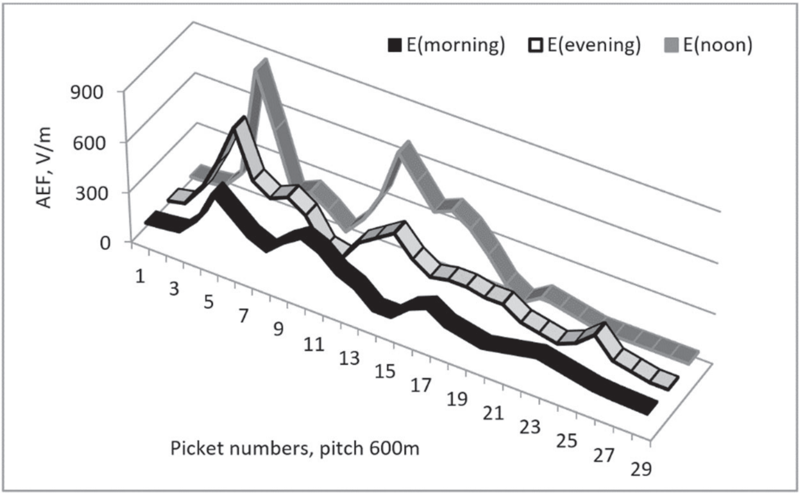

Figure 4.2.6: Spatial variations of AEF by the Uznozh-Svetlogorsk highway over the zone of the urban water intake.

Let us now turn to the results of observations of variations in the atmospheric electric field during the reverse procedure, i.e., when fluid is pumped into the ground [14, 32, 38]. Figure 4.2.7 shows temporary AEF variations recorded at the mouth of the injection well with a field mill Pole-2.

A sharp drop in the signal with a change in the field sign to values of about -140 V/m to -150 V/m around the twentieth minute after the beginning of fluid injection. This was due to a forceful local ejection of the ionizer at the moment of hydraulic fracture—the reverse electrode effect (Figure 2.3.2). The lifetime of the heavy ions, which primarily determine the local atmospheric electric field, was 40 to 50 minutes [39, 40]. The maximum concentration of heavy ions is reached precisely at the middle of their lifetime. A similar result is described in [41], where the reason for ionizer ejection was not a hydraulic fracture, but a sharp increase in the level of seismo-acoustic noise.

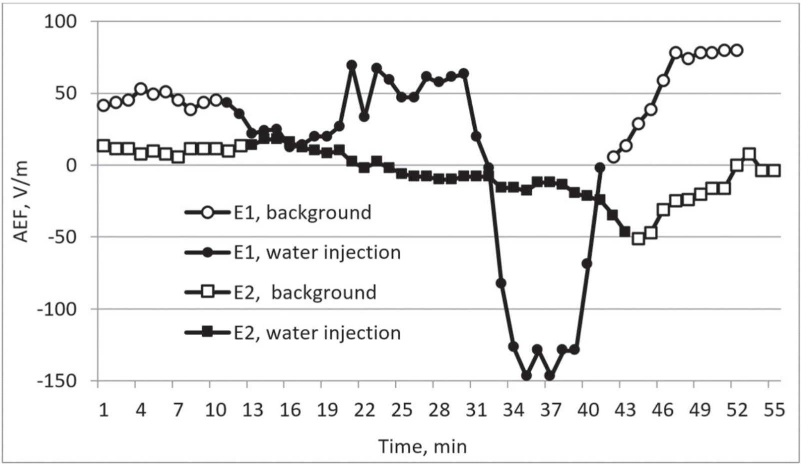

Figure 4.2.7: Variations of the atmospheric electric field during two cycles of injection of 30 m^3 of fluid into the ground to a depth of 50 m.

The experiment was performed in June 1988, at the end of the working day at the site of a station for the disposal of radioactive waste. Unfortunately, according to the working conditions at the site, the field mill could not be set up for continuous recording until the next day. The field recording in the morning of June 3—E_2, Figure 4.2.7—shows that 15 hours after the first injection, the background level fell to 10 V/m. That is, during this time, the pressure wave from the fracture zone led roughly to a fourfold increase in the concentration of the ionizer in the surface atmosphere.

Reinjection of 30 m^3 of water into the fracturing zone caused similar field variations at the mouth of the injection well, but, naturally, with lower amplitude differences. If during the first injection, the ratio of the minimum negative fields to the background before the cycle onset was equal to about -4; in the second case, it was equal to -4 to -5.

Unfortunately, due to the absence of a measuring device, it was not possible to monitor the background radiation at the observation site. Subsequent experience in Belarus in the summer of 1986, after the accident at the Chernobyl Nuclear Power Plant, showed that when caesium contaminates the field, a value of 30 V/m to 50 V/m corresponds to a radiation level of 50 μR/hour to 60 μR/hour. Close

E_1 fields were observed during the recording of the background before the onset of injection (see Figure 4.2.7).

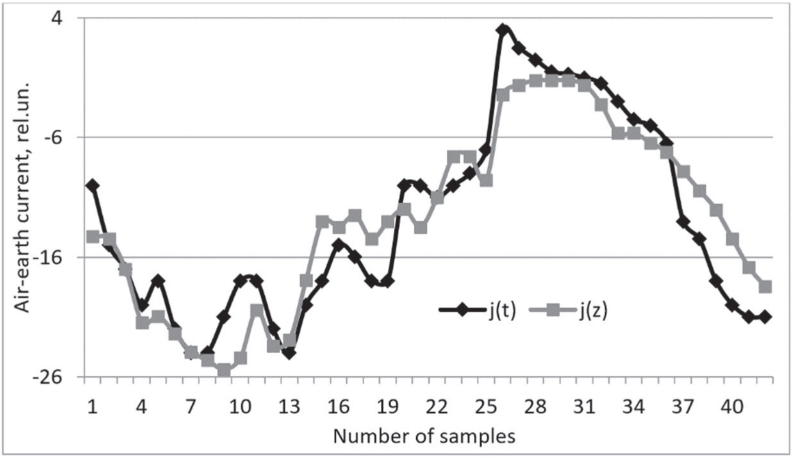

Figure 4.2.8: The measured *j*(*t*) and calculated *j*(*z*) air-earth current values as a function of variations in water level of the observation well z.

During work in May 1987 at the Uznozh Test Site in Belarus, with passing cumulonimbus cloud (in the absence of rain) and drizzle, exciting measurements were obtained for the AEF, the air-earth current, and the water level in the observation well opening the aquiclude. Figure 4.2.8 shows the measured air-earth current values, $j(t)$, and calculated current values as a function of variations in the water level of the observation well, $j(z)$, as the atmospheric pressure fell before a thunderstorm, and its variations during drizzle conditions.

In the first case, there was an increase in the water level of about 3 mm with passing cumulonimbus clouds; in the case of drizzle, variations in the level ranged from 0 mm to 3 mm. The coefficient of correlation between the measured and calculated values was $k[j(t), j(z)] = 0.92$.

Similar relationships were observed between the measured values of AEF and the calculated values of the field as a function of the water level in the observation well, in two separate data arrays, rather than on the whole data set—before a thunderstorm and during drizzle (Figure 4.2.9). The correlation coefficients between the measured and calculated curves were very large: $k = [E(t), E(z)]_{\text{thunderstorm}} = 0.98$; $k = [E(t), E(z)]_{\text{drizzle}} = 0.91$.

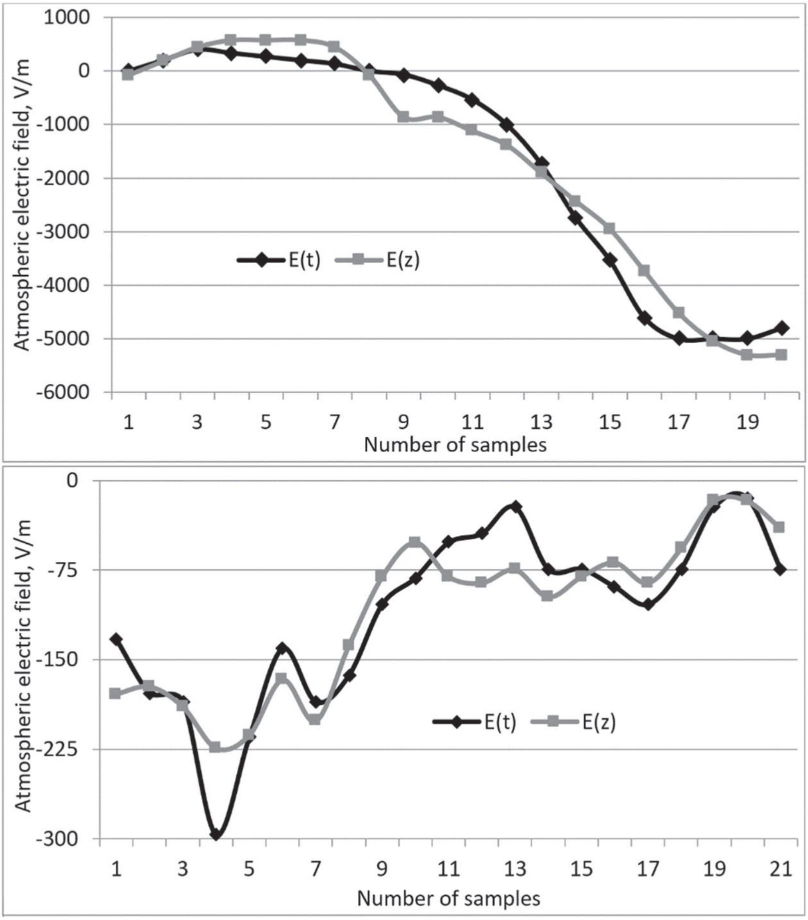

Figure 4.2.9: Measured $E(t)$ and calculated $E(z)$ values of AEF, as a function of water level variation in the observation well (z) before a thunderstorm and during drizzle.

The results obtained are clear. The air-earth current is considered to be the most stable atmospheric-electrical characteristic [39, 40]: $j = E \times \lambda$, where λ is the total polar conductivity of the air.

In the pre-storm period, with no precipitation or with drizzling rain, polar conductivities, λ, were obviously different.

A drop in atmospheric pressure accompanies the formation of cumulonimbus clouds. During drizzle, fluctuations in atmospheric pressure are possible. Under stable conditions, the weight of the air column keeps aquifers at a certain level, but a drop in atmospheric pressure leads to a rise in levels. The sensitivity of groundwater and perched water levels to a drop in atmospheric pressure is about 8 mm/hPa; in water-bearing formations isolated from the atmosphere, it is significantly less than 2 mm/hPa [42, 43].

In the examples considered, the dynamics of the air-atmosphere air exchange are associated with the dynamics of the groundwater level. In spring, the installation site of the measuring devices was flooded and the waterline in the nearby pond was about 0.8 m.

When the aquifer level rises from the pore space of the surface soil layers, the soil air, which consists of hydrogen, methane, and radon, is squeezed up into the atmosphere. Moreover, the process of soil air motion in the pore space of the covering rocks intensifies exhalation of soil radon, as in the case of micro-oscillations of the ground (see the beginning of Section 4.2).

Sections 2.2 and 2.3 clearly showed that fair-weather conditions [44–46], under which almost all the described research studying the relationships between geological heterogeneities and zones of geodynamic processes was carried out, should be supplemented by the monitoring of relative humidity. Changes in this characteristic inevitably introduce noise variations in the elements of surface atmospheric electricity of meteorological origin. The results of the current section highlight the need to pay close attention to the stability of atmospheric pressure, particularly if atmospheric-electrical monitoring is carried out in places where groundwater and perched water are close to the ground surface.

4.3. Geology, Geodynamics, and Thunderstorm Activity

For many decades, studies of atmospheric electricity have distinguished fair-weather electricity from thunderstorm electricity [47–52]. The planetary scale of the global electrical circuit [53] combines these two scientific directions. Thunderstorms arise and elsewhere fair-weather conditions are observed at another location on the Earth at the same time. Both these processes contribute to the phenomenon of the global electrical circuit. Let us consider some examples of experimental observations where, in areas with fair weather conditions, a transition to thunderstorm activity is possible. Within the established relationships between hydrogen, methane, and radon [14, 32], we can testify that due to local geological features, and geodynamic and meteorological processes in large areas, conditions are created for the occurrence of cloud-to-ground discharges under abnormal concentrations of these gases.

In the early twentieth century, Professor L. N. Bogoyavlensky associated the regional recurrence of cloud-to-earth lightning discharges with the radioactivity level. According to his statistics, obtained for the region near the town of Sestroretsk, a high radioactivity level (high air ionization level) leads to high perishability in this area from lightning discharges. He observed this phenomenon every year. Unfortunately, the current condition of these territories is unknown. However, near the town of Sestroretsk there is a unique lake called Lopukhinka formed by several springs, where the volumetric activity of radon reaches about 400 Bq/l. The town of Sestroretsk, the settlements of Beloostrov and Pesochny, and the “Sestroretskoye Boloto” State Nature Reserve cover a total area of 1,900 hectares. In the western part of the swamp adjacent to the Sestroretsky Razliv Lake, the volumetric activity of radon reaches 252 Bq/l.

Assessing the results of L. N. Bogoyavlensky’s work, we can say that the presence of granites, slates, and metal ores in the ground sharply changes local air ionization; the closer to the Earth’s surface they are, the higher the ionization. Territories with surface rock exposure are struck by lightning at a frequency three times more than in areas of their occurrence at a depth of 60–80 m. For example, the Kursk Magnetic Anomaly experiences up to 32 thunderstorms and the Tikhvin Magnetic Anomaly up to 25 thunderstorms annually.

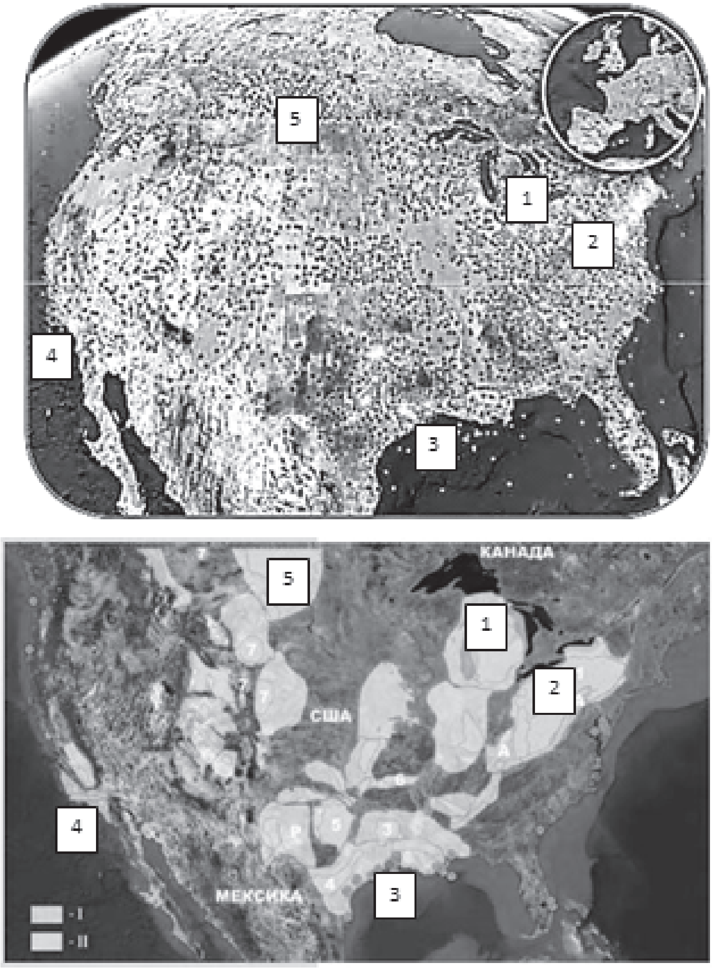

Figure 4.3.1: The location of thunderstorm activity foci in North America according to NLDN—the location of more than 150 sensors (upper); map of shale gas deposits and development in North America (lower).

The proposal by L. N. Bogoyavlensky regarding increased air ionization with increased thunderstorm activity in areas of shale is supported by data from the National Lightning Detection Network (NLDN, USA)—the most extensive network in North America. Figure 4.3.1 shows a map of thunderstorm foci recorded by this network. The spotty location pattern of these foci is apparent. This phenomenon allows us to say that local geological and geodynamic features affect the territorial distribution of lightning discharges.

We can compare the locations of thunderstorm foci to the map of shale gas deposits and development (see Figure 4.3.). Numbers 1 to 5 on these maps indicate territories with coincident areas of thunderstorm activity and shale gas development: 1 – Michigan (MI); 2 – New York (NY) and Pennsylvania (PA); 3 – Texas (TX), Louisiana (LA), and the Gulf Coast; 4 – California (CA), the southern coast of the Pacific Ocean; 5 – Montana (MT), North Dakota (ND), and the Canadian border.

Shale gas developments are accompanied by excessive discharge of methane—the main component of shale gas—into the surface atmosphere. Methane, in turn, transfers radon to the near-surface atmosphere.

To illustrate the increased air ionization above an ore body, we can use the observation results of AEF above the Novoselkovskoe ilmenite-magnetite ore deposit (Belarus) (Figure 3.2.2). In the ore body projection area, a dip in the atmospheric electric field is observed. The detected field drop-off is due to the electrochemical processes in the ore body cap accompanied by the release of hydrogen—the main gas-carrier of radon—into the near-surface atmosphere.

Statistically, lightning discharges most often hit clayey soil and wet areas; sloping river banks; and boggy territories, where groundwater approaches the ground surface. Swamps show the presence of biogenic methane, which is the second gas-carrier of radon; an argillaceous confining bed is also a stable source of the ionizer, with a maternal substance content half as much as in granites [54].

Figure 4.3.2 shows observation results on the polar conductivities of atmospheric air in the marshy area of the observation profile. The criterion of marshiness is the presence of reeds. The ratio of the average total polar conductivity in the marshy area of the profile (λ_{marsh} = 0.89 rel. units) to the mean value at pickets 14–19 and 24–34 (λ = 0.42 rel. units) is $\lambda_{\text{marsh}}/\lambda$ = 2.1. The meteorological situation determined the low values of the total polar conductivity ratio—measurements were carried out in the Stavropol Territory during a long-lasting period of abnormally hot weather of about 40 °C during the daytime.

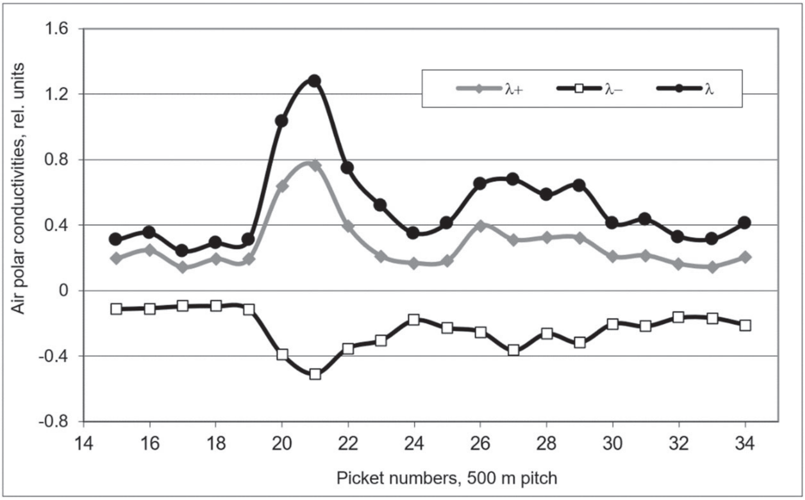

Figure 4.3.2: Variations of polar air conductivity in the profile of the North Stavropol GSF. At the interval between pickets 20 and 23, the profile crosses the marsh area.

Figure 4.3.3 illustrates the pronounced effect of ionization on the air conductivity as a result of the radionuclides released during the accident at the Chernobyl Nuclear Power Plant.

As far as is known, the Ostankino TV Tower built on boggy ground, is the highest lightning conductor in Russia. Over the years, experts from the Krzhizhanovsky Power Engineering Institute have taken photos of the tower from several neighboring structures simultaneously and concluded that flashes of lightning did not always hit the top of the Ostankino TV Tower—there were also discharges to the base of the sightseeing platform and the base of the tower. Statistically, 5 to 7 % of flashes of lightning hit the lateral surface of the tower far below its top.

Moreover, in the vicinity of the Ostankino TV Tower, downward flashes of lightning also hit the boggy area with the same frequency as before its construction. This allows us to assume that excessive emission of biogenic methane (boggy areas) and, as a consequence, radon, in the pre-thunderstorm period, due to a drop in atmospheric pressure, increases the conductive characteristics of the atmospheric surface layers.

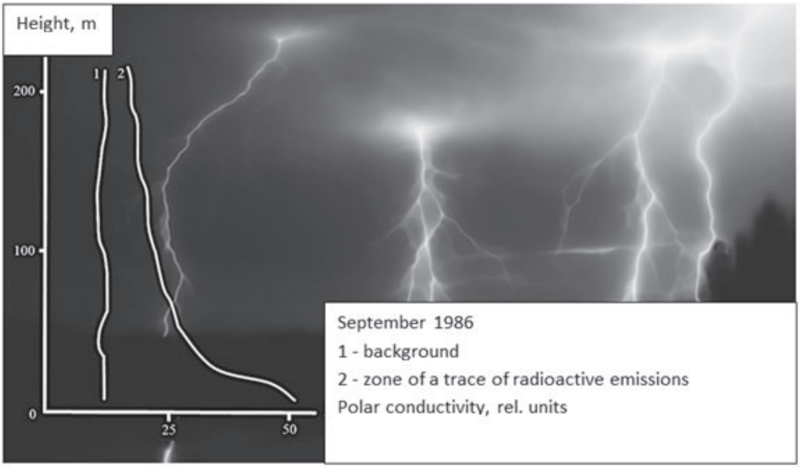

Figure 4.3.3: Electrical state of the atmospheric boundary layer affected by the release of radioactivity during the Chernobyl NPP accident.

Figures 4.2.8 and 4.2.9 provide a rough estimate of the increase in the air-earth current as a cumulonimbus cloud passes over the test site. We suppose that under normal conditions, the current can be estimated by an average world value of (2–3) × 10^{-12} A/m^2 [54]; with precipitation, including drizzle, the current can be estimated to be 10^{-9} to 10^{-8} A/m^2 [39, 55]. One of the records in Figure 4.2.6 was obtained at about 5 p.m. on May 21, 1987. The record shows that the electrical field at the test site (pickets 28, 29) was equal to about 100 V/m. At the AEF minimum, on May 21, 1987, at about 6 p.m., the field dropped to -5,050 V/m [14, 32]. As a thundercloud was passing, the air-earth current increased by three orders of magnitude, whereas the increase at the expense of the field was about 50 times. This means that polar conductivities increased by approximately 20 times.

Exhaled soil radon is the connection between water level dynamics and changes in the electrical characteristics of the surface air with atmospheric pressure variations [14, 32, 56]. Let us consider the experimental results for radon soil and volumetric atmosphere activity with a drop in atmospheric pressure during a pre-storm period. The research was carried out at the site of the Kasimov Underground Gas Storage Facility at the beginning of July 2003, with thunderstorms happening every 3–4 days at the time. While working on an observational profile lying along the western part of the gas storage facility, a cumulonimbus cloud appeared on the horizon. Table 4.3.1 shows the values of soil radon (Rn); atmospheric radon [Rn (a)]; and AEF recorded at pickets 6 to 8.

Table 4.3.1. The volumetric activity of soil radon, air radon, and AEF recorded at pickets # 6, 7, and 8

Observation picket #	Rn, Bq/l	Rn(*a*), Bq/l	AEF, V/m
6	2.74	1.19	296
7	4.73	3.66	394
8	15.36	8.99	-2,177
Radon volumetric activity increase	5.6 times	7.6 times	

The time of operation at one picket before moving on to the next was about 20 minutes, including: drilling of a sampling well; sampling; sample analysis for soil radon content; purging of the working volume using atmospheric air; and atmospheric sample analysis for atmospheric radon content. When measuring the volumetric activity of soil radon and atmospheric radon, a single instrument was used. Changes in the monitored parameters were rapid and, as such, the results obtained may not be wholly accurate.

The increase in volumetric radon activity during the pre-storm pressure drop was of great interest. Due to frequent thunderstorms in July 2003, the experiment was repeated using two identical radon sensors that had been checked beforehand. The measurements were carried out in a stationary position, on a cushion of bulk soil (sand) 0.6–0.8 m thick, in a marshy area at a distance of several hundreds of meters eastwards from the gas storage area. In a single sampling cycle, the soil air was pumped through the working volume of the hydrogen sensor to the working volume of the radon sensor. The measurements were carried out 43 minutes, 23 minutes, and 3 minutes before a thunderstorm began. The measurements are shown in Table 4.3.2; the last table row gives the relationship of the monitored parameters 3 minutes and 43 minutes before precipitation began.

The increases in the volumetric activity of soil and atmospheric radon 40 minutes before the event were comparable to each other. The increase in radon content was comparable to the estimate of the increase in the conductive characteristics of the atmosphere during the passage of a cumulonimbus cloud over the Uznozh Test Range. The measurements shown in Tables 1 and 2 suggest that in the area of the Klimovsk Underground Gas Storage Facility, during the injection period and in a pre-storm period, the content of atmospheric radon can increase by 8 to 15 times.

Table 4.3.2. Changes in the volumetric activity of radon in the soil, atmosphere, hydrogen, and AEF with an atmospheric pressure drop in the period before to a thunderstorm

Time before thunderstorm (pressure drop time)	Rn, Bq/l	Rn(*a*), Bq/l	$H_2, \times 10^{-4}$, vol.%	AEF, V/m
43 minutes	0.67	0.32	4.2	312
23 minutes	4.73	1.75	10.5	-1,180
3 Minutes	11.59	4.9	35.2	-7,500
Radon and hydrogen content increase within 40 minutes	**17.3 times**	**15.3 times**	**8.3 times**	

Let us consider the results of AEF observations in the profile in the central part of the Kasimov Gas Storage Facility, crossing the injected gas spreading line from the injection well cluster to the dome of the reservoir bed. The profile was observed twice: the first time was in autumn 2000, 10 days after the completion of the injection cycle; and the second time was in July 2003 at the third month of the injection cycle. The average AEF values in the profile varied broadly: $E(2000)_{ave}$ = 563 V/m; $E(2003)_{ave}$ = 210 V/m. Therefore, for the convenience of comparing the AEF variations, the graphs are presented in absolute and relative units (Figure 4.3.4).

The injection process was accompanied by the extension of rocks covering the reservoir and an increase in the pore space volume of the surface soil layers—during structural leveling at the Krasnopartizansky Gas Storage Facility in Ukraine, a rise in the ground surface of up to 2 cm was recorded. An increase in the pore space volume inevitably stimulates soil-atmosphere air exchange, with increased exhalation of soil radon and a decrease in AEF [57].

A section of the profile between pickets 6 and 14 fits along the gas escape line from the injection well cluster to the dome of the gas storage facility. The average field in the profile was $E(2003)_{ave}$ = 210 V/m; at the section following pickets 6–14, this was even less with a value $E(6\text{-}14)_{ave}$ = 190 V/m.

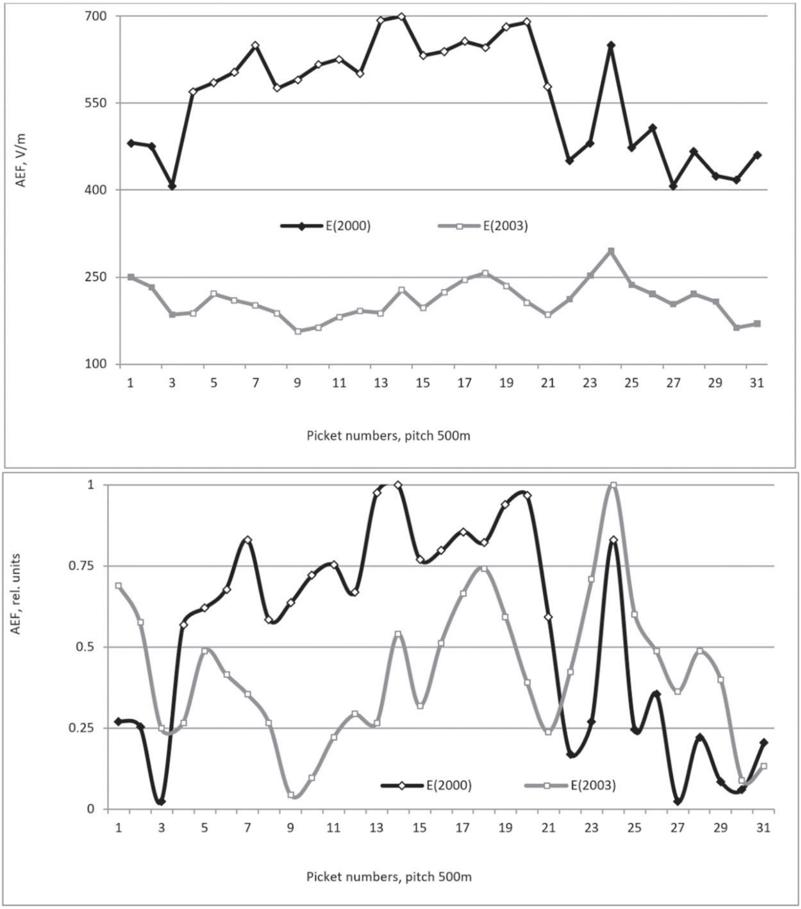

Figure 4.3.4: The results of AEF observations on the profile passing by the injection well cluster in 2000 and 2003. For clarity, the field measurement data are given in absolute and relative units.

Unlike the North Stavropol Gas Storage Facility, which was located on the site of the depleted North Stavropol deposit [58], the reservoir bed near Kasimov is artificial. Over the decades of its operation, due to a non-dense surface cover, the content of hydrogen and methane in the surface layers increased by almost two orders of magnitude. The average values of soil hydrogen and methane were equal to H_2(ave) = 0.0012 vol.%, CH_4(ave) = 0.0220 vol.% at the gas storage site; and on a profile 2 km from the injection zone—H_2(ave) = 0.00091 vol.%, CH_4(ave) = 0.016 vol.% (data obtained from laboratory analysis of samples).

For the two weeks of research at the gas storage facility, only one night-time thunderstorm occurred; the rest of the thunderstorms occurred in the afternoon—thermal thunderstorms. The employees of the gas storage facility, who lived 5 to 20 km from their place of work, told us that thunderstorms mainly occurred across the area of the gas storage facility. All this supports the assumption that excessive hydrogen and methane release into the atmosphere, which act as radon gas carriers, during the injection period and a pre-storm pressure drop may be the reason for increased thunderstorm activity in July 2003 over the Kasimov Gas Storage Facility site.

In the mid-twentieth century in France, the idea of constrained radioactive ionization of air causing the lighting conductor effect was proposed. Radioactive lightning conductors were developed, although they were only produced for a short while. The reason for their failure was the impossibility of safely using such a powerful ionizing radiation source. However, the ionizing effect, which can be achieved with a powerful source, can be achieved by using a less powerful, aerial source. This can be illustrated by the increase in thunderstorm activity in clayey, wet areas; flat river banks; boggy territories, where groundwater comes closest to the surface; and in places where radionuclides were present as a result of the Chernobyl accident. A pre-storm pressure drop naturally enhances the effect of ionization by at least an order of magnitude, forcing such an area to work as an aerial lightning conductor.

A drop in atmospheric pressure inevitably accompanies the formation of cumulonimbus cloud. Moreover, about 60 % of thunderstorms occurring throughout the year around the world are thermal thunderstorms, the time range of which falls on the daily minimum of atmospheric pressure and the daily maximum of soil radon exhalation.

4.4. References to Chapter 4

1. Ibinder, A.B. *Calculation of Main and Field Pipelines for Strength and Stability*. Moscow, Nedra, 1991, 40-79. [in Russian]
2. Borodavkin, P.P., and Beresin, V.L. *Construction of Main Gas Pipelines*, Moscow, Nedra, 1987, 104. [in Russian]
3. Borodavkin, P.P. *Soil Mechanics in the Pipeline Construction*, Moscow, Nedra, 1986, 133-161. [in Russian]
4. Nikitin, V.N. *Grounds for Engineering Seismic Survey*, Moscow, Izdatelstvo MGU, 1981, 175p. [in Russian]
5. Ogilvi, A.A. *Grounds for Engineering Geophysics*, Moscow, Nedra, 1990, 501p. [in Russian]
6. Sergeev, E.M. *Geological Engineering*, Moscow, MSU Publ., 1978, 384p. [in Russian]
7. Bondarenko, V.M., Viktorov, G.G., and Demin, N.V. *Novel Methods of Engineering Geophysics*, Moscow, Nedra, 1983, 223p. [in Russian]
8. Shuleikin, V.N., Reznichenko, A.P., and Nikulin, D.A. Gas permeability—the reference parameter of the landslide stressed state, *Proc. XII Geophys. V.V. Fedynsky Readings "Geophysics of the XXI Century: 2005."* Moscow, Nauchny mir, 2006, 341-346. [in Russian]
9. Shuleikin, V.N. Monitoring of the landslide slope stressed state at the pipeline route, *Oil&Gas Journal Russia*, 2012, **9**(64), 82-87. [in Russian]
10. Shuleikin, V.N. Complex atmospheric-electrical and hydrogen-radon study of the stress state of the geological environment, *Proceedings of VII Russian Conference for the Atmospheric Electricity*. Saint. Petersburg, 2012, 269-271. [in Russian]
11. Nikolaev, I.N., and Litvinov, A.V. Technique of measuring low H_2 and H_2S concentrations above the water surface, *Measurement Equipment*, 2004, **5**, 54-60. [in Russian]
12. Nikolaev, I.N., Litvinov, A.V., and Khalfin, T.M. Automated hydrogen gas detectors in the range of 10^{-6}-1.0% volumetric concentrations, *Measurement Equipment*, 2004, **7**. [in Russian]
13. Litvinov, A.V., Kalinina, L.N., and Nikolaev, I.N. Low-power hydrogen gas analyzer based on MIS-sensor, *Metrology*, 2012, **12**, 37-41.
14. Shuleikin, V.N., Shchukin, G.G., and Kupovykh G.V. *Development of Methods and Means for Applied Geophysics—*

Atmospheric-Electrical Monitoring of Geological Heterogeneities and Geodynamic Process Zones, SPb.: Publ. TsOP RGGMU, 2015, 205p. [in Russian]

15. Shuleikin, V.N. *Atmospheric-Electrical and Hydrogen-Radon Monitoring of a Landslide Stressed State. Part 1, Advanced Topics in Oil and Gas,* **1**(16), 25p. [in Russian]
16. Shuleikin, V.N. *Atmospheric-Electrical and Hydrogen-Radon Monitoring of a Landslide Stressed State. Part 2, Advanced Topics in Oil and Gas,* 2017, **1**(16), 16p. [in Russian]
17. Shuleikin, V.N. *The Earth and Atmospheric Electricity*, New York, Nova Science Publishers, 2018, 143p.
18. Kudrinskaya, T.V. Experimental studies of ionization processes in the near-surface atmospheric layer. *Candidate Thesis*, Nalchik, 2013, 20p. [in Russian]
19. Barberio, M.B., Gori, F., Maurizio Barbieri, M. *et al. Diurnal and Semidiurnal Cyclicity of Radon (222Rn) in Groundwater*, Giardino Spring, Central Apennines, Italy, *Water*. 2018, **10**, 11p.
20. Morozova, L.I. The manifestation of the Main Ural Fault in the cloudiness field on satellite images, *The Earth Study from Space*, 1980, **3**, 101-103. [in Russian]
21. Avenarius, I. G., Bush, V.A., and Treschov, A.A. The use of satellite images for the study of tectonic structure of the shelves, *Geology, and Geomorphology of Shelves and Continental Margins*, 1985, Moscow, Nauka, 163-172. [in Russian]
22. Florensky, P.V. *A Complex of Geological, Geophysical, and Remote Methods for the Study of Oil and Gas Regions*, 1987, Moscow, Nedra, 205 p. [in Russian]
23. Letnikov, F.A. *Synergism of the Human Environment. The Atlas of Temporal Variations of Natural, Anthropogenic, and Social Processes*, 2002, Moscow, Yanus-K, **3**, 69-78. [in Russian]
24. Boyarchuk, K.A., Karelin, A.V., Pulinets, S.A. *et al*. The unified concept of detecting signs of an impending strong earthquake within the framework of the complex system of the lithosphere-atmosphere-ionosphere-magnetosphere, *The Space Science and the Rocket Science*, 2012, **3**(68), 21-42. [in Russian]
25. Pulinets, S.A, Morozova, L.I., and Yudin, I.A. Synchronization of atmospheric indicators at the last stage of earthquake preparation cycle, *Research in Geophysics*, 2014, **4**, 45-50.
26. Morozova, L.I., and Dyad'kova, P.G. Dynamics of Cloud and Thermal Anomalies in the Region of the Tohoku Mega-

Earthquake (Japan), which happened on March 11, 2011, M = 9, *NTR*, 2011, **90**(4), 25-37.

27. Doda, L.N., Martynov, O.V., Pakhomov, L.A. *et al*. The ground-space monitoring and forecast of mega-earthquake in Japan on March 11, 2011, *NTR*, 2011, **90**(1), 35-44.
28. Tabulevich, V.N. *Complex Studies of Microseismic Vibrations*, Moscow, Nauka, 1986, 152p.
29. *Observation Results for Surface Atmospheric Electricity (the Global Network)*, Leningrad: A.I. Voeykov MGO, 1982-1992. [in Russian]
30. Shuleikin, V.N., and Polikarpov, A.M., Ocean noises and variations in surface atmospheric electricity, *Proc. All-Union Symp. "The Relationship of Regional and Global Processes in the Atmosphere and Hydrosphere*," 1988, Tbilisi, 77.
31. Shuleikin, V.N., and Polikarpov, A.M. On Correlation of microseismic, hydrogeological and atmospheric-electrical processes, *Proc. All-Union Sem. "Nontraditional Research Methods for Heterogeneity in the Crust*," M-Zvenigorod, 1989, 124-125. [in Russian]
32. Shuleikin, V.N. Atmospheric-electrical monitoring of the geodynamical process, *Proc. 9-th Int. Conf. on Atm. EI.*, St. Petersburg, 1992, 499-503. [in Russian]
33. Shuleikin, V.N., and Shchukin, G.G. Atmospheric electricity and microvibrations of the Earth, *Meteorology, and Hydrology*. 2015, **12**, 38-46.
34. Shuleikin, V.N. Earth noises and atmospheric electricity, *All-Russian Acoustic Conference*, 2014, 58-59. [in Russian]
35. Shuleikin, V.N., and Polikarpov, A.M. On Correlation of microseismic, hydrogeological, and atmospheric-electric processes, *Proc. All-Union Sem. "Alternative Methods for Studying Heterogeneities of the Earth's Crust*," M-Zvenigorod, 1989, 124-125. [in Russian]
36. Shuleikin, V.N., and Polikarpov, A.M. A model of atmospheric-electrical, microseismic and hydrogeological interactions, *Proc. IV All-Union Symp. on Atmospheric Electricity*, 1990, Nalchik, 38-39. [in Russian]
37. Shuleikin, V.N. On the correlation of the dynamics of elements of surface atmospheric electricity and aquifers, *Proc. IV All-Union Symp. on Atmospheric Electricity*, 1990, Nalchik, 30-32. [in Russian]

38. Shuleikin, V.N., and Nikulin, D.A. Electrical phenomena in the atmosphere—a natural indicator of geodynamic processes, *Proc. All-Russian Conf. "Risk-2003,"* **1**, 274-277. [in Russian]
39. Tverskoi, P.N. *The Course of Meteorology*, Leningrad, 1951, Gidrometizdat, 887p. [in Russian]
40. Frenkel, Ya.I. *The Theory of Atmospheric Electricity Phenomena*, Leningrad, GITTA, 1949, 155p. [in Russian]
41. Kuptsov, A.V., Marapulets, Yu.V., Mishchenko, M.A., Rulenko, O.P., Shevtsov, B.M., and Shcherbina, A.O. About the relation of high-frequency acoustic emission to the electric field in the surface atmosphere, *Volcanology and Seismology*, 2007, **5**, 71-76. [in Russian]
42. Bagmet, A.L., Bagmet, M.I., Barabanov, V.L. *et al*. The study of the Earth tidal oscillations of the groundwater level in the Obninsk well, *Izvestiya AN SSSR*, *Ser. Physics of the Earth*, 1989, **11**, 84-95. [in Russian]
43. Barabanov, B.L., Grinevsky, A.O., Kalachev, A.A., and Savin, I.V. The well-aquifer system frequency response according to observations for groundwater level, *Izvestiya AN SSSR. Ser. Physics of the Earth*, 1988, **3**, 41-50. [in Russian]
44. Imyanitov, I.M., and Shifrin, K.S. The current status of research of atmospheric electricity, *Uspekhi Fizicheskikh Nauk*, 1962, **4**, 593-642. [in Russian]
45. *The Guide for Surface Observations of Atmospheric Electricity Elements*, Leningrad, Izdatelstvo GGO im. A.I. Voeykova, 1960, 95p. [in Russian]
46. Semenov, K.A. Good weather and atmospheric electricity elements, *Proc. GGO im. A.I. Voeykova*, 1982, **455**, 112-119. [in Russian]
47. *Proc. III All-Russian Symposium on Atmospheric Electricity*, Tartu, 1986, 300p. [in Russian]
48. *Proc. 8-th Conference on Atmospheric Electricity*, Uppsala-Sweden, 1988, 897p.
49. *Proc. IV All-Russian Symposium on Atmospheric Electricity*, Nalchik, 1990, 312p. [in Russian]
50. *Proc. 9-th Conference on Atmospheric Electricity*, St. Petersburg-Russia, 1992, **1-3**, 977p. [in Russian]
51. *Proc. V Russian Symposium on Atmospheric Electricity*, Vladimir, 2003, 344p. [in Russian]
52. *Proc. VII All-Russian Conference on Atmospheric Electricity*, Saint. Petersburg, 2012, 287p. [in Russian]

53. *Proc. Conference "Global Electrical Circuit,"* Yaroslavl, 2013, 136p. [in Russian]
54. Koshkin, N.I., and Shirkevich, M.G. *Handbook on Elementary Physics*, 1976, Moscow, Nauka. [in Russian]
55. Kanonidi, K.Kh., Lidvansky, A.S., Sobisevich, L.E., and Khaerdinov, N.S. Geomagnetic field pulsations associated with cosmic rays' intensity during thunderstorms, *Proceedings of the 31-st All-Russian Conference on Cosmic Rays*, Moscow, MGU, 2010. [in Russian]
56. Shuleikin, V.N. Aquifer dynamics and atmospheric electricity, *Izvestiya, Atmospheric and Oceanic Physics*, 2018, 7, 29-42. [in Russian]
57. Shuleikin, V.N., and Zubarev, A.P. Methane distribution monitoring by gas storage reservoir bed from the Earth surface, *Gas Industry*, **12**(667), 2011, 48-51. [in Russian]
58. Alekseev, F.A., Voitov, G.I., Lebedev, V.S., and Nesmelova, Z.N. *Methane*, 1978, Moscow: Nedra, 310p. [in Russian]

CONCLUSION

The interest of researchers into electrical phenomena in the atmosphere arose in the mid-eighteenth century and was naturally associated with thunderstorm phenomena. G. Richman built the first electrical measuring device—the "electric pointer"—using which, together with M. Lomonosov, he proved the existence of electric charges in the atmosphere in the absence of thunderstorms. B. Franklin described and created the first lightning conductor, which "...either prevents lightning discharge from the cloud or, already at the discharge, deflects the lightning to the ground without any detriment to a building...."

Since the early twentieth century, interest in the study of lightning and thunderstorms has greatly decreased. The focus has primarily been on the study of the electric field in fair weather. In the 1920s, an expedition aboard the brigantine Carnegie, which was constructed from wood and other anti-magnetic materials, to the Pacific, Atlantic, and Indian oceans discovered the presence of unitary variation of the field. The mismatch of the diurnal variation of the atmospheric electric field recorded, under continental conditions with a unitary variation, led to the discovery of the radon mechanism for generating a surface air space charge. The ionization of surface air by the exhalation of soil radon served as the first indication of the geological and geodynamic nature of surface atmospheric electricity.

The high molecular weight of the ionizer, Rn^{222}, precluded the possibility of its spontaneous sub-vertical migration. Complex gas atmospheric-electrical observations helped model the relationships between the gas and electric fields of the Earth and the atmosphere. Hydrogen and methane bubbles capture soil radon at a depth of 4–6 m and lift it to the surface atmosphere. Radiogenic gas ionizes the air and forms light ions that determine its polar conductivity. The aggregation of light ions with neutral condensation nuclei (aerosols) causes the formation of heavy ions, which are primarily responsible for the existence of the atmospheric electric field (AEF). As such, soil radon acts as an intermediary and allows the determination of the density of sub-vertical carrier gas fluxes through the electrical characteristics of the surface air.

A negative earth charge inevitably leads to a redistribution of the space charge of the surface atmosphere. The initial solutions to the electrode effect problem were obtained for a case with the presence of light ions in the atmosphere. The solutions obtained made it immediately possible to distinguish two cases of a change in the atmospheric electric field with elevation: the classical electrode effect, which allowed a smooth decrease of the field with height until reaching the background level; and the reverse electrode effect, in which the field drops below the background level and then reaches it after bending back up. Today's position describes the non-stationary electrodynamic model of a horizontally homogeneous convective-turbulent surface layer of the atmosphere, taking into account multiple charged aerosol particles. It confirms the existence of the classical and reverse electrode effects and extends its manifestation zone to an elevation of tens of meters above the ground. The calculation results unambiguously explain the recorded bipolar anomalies of the atmospheric electric field before seismic events. At low ionization rates—a low level of exhalation of soil radon (the compression zone)—the classical electrode effect takes place. At high ionization rates—a high level of radon content in the surface atmosphere (the extension zone)—a layer of negative space charge is formed above the ground, leading to the reverse electrode effect. Turbulence "erodes" the space charge formed near the ground surface, thereby expanding the zone of the electrode effect to tens of meters.

The modeled approximation of the relationships between hydrogen, methane, radon, and elements of the surface atmospheric electricity, and the solution of the electrode effect problem, have made it possible to proceed to the analysis of the atmospheric-electrical monitoring results of geological heterogeneities and zones of geodynamic processes. For many years, measuring devices—a field mill atmospheric electric field sensor and an aspiration condenser for recording polar air conductivities—have been used in continuous observational measurement; a differential passive antenna was designed and built to measure the air-earth current; finally, recorders for radon activity and hydrogen concentrations have been produced in industrial settings.

Contrastive changes in the soil-atmosphere air exchange should, by definition, be expected in fracture zones, i.e., in areas where the Earth's crust is loosening. The results of fieldwork in a seismically active region (Dagestan) proved that the atmospheric electric field drops to negative values in the fault zone of the Aktash River. Observations in a seismically calm region (the Kaluga Ring Structure; the Aleksandrovsky Fault in Belarus) have led to the recording of similar field variations, but with smaller differences in amplitude; the field drop is confidently observed above the zone of a sharp lowering of the basement roof, with an increase in the thickness of sedimentary rocks. Polar air conductivities grow above underground utilities (Moscow subway lines) and karst formations (Tula). In some cases, when yielding beyond the margins of the projection of an investigated heterogeneity at the ground surface, side extremes are recorded, the presence of which makes it possible to estimate the depth of soil loosening in the investigated area. A similar effect can be observed in the variations of the atmospheric electric field along an observation profile that extends beyond the reservoir bed of the North Stavropol Gas Storage Facility, in the depleted North Stavropol field. The field changed by the Cos*X*/*X* law, and the distance between maximums was comparable to the depth of the cap zone.

The initial results of multi-profile changes in the atmospheric electric field were obtained in Belarus, at the Novoselkovsky ilmenite-magnetite ore deposit. The average drop of the field above the ore body amounted to 100 V/m. Such a drop in the atmospheric electric field is due to electrochemical processes in the ore body cap accompanied by the release of hydrogen—the gas-carrier of radon—to the surface atmosphere.

Methane, the second gas-carrier of the ionizer, is a component of oil field plumes, and is present in elevated concentrations in the surface soil layers of underground gas storage facilities in artificial reservoirs. In the case of observations of the atmospheric electric field at the Third Rechitsa Oilfield (Belarus), a field drop relative to background values beyond the deposit by 150 V/m was recorded at the minimum. After three years of repeated profile measurements, the field drop decreased to 60 V/m due to a decrease of *in-situ* pressure and reservoir flooding. The same field drop was recorded at the Aleksandrovskoe Oilfield; parallel control of the soil radon showed the presence of a two-fold increase in its volumetric activity over the deposit.

Two years of research at the oldest underground gas storage facility in Schelkovo over the last days of combustible gas injection allowed mapping of the reservoir bed contour from the ground surface. The average decrease in the atmospheric electric field above the injection volume in 1999 was 270 V/m; in 2000, the average field drop decreased to 190 V/m. The work continued into the year 2000 with three observation profiles at the Kasimov Gas Storage Facility, which gave results in the average field values above the injection volume of 138 V/m, 136 V/m, and 140 V/m; beyond the projection of the injection volume zone and onto the Earth's surface, the field increased to 184–240 V/m.

Geodetic work at sites of underground gas storage facilities have shown that combustible gas injection into a reservoir bed causes deformation to the level of 10^{-5}. Hence, the pore space, which is packed with volatile gases of soil air, expands. The release of volatile gases to the surface atmosphere occurs not only during the injection period, but also after its completion when the combustible gas spreads from the injection well cluster to the dome of the gas storage facility. In an area of 19 injection wells at the Kasimov Gas Storage Facility, on the fifth day after the completion of the weekly injection cycle, a rapid survey of the atmospheric electric field was carried out over two hours, with eight pickets around each well. The measurements were carried out in ideal weather conditions—a windless autumn day, and 0-point cloudiness. The average field values of two wells, through which the gas was injected to the dome of the gas storage facility, turned out to be equal to E_2 = 304 V/m; the average value for the remaining 17 wells was E_{17} = (451 +/- 11) V/m. The results suggested that at the time of measurement, the combustible gas remained beneath the line of these two wells.

In the proposed model, except for methane, all the listed gas and electrical parameters are amenable to rapid observation, which opens up the possibility of indirect assessment. The sensitivity of modern sensors (PGA-4) for express monitoring of methane concentration is no lower than 10^{-1} vol.%. Let us consider an estimate of the methane content calculation error based on measurements of hydrogen, radon, polar conductivities, and the atmospheric electric field. Working formulas were introduced as functions of pairs of values (soil radon—atmospheric radon), (soil radon—AEF), and (soil radon—polar air conductivity). We now turn our attention to the working formula for the first pair of values, since the single reading error of the radon sensor was maximal. In particular, in an area with an average methane concentration of (10^{-6}–10^{-5}) vol.%, the relative error of the methane concentration calculation was $\Delta CH_4/CH_{4ave}$ = 28 %. As the soil methane concentration increased to (10^{-3}–10^{-2}) vol.%, the relative error of its calculation was reduced by a factor of two.

Microseismic vibrations stimulate soil-atmosphere air exchange. Man-made microseisms in the range of 5.0–25.0 Hz and an amplitude of 100 μm, caused by the passage of a subway train, increased the polar conductivities 2.0 to 2.5 times. Even with slight freezing of the soil, the same man-made microseisms caused by the continuous coupling of train cars on shunting routes led to a drop in the atmospheric electric field of 200–250 V/m at the railway, compared to the background signal level at a distance of a few hundred meters from the source.

The effect of microseismic regulation of soil radon exhalation can be observed with a minimal level of vibration (vibration velocities of v ~10^{-8}–10^{-7} m/s), but with long duration. Significant correlation coefficients were obtained for the core variations of the atmospheric electric field and the microseismic velocities generated by the booster compressor stations at the site of the Kasimov Gas Storage Facility. The compressor stations have operated for decades for 3 to 4 months a year.

The artesian water intake that fulfils the needs of a city with a population of 200,000 people sees a daily variation in atmospheric electric field peak values at the traverse of the water intake station of about 400–900 V/m. The reason for this is that there is a depression funnel minimizing soil radon exhalation. The reverse process—the injection of 30 m^3 of fluid to a depth of 50 m through hydraulic fracturing—leads to a sharp drop in the atmospheric electric field to -150 V/m some 20 minutes after the onset of injection. The shockwave of hydraulic fracturing inevitably leads to a powerful pulse ejection of the ionizer into the installation volume of the measuring device. The formation of an interlayer of negative space charge leads to a reversible electrode effect somewhere in the middle of the lifetime of heavy ions.

The combined effect of hydrogeological and microseismic processes on the atmospheric electric field was considered in analyzing the results of observations of the amplitudes of global oceanic microseisms, A, with periods of 4 to 9 seconds in the North Atlantic (Pulkovo seismic station); variations in the aquifers levels of observation wells at medium depths $z1$ ~6m, $z2$ ~30m, and $z3$ ~60m (North-West Department of Geology of Leningrad City); and the atmospheric electric field, E, (the Voeykovo Observatory, Leningrad Region) for 1984.

The correlation coefficient between the measured mean monthly values of the atmospheric electric field for 1984 and the calculated values of the parameter as a function of the mean monthly water levels and amplitudes of global microseisms is quite high k[E; $E(z1, z2, z3, A)$] = 0.79. The primary factor in the annual variation of the field is caused by changes in water levels in the observation wells $k[E; E(z1)] = 0.72$, $k[E; E(z1, z2)] = 0.78$. However, if we consider the relationship of the atmospheric electric field with the level of global oceanic microseisms during periods of microseismic storms, when the vibration amplitudes increase to A ~4–6 µm, the correlation coefficients of the measured and calculated field variations also increase: $k[E; E(A)]_{3\text{-}10.02} = 0.84$; $k[E; E(A)]_{27.02\text{-}4.03} = 0.70$.

Let us consider one more example of the relationship between hydrogeological and atmospheric-electrical processes. Simultaneous measurement of the air-earth current, $j(t)$, the atmospheric electric field, $E(t)$, and the water level in the observation well, z, which opens the aquiclude, when a thunderstorm cloud (with no rain) passed by and with drizzle, indicated an apparent relationship between the studied parameters. With the passage of a cumulonimbus cloud, the increase in the water level amounted to ~3 mm; during drizzle, the level varied between 0 mm and 3 mm. The correlation coefficient between the measured and calculated values of the air-earth current, $j(z)$, is exceptionally high—$k[j(t), j(z)] = 0.92$. The same was observed in variations of the atmospheric electric field and water level in the observation well, but for separate calculated data sets, $E(z)$, for a thunder cloud and with drizzle: $k = [E(t), E(z)]_{\text{thunderstorm}} = 0.98$; $k = [E(t), E(z)]_{\text{drizzle}} = 0.91$.

A drop in atmospheric pressure accompanies cumulonimbus cloud formation; when drizzling, fluctuations in atmospheric pressure occur. Under constant pressure, the weight of the air column keeps aquifers at a certain level. A drop in atmospheric pressure leads to a rise in their levels. The sensitivity of groundwater and perched water levels see a drop in atmospheric pressure (barometric efficiency) of about 8 mm/hPa; in aquicludes isolated from the atmosphere, it is significantly less than 2 mm/hPa.

In the examples considered, the dynamics of soil-atmosphere air exchange are associated with the dynamics of the groundwater level. In spring, standing water at the installation site of the measuring devices and the water boundary in the nearby pond were at a level of about 0.8 m. When the aquifer level rises from the pore space of the surface soil layers, the soil air, which consists of hydrogen, methane, and radon, is squeezed into the atmosphere.

Moreover, the process of soil air motion in the pore space of the covering rocks intensifies exhalation of soil radon, as in the case of micro-oscillations of the ground. A particular experiment under the conditions of a close approach of groundwater to the ground surface showed that the drop in atmospheric pressure during a pre-storm period (43 minutes before precipitation) led to an increase in atmospheric radon volumetric activity by a factor of 15.

A complex of hydrogen-radon and atmospheric-electrical measurements was successfully used in measuring the stress-state dynamics of a landslide, the instability of which was provoked by the laying of a gas pipeline. As a control characteristic, the relative gas permeability $G(H_2)$ was obtained from observations of the soil air hydrogen in the system of observation pickets by normalizing the data to the maximum value of the parameter H_{2max}. Taking into account the model's approximation, the relative gas permeability was calculated from the results of measurements of pairs of parameters [ground radon, Rn, and atmospheric radon, Rn(a)] $G[\mathrm{Rn}(a)]$; (ground radon and polar conductivity) $G(\lambda)$; (ground radon and inverse atmospheric electric field) $G[(1/E)]$. After averaging, the differences in relative gas permeability values in the second and the first observation cycles ΔG_{21} and then in the third and first observation cycles G_{31} etc. were estimated. Nine observation cycles showed that the load on the pipeline for the five years of observation remained almost unchanged—the sum of differential relative permeability values at the pipeline varied around zero and a cluster of technological wells restraining the movement of the landslide showed the stable state of compression recording.

All the described atmospheric-electrical observations were carried out under fair weather conditions—the wind speed was, at most, 6 m/s, and there was an absence of thunderstorms, precipitation, frost, fog, dust, and low cloud. All these meteorological characteristics were visually determined. To avoid noise from meteorological conditions effecting the results of atmospheric-electrical monitoring of geological heterogeneities and zones of geodynamic processes in the measurement process, it is necessary to instrumentally control the relative humidity of the air tracking the evaporation processes and atmospheric pressure, which can change the dynamics of soil radon exhalation.

Elements of surface atmospheric electricity have never been used in solving applied geophysical problems. The modeled approximation was repeatedly confirmed experimentally and the above review of field observations prove that atmospheric electrical monitoring can be successfully used for prospecting and exploratory geophysical work.

In training courses on atmospheric electricity, only meteorological effects on changes in the electrical characteristics of the surface air layer are considered. The established connections of the gas and electric fields of the Earth and the atmosphere indicate the terrestrial origin of the volume charge of the surface atmosphere; in stable meteorological conditions, the atmospheric electric field and the polar conductivities of air are determined solely by local geological and geodynamic features of the geophysical environment.